

STATIC AEROELASTIC MODELING AND PARAMETRIC STUDY OF  
STACKING SEQUENCE FOR LAMINATED COMPOSITE MISSILE FINS

A THESIS SUBMITTED TO  
THE GRADUATE SCHOOL OF NATURAL AND APPLIED SCIENCES  
OF  
MIDDLE EAST TECHNICAL UNIVERSITY

BY

GÖKTUĞ MURAT ASLAN

IN PARTIAL FULFILLMENT OF THE REQUIREMENTS  
FOR  
THE DEGREE OF MASTER OF SCIENCE  
IN  
AEROSPACE ENGINEERING

JUNE 2018



Approval of the thesis

**STATIC AEROELASTIC MODELING AND PARAMETRIC STUDY OF  
STACKING SEQUENCE FOR LAMINATED COMPOSITE MISSILE FINS**

submitted by **GÖKTUĞ MURAT ASLAN** in partial fulfillment of the requirements  
for the degree of **Master of Science in Aerospace Engineering Department,**  
**Middle East Technical University** by,

Prof. Dr. Halil Kalıpçılar \_\_\_\_\_  
Dean, Graduate School of **Natural and Applied Sciences**

Prof. Dr. Ozan Tekinalp \_\_\_\_\_  
Head of Department, **Aerospace Engineering**

Assoc. Prof. Dr. Dilek Funda Kurtuluş \_\_\_\_\_  
Supervisor, **Aerospace Engineering Dept., METU**

**Examining Committee Members:**

Assoc. Prof. Dr. Demirkan Çöker \_\_\_\_\_  
Aerospace Engineering Dept., METU

Assoc. Prof. Dr. Dilek Funda Kurtuluş \_\_\_\_\_  
Aerospace Engineering Dept., METU

Assoc. Prof. Dr. Ercan Gürses \_\_\_\_\_  
Aerospace Engineering Dept., METU

Asst. Prof. Dr. Mustafa Perçin \_\_\_\_\_  
Aerospace Engineering Dept., METU

Asst. Prof. Dr. Mustafa Kaya \_\_\_\_\_  
Aeronautical Engineering Dept., AYBU

**Date:** 19/06/2018

**I hereby declare that all the information in this document has been obtained and presented in accordance with academic rules and ethical conduct. I also declare that, as required by these rules and conduct, I have fully cited and referenced all material and results that are not original to this work.**

Name, Last name : Göktuğ Murat ASLAN

Signature :

## **ABSTRACT**

### **STATIC AEROELASTIC MODELING AND PARAMETRIC STUDY OF STACKING SEQUENCE FOR LAMINATED COMPOSITE MISSILE FINS**

Aslan, Göktuğ Murat

M.Sc., Department of Aerospace Engineering

Supervisor: Assoc. Prof. Dr. Dilek Funda Kurtuluş

June 2018, 116 Pages

In this thesis, a surface-to-surface missile model with laminated composite fins is examined with respect to one-way static aeroelastic response under constant supersonic flight conditions. Two different modified double wedge fins or control surfaces using for control actuation system of a missile are investigated and compared in terms of aerodynamic and linear structural characteristics in order to minimize tip deflection. A serial set of steady-state supersonic Computational Fluid Dynamics (CFD) analyses at different angles of attack are conducted in order to obtain pressure distribution causing the structural deflection or failure on fins having modified double-wedge cross-sections. Grid refinement study is also performed for CFD analysis part. Control surface models are manufactured and tested in supersonic wind tunnel at a certain angle of attack and Mach number in order to observe shock waves on control surfaces during the flight.

By using aerodynamic loads due to pressure distribution on fins, linear structural analyses with an algorithm written in Matlab® are executed in Nastran®. This algorithm examines the different stacking sequence of the laminated composite control surfaces in order to reduce tip deflection by considering four different failure criteria. Three structures with different stacking sequences not failing under maximum aerodynamic loads in structural analyses are manufactured and tested for both control surface models in order to compare and verify the maximum tip deflection results of Finite Element Method.

Keywords: Computational Fluid Dynamics, Stacking Sequence, Tip Deflection, Laminated Composite Fin, Failure Criteria, Finite Element Method,

## ÖZ

### **KATMANLI KOMPOZİT YAPIDAKİ FÜZE KANATLARININ STATİK AEROELASTİK MODELLEMESİ VE PARAMETRİK SERİM AÇISI ÇALIŞMASI**

Aslan, Göktuğ Murat

Yüksek Lisans, Havacılık ve Uzay Mühendisliği Bölümü

Tez Yöneticisi : Doç. Dr. Dilek Funda Kurtuluş

Haziran 2018, 116 Sayfa

Bu tezde, katmanlı kompozit yapıdaki kontrol yüzeylerine sahip bir karadan-karaya füze modelinin, sabit süpersonik uçuş koşulundaki tek yönlü statik aeroelastik tepkisi incelenmiştir. Uç kısmındaki sehim miktarını en aza indirmek için, değiştirilmiş çift kama kesit alanına sahip iki farklı kontrol yüzeyi, aerodinamik ve lineer yapısal karakteristikleri bakımından incelenmiş ve karşılaştırılmıştır. Farklı hücum açılarında, kontrol yüzeylerine etki eden, yapısal sehime ya da kırılmaya sebep olan basınç dağılımını elde edebilmek için bir dizi durağan durumdaki hesaplamalı akışkanlar dinamiği analizi (HAD) gerçekleştirilmiştir. Ayrıca HAD analizleri için çözüm ağı iyileştirme çalışması yapılmıştır. Şok açılarını gözlemlemek için, kontrol yüzeyi modellerinin üretimi gerçekleştirilmiş olup, bu modellerin belli bir hücum açısında ve Mach sayısında süpersonik rüzgar tüneli testleri gerçekleştirilmiştir.

Kontrol yüzeylerine etki eden basınç dağılımından kaynaklanan aerodinamik yükler kullanılarak, Matlab® programında yazılmış olan algoritma aracılığıyla, Nastran® programında lineer yapısal analizler gerçekleştirilmiştir. Katmanlı kompozit yapıya sahip kontrol yüzeylerinin farklı katman oryantasyonları, dört farklı hata kriterini göz önüne alarak, sehim miktarını azaltmak için bu algoritma tarafından incelenmiştir. Hasara uğramamış katman dizilimine sahip 3 farklı model, her iki kontrol yüzeyi için de üretilmiş olup, sonlu elemanlar metodu ile elde edilen en yüksek uç sehimini doğrulamak ve kıyaslamak için test edilmiştir.

Anahtar Kelimeler: Hesaplamalı Akışkanlar Dinamiği, Serim Açısı, Uç Sehimi, Katmanlı Kompozit Kanat, Hasar Kriteri, Sonlu Elemanlar Metodu.

*To My Wife*

## ACKNOWLEDGEMENTS

I am very thankful to my advisor Assoc. Prof. Dr. Dilek Funda Kurtuluş for her guidance and encouragements throughout the research.

I would like to thank to my mother, my father and my sister for their unflagging support throughout my life.

I would like to express my deepest gratitude to my wife for her support and patience throughout the research.

I wish also thank to my managers, Dr. Murat Şahin and Dr. Burcu Dönmez, for their guidance and support during the study.

This work is supported by SAYP project (2016-03-13-32-00-05) of METU in collaboration with Roketsan Missile Inc. and Undersecretariat for Defence Industries.

## TABLE OF CONTENTS

ABSTRACT .....	v
ÖZ .....	vii
ACKNOWLEDGEMENTS .....	x
TABLE OF CONTENTS .....	xi
LIST OF FIGURES .....	xiii
LIST OF TABLES .....	xvi
ABBREVIATIONS .....	xvii
CHAPTERS	
1. INTRODUCTION .....	1
1.1 Definition of Missiles .....	1
1.2 Aeroelasticity.....	4
1.3 Composite Materials.....	6
1.4 Aim of Thesis .....	8
2. LITERATURE SURVEY.....	9
3. FAILURE THEORIES .....	17
3.1 Maximum Stress Failure Criterion .....	19
3.2 Tsai- Hill Failure Criterion.....	19
3.3 Tsai-Wu Failure Criterion .....	20
3.4 Hoffman Failure Criterion.....	21
4. CFD MODELING AND WIND TUNNEL TESTING .....	23
4.1 Methodology and Geometry Description .....	23
4.1.1 Model 1 .....	25
4.1.2 Model 2 .....	25
4.1.3 CFD Grid Generation.....	26

4.2	Grid Quality Analysis .....	27
4.3	Boundary Layer Model.....	29
4.4	Solution Method and Boundary Conditions .....	33
4.5	Results .....	35
4.6	Wind Tunnel Testing .....	59
5.	STRUCTURAL ANALYSIS AND TESTS .....	67
5.1	Description of Material.....	68
5.2	Initial structural Analysis.....	72
5.3	Boundary Conditions of Initial Analysis .....	74
5.4	Results of Initial Analysis.....	76
5.5	Mesh Sensitivity Analysis .....	78
5.6	Parametric Study of Stacking Sequence .....	79
5.6.1	Parametric Study Routine.....	79
5.6.2	Code Verification Study.....	80
5.7	Results of Stacking Sequence.....	90
5.8	Loading Test.....	96
6.	CONCLUSION AND FUTURE WORKS .....	103
	REFERENCES.....	107
	APPENDICES	
A.	Nastran File Modification.....	111

## LIST OF FIGURES

### FIGURES

Figure 1 Guided Missile Control Types [2] .....	2
Figure 2 Javelin Medium Anti-Armor Weapon System [3].....	3
Figure 3 Forces and moment coefficients in six D.O.F. systems [4] .....	4
Figure 4 Collar's Aeroelasticity Triangle [5].....	4
Figure 5 Fields of Aeroelasticity .....	5
Figure 6 Laminated composite structure [8] .....	7
Figure 7 Turbulence Models comparative study [25] .....	14
Figure 8 Failure envelopes for UD carbon/epoxy (AS4/3501-6) lamina [27].....	18
Figure 9 Parts of missile Model .....	24
Figure 10 Missile and fixed wing dimensions (mm) .....	24
Figure 11 Control surface dimensions of missile model-1 .....	25
Figure 12 Control surface dimensions of missile model-1 .....	25
Figure 13 Fine grid details .....	27
Figure 14 Skewness ratio of Model-1 .....	28
Figure 15 Skewness ratio of Model-2 .....	29
Figure 16 $y^+$ values of turbulent layers [35].....	30
Figure 17 $y^+$ values of missile model-1.....	32
Figure 18 $y^+$ values of missile model-2.....	32
Figure 19 Dimensions of solution domain in m.....	34
Figure 20 Solution domain of CFD.....	34
Figure 21 Missile part notations.....	36
Figure 22 $C_L$ vs. $\alpha$ ( $^\circ$ ) graph of nose .....	37
Figure 23 $C_L$ vs. $\alpha$ ( $^\circ$ ) graph of body.....	38
Figure 24 $C_L$ vs. $\alpha$ ( $^\circ$ ) graph of fixed wing-4 .....	39
Figure 25 $C_L$ vs. $\alpha$ ( $^\circ$ ) graph of control surface-4 .....	40
Figure 26 $C_D$ vs. $\alpha$ ( $^\circ$ ) graph of nose .....	40

Figure 27 $C_D$ vs. $\alpha$ ( $^\circ$ ) graph of body .....	41
Figure 28 $C_D$ vs. $\alpha$ ( $^\circ$ ) graph of fixed wing-4 .....	42
Figure 29 $C_D$ vs. $\alpha$ ( $^\circ$ ) graph of control surface-4 .....	43
Figure 30 Normal Force (N) vs. $\alpha$ ( $^\circ$ ) graph of nose .....	44
Figure 31 Normal Force (N) vs. $\alpha$ ( $^\circ$ ) graph of body .....	45
Figure 32 Normal Force (N) vs. $\alpha$ ( $^\circ$ ) graph of fixed wing-4.....	45
Figure 33 Normal Force (N) vs. $\alpha$ ( $^\circ$ ) graph of control surface 4 .....	46
Figure 34 Axial Force (N) vs. $\alpha$ ( $^\circ$ ) graph of nose .....	47
Figure 35 Axial Force (N) vs. $\alpha$ ( $^\circ$ ) graph of body.....	47
Figure 36 Axial Force (N) vs. $\alpha$ ( $^\circ$ ) graph of fixed wing-4 .....	48
Figure 37 Axial Force (N) vs. $\alpha$ ( $^\circ$ ) graph of control surface 4.....	49
Figure 38 Spanwise variation of C.P. location via $\alpha$ ( $^\circ$ ).....	50
Figure 39 Variation of C.P. location through the chord length via $\alpha$ ( $^\circ$ ).....	51
Figure 40 Static pressure (MPa) distribution of model-1 at different $\alpha$ ( $^\circ$ ).....	52
Figure 41 Static pressure (MPa) distribution of model-2 at different $\alpha$ ( $^\circ$ ).....	52
Figure 42 Mach number distribution of model-1 at different $\alpha$ ( $^\circ$ ).....	53
Figure 43 Mach number distribution of model-2 at different $\alpha$ ( $^\circ$ ).....	54
Figure 44 Static pressure (MPa) distribution of control surface-4 of model-1 at different $\alpha$ ( $^\circ$ ).....	55
Figure 45 Static pressure (MPa) distribution of control surface-4 of model-2 at different $\alpha$ ( $^\circ$ ).....	56
Figure 46 Mach number distribution of control surface-4 of model-1 at different $\alpha$ .	57
Figure 47 Mach number distribution of control surface-4 of model-2 at different $\alpha$ .	58
Figure 48 Test specimens and their chord lengths [mm] .....	60
Figure 49 Supersonic wind tunnel.....	60
Figure 50 Shock waves at $M=1.6$ and $\alpha=0^\circ$ .....	61
Figure 51 Oblique Shock wave over a wedge [36] .....	61
Figure 52 Shock Wave versus Deflection angle of wedge with control surface 2D theoretical results [36].....	63
Figure 53 Shock wave comparison of CFD and test data at $M=1.6$ and $\alpha=0^\circ$ .....	64
Figure 54 Carbon/Epoxy CE 1007/310/37 Prepreg .....	71

Figure 55 Shell mesh model of structural analyses.....	73
Figure 56 Shell element thicknesses .....	73
Figure 57 Shell element thicknesses (given in meter) .....	74
Figure 58 Boundary conditions of control surfaces .....	75
Figure 59 Pressure distributions in Pa at $\alpha=15^\circ$ .....	76
Figure 60 Total Deformation in mm .....	77
Figure 61 Von Mises stress distribution in Pa .....	77
Figure 62 Maximum tip deflections of different mesh sizes in mm .....	78
Figure 63 Algorithm flowchart of parametric study for stacking sequence.....	80
Figure 64 Laminate with $[0^\circ/90^\circ/0^\circ]$ ply orientation.....	81
Figure 65 n-ply laminate and in-plane forces and moments [46] .....	83
Figure 66 Plate model under bending moment .....	85
Figure 67 2D plate model and its boundary conditions .....	86
Figure 68 Representation of ply orientation.....	91
Figure 69 Amount of ply orientations passed from failure tests for control surface of model-1 .....	92
Figure 70 Amount of ply orientations passed from failure tests for control surface of model-2 .....	93
Figure 71 Mould of control surfaces.....	97
Figure 72 Initial products without trimming.....	98
Figure 73 Final product of control surfaces .....	98
Figure 74 Length of a control surface sample.....	99
Figure 75 Loading test setup .....	99
Figure 76 Sample of Nastran® input file [44] .....	112
Figure 77 Bulk data section of Nastran® input file .....	113
Figure 78 Parts of the output file of initial analysis .....	114
Figure 79 General format of grid entry [44] .....	115
Figure 80 Grid data in free field [44] .....	116
Figure 81 Small field data entry [44] .....	116
Figure 82 Large field data entry format [44] .....	116

## LIST OF TABLES

### TABLES

Table 1 Classification of missiles in terms of launch mode.....	1
Table 2 Fiber and wire properties [7].....	7
Table 3 Least deformable 5 orientations of optimization study [25] .....	15
Table 4 Mesh Refinement Study.....	26
Table 5 Wedge and tetrahedral elements in missile models .....	26
Table 6 Skewness ratio with respect to element quality [34].....	28
Table 7 Operating Conditions [36].....	30
Table 8 Maximum first boundary layer thickness of missile parts .....	31
Table 9 CFD results Comparison between control surface models at $\alpha=15^\circ$ .....	59
Table 10 Shock wave comparison Table.....	64
Table 11 Elastic constants of Different Materials [42] .....	71
Table 12 Mechanical Properties of CE 1007/310/37 [43].....	72
Table 13 Results of Initial Analysis .....	78
Table 14 Results of code for a single step.....	86
Table 15 Comparison of analytical solution and code results.....	89
Table 16 A part of printed results of parametric study algorithm .....	90
Table 17 In-plane stresses and maximum tip deflection of least deflected ply orientations.....	91
Table 18 Least deformable 20 stacking sequence of control surface of model-1 .....	94
Table 19 Least deformable 20 stacking sequence of control surface of model-2 .....	95
Table 20 Total deformation with FEM of selected configuration.....	97
Table 21 Test inputs of control surface models .....	100
Table 22 Comparison of FEM and test results.....	101
Table 23 Comparison of control surface models .....	102
Table 24 Real number data entry types .....	115
Table 25 Field Format Types .....	115

## ABBREVIATIONS

$C_f$	: Friction coefficient
$E_1$	: Elastic modulus in fiber direction [Pa]
$E_2$	: Elastic modulus in matrix direction [Pa]
FI	: Failure Index
$G_{12}$	: Shear Modulus [Pa]
Re	: Reynolds Number
S	: Shear Strength [Pa]
$U_\tau$	: Frictional velocity [m/s]
$X_t$	: Tensile strength in fiber direction [Pa]
$X_c$	: Compressive strength in matrix direction [Pa]
$y^+$	: Non-dimensional distance to wall
$Y_t$	: Tensile strength in matrix direction [Pa]
$Y_c$	: Compressive strength in matrix direction [Pa]
$\alpha$	: Angle of attack [ $^\circ$ ]
$\beta$	: Shock wave angle [ $^\circ$ ]
$\theta$	: Wedge angle [ $^\circ$ ]
$\rho$	: Density [ $\text{kg/m}^3$ ]
$\mu$	: Dynamic viscosity [ $\text{N}\cdot\text{s/m}^2$ ]
$\sigma_1$	: In-plane stress in fiber direction [Pa]
$\sigma_2$	: In-plane stress in matrix direction [Pa]
$\sigma_{12}$	: In-plane shear stress [Pa]
$\tau_\omega$	: Wall shear stress [Pa]
$\vartheta$	: Poisson's ratio



# CHAPTER 1

## INTRODUCTION

### 1.1 Definition of Missiles

Missiles are self-propelled guided systems including detectors such as image, heat and inertial detectors in order to reach a target. They have high acceleration, range of speed and maneuverability in comparison to conventional air vehicles. Also, higher loading due to dynamic pressure occurs on missiles. Due to these differences, some aerodynamic design constraints may come to existence. For example, excessive aerodynamic heating, high pressure exerted on missile components and extreme gravitational force due to high acceleration may result in some structural problems.

Missiles are categorized in terms of warhead, propulsion systems, launch mode, range, and guidance system. On the other hand, launch mode is mostly used classification way. Missile types with respect to launch mode are shown in Table 1 [1].

Table 1 Classification of missiles in terms of launch mode

SAM	Surface-to-air missile
SSM	Surface-to-surface missile
AAM	Air-to-air missile
ASM	Air-to-surface missile
AUM	Air-to-underwater missile
UUM	Underwater-to-underwater missile

Besides these classifications, missile with guidance system can be classified with respect to types of the flight control method. These are canard control, wing control, tail control, and unconventional flight control. In tail control alternative, control surfaces are located at tail. This type of systems, need to be integrated into a launch platform and they may also have fixed wings, strakes or canards. For canard and wing control systems, there are additional control surfaces to tail control surfaces. Finally, unconventional control alternative includes thrust vector control with jet interaction. In Figure 1, four main types of guided missiles are given in terms of the control methods [2].

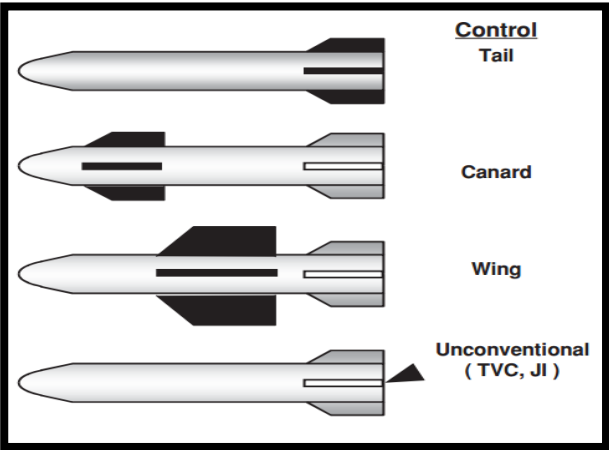


Figure 1 Guided Missile Control Types [2]

Missiles are typically five main sections including guidance system, warhead, propulsion system, autopilot, and control actuation system. The guidance system is a system that receives information from its launch controller and directs the missile to the target. This system also transmits all missile functions to its launch controller for monitoring the missile performance. The warhead is explosive section of missile containing destroying materials in order to destroy the target. The autopilot system provides some flight information such as missile location, direction, velocity and altitude in order to direct motion of missile via control surfaces. The propulsion system is a system that provides thrust throughout the flight. It includes a mixture of chemical fuels.

This system is also responsible for propelling the missile from its launcher. Finally, the control actuation system is a system that directs the missile via received information from the autopilot and guidance section. It has fins or control surfaces in order to change direction of missile during the flight. The main sections of missile are shown in Figure 2.

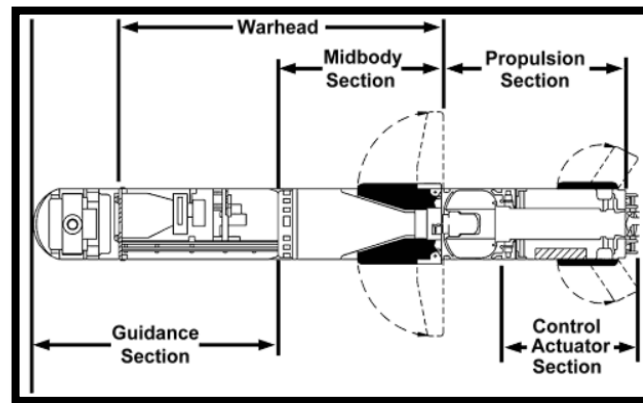


Figure 2 Javelin Medium Anti-Armor Weapon System [3]

Calculation of aerodynamic forces and moments is a significant issue for missile design process. To obtain an accurate solutions for aerodynamic coefficients and forces cause the cost reduction and saving on time. However, calculation of these is a difficult process for missile design due to some aerodynamic problems such as excessive aerodynamic heating, high range of flight velocity and high pressure distribution on missile body. Due to the various mission requirements, there are many missile designs in defense industry. In missile design, apart from designing conventional airplanes, different aerodynamic sign conventions are utilized so as to define aerodynamic forces and moments. In a six degree of freedom coordinate system, these forces and moments acting on missile are shown in Figure 3.

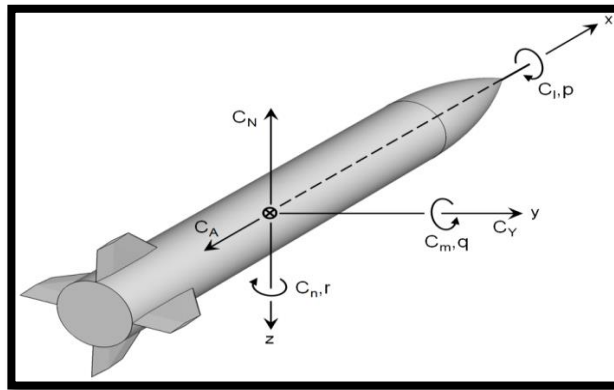


Figure 3 Forces and moment coefficients in six D.O.F. systems [4]

## 1.2 Aeroelasticity

During the missile design processes, there are some constraints that restrict the designers such as aeroelasticity. Aeroelasticity is the interaction between aerodynamics and structural mechanics composed of static and dynamic aeroelasticity. While dynamic aeroelasticity deals with dynamic response of a structure, static aeroelasticity takes care of steady-state response of an elastic structure due to the fluid structure interaction. In Figure 4, Collar's triangle of forces is shown in order to define relation between aerodynamic, elastic and inertial forces [5].

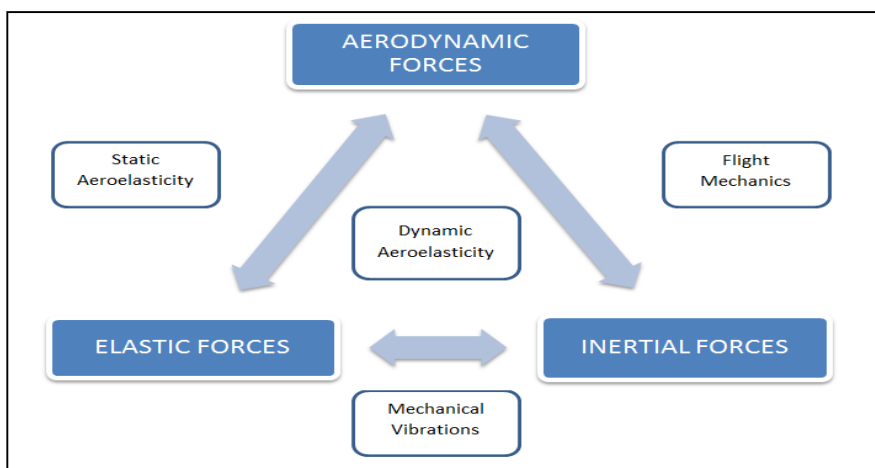


Figure 4 Collar's Aeroelasticity Triangle [5]

Aerodynamic loads may cause structural fatigue and failure problems for an aerospace structure such as a missile exposed to coupled aerodynamic loads varying with the velocity profile.

Static aeroelasticity is related with the interaction among aerodynamic and elastic forces. The main points of interest of this discipline are divergence, load distribution and control surface reversal. Divergence is a static instability condition of a lifting surface of an air vehicle during the flight. It occurs at a specific speed called the divergence speed. Load distribution is an influence of the pressure distribution over the structure. Control surface reversal is a condition which occurs at control reversal speed. It is related with the effects of an elastic deformation on control surfaces such as aileron, rudder and elevator.

On the other hand, dynamic aeroelasticity is a phenomenon including flutter, buffeting and dynamic response. Flutter is a dynamic instability occurring at a specific flight speed called flutter speed. Then, buffeting is transient vibration of an aircraft component due to the aerodynamic impulses. Finally, dynamic response is a transient response of a structure created by gust, landing, gun reactions etc. [5]. Fields of aeroelasticity is shown in Figure 5.

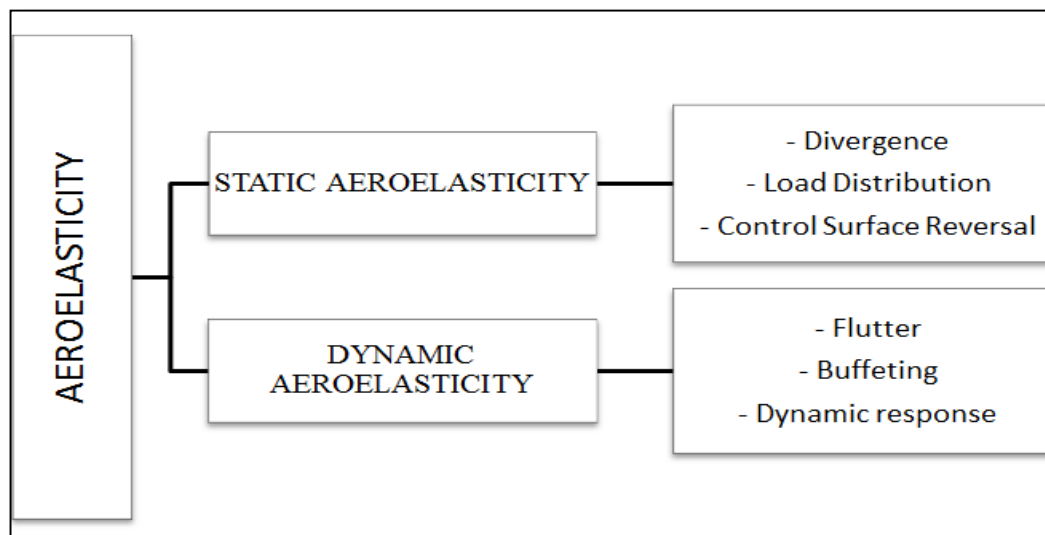


Figure 5 Fields of Aeroelasticity

### **1.3 Composite Materials**

For missile structural design, composite materials are highly used in industry. Composite materials consist of two or more materials that have different chemical and physical properties. Recently, they are highly used in aerospace industry due to some design requirements such as high strength and minimum weight requirements. Composite laminates consist of layers of fibrous composite materials and the failure characteristics of these highly need to be considered in order to utilize strength of a composite structure. The main advantage of composite structures is that they show the best properties of their constituents. In other words, there are some properties of a design that can be developed by constituting a composite structure such as, strength, stiffness, corrosion resistance, weight, fatigue life and thermal insulation. There are four commonly accepted types of composites which are fibrous composites including matrix and fiber materials, laminated composite materials composed of layers of different materials, particulate composite materials and combination of these three kind of composites. Fibrous materials are materials that consist of fibers with high modulus and surrounding materials called matrix. Fibers are geometrically defined by their very high length-to-diameter ratio. Strengths of fiber elements are very high in comparison to common structural elements such as aluminum. However, it is not possible to compare fibers and common used structural materials because fibers have to be used with matrix materials in a structural member [6]. In Table 2, different fiber materials are compared with commonly used structural materials in terms of their densities, strengths and stiffness.

Table 2 Fiber and wire properties [7]

Fiber or Wire	Density [kN/m <sup>3</sup> ]	Tensile Strength [GN/m <sup>2</sup> ]	Tensile Stiffness, E [GN/m <sup>2</sup> ]
Aluminum	26.3	0.62	73
Titanium	46.1	1.9	115
Steel	76.6	4.1	207
E-Glass	25.0	3.4	72
S-Glass	24.4	4.8	86
Carbon	13.8	1.7	190
Graphite	13.8	1.7	250

Fibers have limited usage without bonding with a structural element that holds them together which is called matrix. Matrix supports fibers and transfers the stresses between them. It is generally considered as the material with lower density, stiffness and strength. However, the combination of matrix and fibers has very high stiffness and strength. The structures of matrix materials can be polymers, ceramics, metals or carbon. Laminated composite materials are composed of at least two layers with different materials which are bonded together. Lamination is used to combine best properties of layers in a composite structure. These aspects can be stiffness, weight, corrosion resistance, thermal insulation etc. A laminated composite consisting of 4 layers is shown in Figure 6.

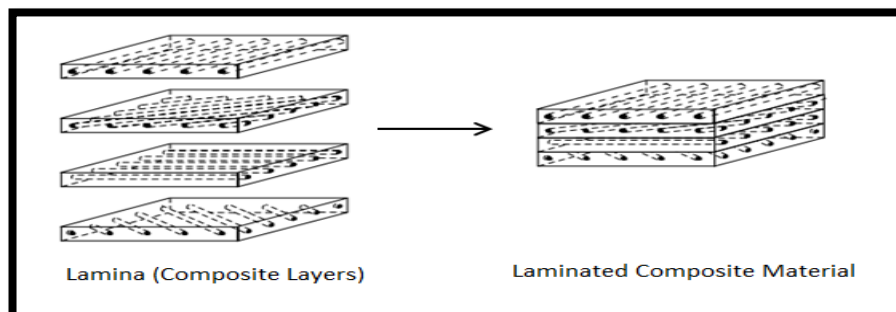


Figure 6 Laminated composite structure [8]

Particulate composite materials are composed of particles which can be metallic or non-metallic. These particles are used in a matrix material and the final product of matrix and particles has lower stiffness and strength in comparison to fibrous composite materials because load is mainly carried by the matrix material. However, in fibrous composites, matrix provides support and protection for fibers and helps for load distribution between fibers, so desirable strength and stiffness can be provided [8].

#### **1.4 Aim of Thesis**

In this study, laminated composite missile fins are investigated in terms of strength varying with the aerodynamic profile. The main goal of this study is to examine whether the laminated composite control surfaces with modified-double wedge cross-sections fail or not under maximum aerodynamic loads by performing one-way static aeroelastic analyses. Another purpose of this study is to investigate different stacking sequences of control surfaces consisting of carbon/epoxy composite layers in order to minimize the maximum deflection and increase the carried load capacity. By considering the geometric constraints of missile body, two different cross-section of control surface are investigated in terms of their strengths and maximum deflection under maximum aerodynamic pressure. In order to obtain aerodynamic loads and moments, two missile models analyzed at different angles of attack and constant supersonic speed. After performing CFD analyses, less deformable ply orientations are obtained by using an algorithm written in Matlab®. All ply orientations are investigated by Tsai-Wu, Tsai-Hill, Maximum Stress and Hoffman failure criteria. Then, the three configurations of both control surface models are manufactured and tested to compare the tip deflections.

## CHAPTER 2

### LITERATURE SURVEY

In literature, there are many studies on static aeroelasticity of a missile and stacking sequence optimization of laminated composites. In this chapter, a review study on these topics is carried out. The most related studies which is utilized in this study are introduced.

Yang [9] carried out an analysis on composite canards exposed to static aerodynamic loads. He modelled the canard as a symmetrically laminated structure formed by graphite/epoxy lamina. In this study, an iterative code was developed in order to examine the interaction between the aircraft canard and aerodynamic loads. The canard model with 2-D shell elements was also optimized in terms of the ply orientation of laminate. It was revealed that, transverse shear stresses are considerably larger than in-plane stresses. In CFD part of the study, panel method was preferred to describe the fluid and obtain the aerodynamic loads. Moreover, in structural part, GA (genetic algorithm), CONMIN (Constrained Function Minimization) and Hybrid optimizer were used in order to optimize the ply orientation and ply thickness of laminated composite canard. These optimizer algorithms, were compared with respect to accuracy, convergence criteria and computational costs.

Kim et al. [10] investigated the optimal ply orientation of a laminated composite plate. To calculate the stresses classical lamination theory was used.

Tsai-Wu failure criterion was taken into consideration in the optimization procedure of stacking sequence of the structure. Also, a sensitivity analysis was carried out by using finite difference (FDM) and adjoint variable method. Authors concluded that, adjoint variable method provided more accurate results than FDM.

Lopez et al. [11] used a genetic algorithm to optimize the stacking sequence and weight of laminated composite plates exposed to in-plane loads. Different failure criteria which are Tsai-Wu, Maximum Stress and Puck were compared in order to decide weight reduction of the plate.

Harrison and Johnson [12] developed a formulation to predict interlaminar stresses in thickness-tapered laminated composite plate. By using and modifying Pagano's methodology, stress fields were determined for a tapered plate. Also, parametric studies were performed to analyze the ply-drop laminates under different loads. This shows that, the stiffness of the dropped plies has a significant influence on interlaminar stresses.

Rajanish et al. [13] performed a study on different failure criteria of laminated composite plates. The experimental results were compared with the analysis results encompassing Tsai-Wu, Tsai-Hill, Hashin, Hashin-Rotem and Maximum Stress failure theories. It was noticed that, Tsai- Wu, Tsai-Hill and Hashin methods are more close to experimental results than others.

In a review paper of Burk [14] in 1983, reviewing failure criteria usage in failure analyses, 80% of the people performing failure analysis on composite structures utilize Tsai-Wu, Tsai-Hill, Maximum Stress and Maximum Strain failure theories. The most commonly used one is Maximum Strain theory and its percentage of usage is 30%. Maximum Stress theory is ranked at the second with 22%. Tsai-Hill and Tsai-Wu usages are 17% and 12% respectively.

Sun et al. [15] evaluated the commonly used failure criteria for both a single lamina and under different loads in order to characterize and compare these criteria. Hashin, Hashin-Rotem, Tsai-Hill, Tsai-Wu, Maximum Stress and Strain failure theories was compared in this study. It was concluded that, at a single layer level, the criteria which distinguish the fiber and matrix failure modes are more precise. While Hashin-Rotem, Maximum Stress and Maximum Strain failure criteria give more accurate results for fiber-dense laminates, Tsai-Wu, Tsai-Hill and Hashin methods are more reliable for matrix –dominated laminates. Also, it was recommended that, in order to foresee lamina matrix failure of a laminate, transverse and shear strengths should be utilized.

Olcay [16] performed a study at progressive failure methodology for composite of shells. In this study, nonlinear finite element code for large deformations was developed. Maximum stress, Tsai-Wu and Hashin’s failure theories were compared in different cases. It was revealed that first ply failure loads were acquired in increasing order by Tsai-Wu, Hashin’s and Maximum Stress failure criteria. Also, a maximum stress criterion is the least conservative failure criterion for all cases in terms of first ply and ultimate failure loads.

Celik [17] evaluated tapered laminates exposed to tensile loading in his study. In order to survey performance of tapered laminated composites, Hashin’s failure criteria with progressive failure analysis was utilized for in-plane failure modes and cohesive zone method was used for out-of –plane failure modes.

Akbulut and Sonmez [18] studied at weight optimization of composite laminates. In this study, a laminated plate exposed to in-plane and out-of-plane loading was modelled in order to obtain an optimized ply orientation and number of ply of the structure. Tsai- Wu and maximum stress failure theories were utilized during the optimization part of the study. It was emphasized that in some cases, the optimization routine was failed when both theories were utilized individually.

In order to avoid this situation Tsai-Wu and maximum stress criteria were used together in the algorithm.

Lee [19] performed a comparative study for supersonic exhaust jet-flows by using four base eddy viscosity turbulence models which are Spalart-Allmaras, Wray-Agarwa, Standart  $k-\epsilon$ , Shear Stress Transport  $k-\omega$  models. The analyses results were compared with experimental results by modelling Putnam, Seiner and Eggers nozzles. Author concluded that, the accurate prediction of boundary layer profile is required at jet exit in order to obtain better performance of  $k-\epsilon$  turbulence model with low Reynolds number.

Sumer [20] developed a static aeroelastic model for complicated aircraft wing geometries. In this study, an iterative solution as utilized in order to adapt mesh to the deformed wing body. Agard Wing 445.6 was modelled so as to contrast analytical results with test results. Distribution of pressure coefficients across the wing body and edge displacements are obtained by using computational aeroelastic model. It was deduced that deflection due to bending reduced the lift and its coefficient.

Newman et al. [21] performed a study at high-fidelity static aeroelastic analysis. In this study, nonlinear Euler equations and finite element method were used to model aerodynamic loads. In order to identify the solution domain of fluid, unstructured tetra grids were utilized. The aeroelastic response of subsonic, transonic and supersonic flow regimes were obtained statically. According to this study, the case of transonic flow regime shows that there is a significant loss of lift force due to the large deflection of the wing.

Inci [22] optimized the continuous path and discrete ply angle orientation of a composite structure. In this study, there are two methods which are gradient based method by a module of Nastran and genetic algorithm working with Nastran finite element solver in order to carry out the optimization.

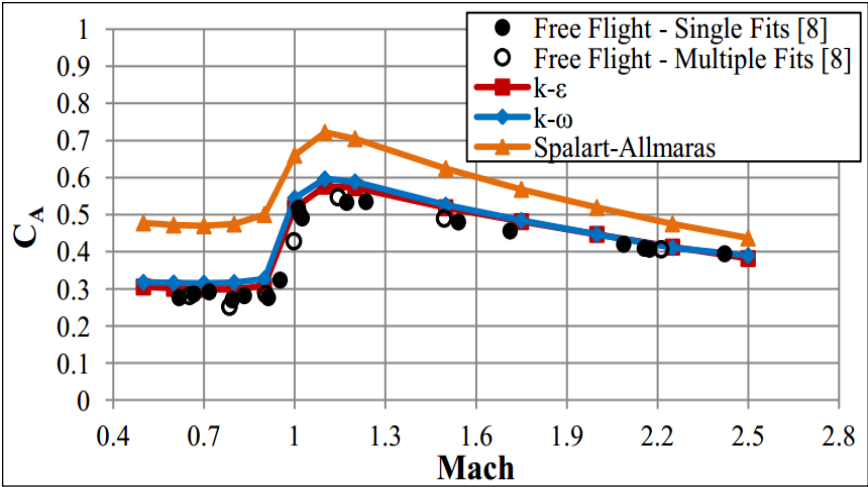
It is revealed that genetic algorithm gives more accurate results than optimization module of Nastran. Also, it is stated that discrete fiber orientation optimization gives a better optimum result than continuous fiber path optimization because the each element is designated an angle of fiber orientation for discrete fiber orientation optimization.

Dillinger [23] made an investigation about static aeroelastic optimization of laminated composites with variable stiffness. In this study, there are two basic parts which are stiffness optimization and design of the wing aeroelastic constraints. In the procedure of stiffness optimization part, a parametric model generator was set up to derive finite element, mass and doublet lattice models. Doublet lattice method is an aerodynamic computing method which calculates surface pressure of aerodynamic model. By using this method, a wing planform was modeled with flat trapezoidal panels in order to obtain aerodynamic pressure. Then, in the wing design part, a model to optimize was prepared and mass minimization study was performed.

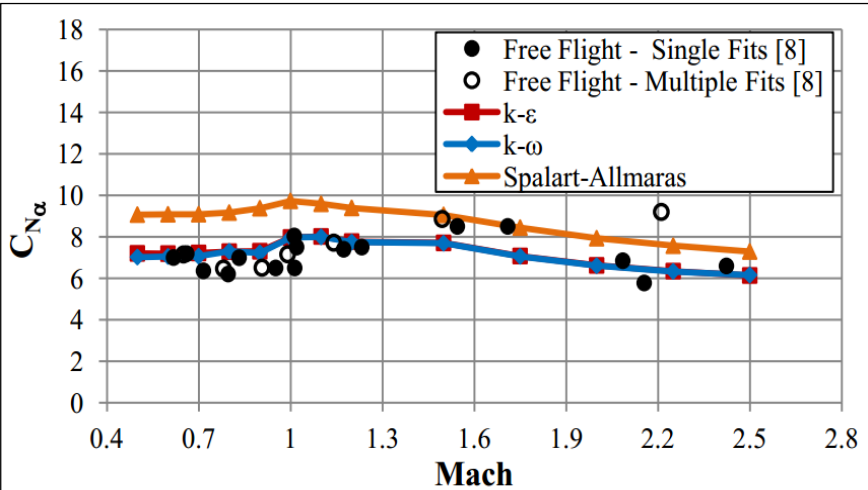
Ozkaya and Kayran [24] developed a nonlinear aeroelastic model for the composite missile fins with intralaminar and interlaminar damage. In this research, two-way fluid structure interaction analyses were performed in order to investigate failure modes of composite missile fins. For case verification, Agard wing 445.6 wing model was utilized at critical Mach number. Laminated composite missile fin was modeled by using the Ansys ACP tool. It is revealed that, delamination of leading or trailing edge is taken into consideration since it is more possible due to manufacturing processes. Moreover, interlaminar and intralaminar damages were examined together so as to simulate the worst case. It is concluded that, total coefficient of lift had been decreased dramatically in comparison to undamaged case.

Kayabasi [4] performed a validation study for Modified Basic Finner (MBF) model with four fins. In this study, CFD results obtained from different turbulence models were compared with experimental data. During this study, Spalart-Allmaras,  $k-\epsilon$  and  $k-\omega$  turbulence models were examined.

Analytical results were compared with test data of free flight at varying velocity profile in terms of axial force coefficient, normal force coefficient slopes and the slopes of pitching moment coefficient. According to this study, for supersonic flow regimes closer results to the test data were acquired by using k-  $\epsilon$  turbulence model. In Figure 7, axial force coefficient and normal force coefficient slope variations with Mach number are shown.



a) Axial force coefficient



b) Normal force coefficient slope

Figure 7 Turbulence Models comparative study [25]

Aslan et al. [25] performed a study about static aeroelastic modeling of a laminated composite missile fin. In this study, missile fin with double wedge cross-section was modeled in order to minimize the tip deflection under aerodynamic loading. An optimization study was carried out in terms of ply orientation of the laminated composite fin by considering the Tsai-Wu failure criterion. This fin with unidirectional layers is also tested. Least deformable 5 ply orientations obtained from the optimization study are shown in Table 3.

Table 3 Least deformable 5 orientations of optimization study [25]

<b>Stacking Sequence [°]</b>	<b><math>\sigma_{1,max}</math> [MPa]</b>	<b><math>\sigma_{2,max}</math> [MPa]</b>	<b><math>\sigma_{12,max}</math> [MPa]</b>	<b><math>\delta_{max}</math> [mm]</b>
[15/0/15/0/0] <sub>s</sub>	508.21	7.70	11.62	4.031
[0/15/15/0/0] <sub>s</sub>	538.61	7.94	12.30	4.033
[0/0/15/0/0] <sub>s</sub>	506.89	7.69	11.55	4.036
[30/0/15/0/0] <sub>s</sub>	512.43	7.74	10.96	4.052
[0/0/0/15/0] <sub>s</sub>	535.50	8.45	18.00	4.058



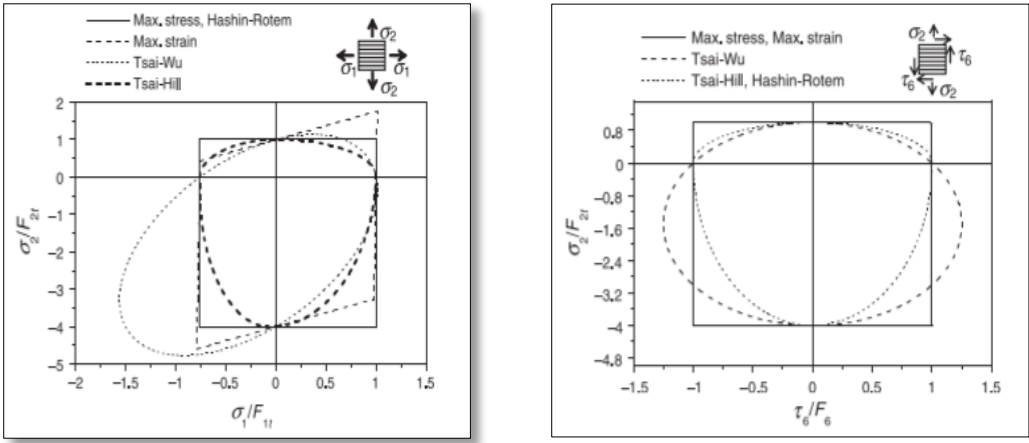
## CHAPTER 3

### FAILURE THEORIES

Failure theories are the field of foreseeing whether the solid material fails or not under the external loads. When the applied load is over the maximum load capacity carried by the solid material, the failure takes place. Since testing of a material in each state is not cost effective process in engineering, failure criteria are used to predict defects in structures. In composite materials, failure mechanism is investigated in micromechanical and macro-mechanical levels. While micromechanics of failure deal with fiber and matrix failure in a layer of composites, macro-mechanics of failure handles delamination of composite structures.

In multilayered composites, evaluating failure theories is more difficult than single layer composites. The scope of failure analysis of laminated composites includes failure theory of a lamina for prediction of first ply failure, progression of failure in laminated structure after first ply failure, a criterion for maximum load or ultimate ply failure [26]. The composite failures occur when damage in fibers, crack in matrix, debonding in a layer or delamination are observed under external loads. In literature, there are some studies so as to examine intra-laminar failure in composites. For instance, Falzon and Appruzzese [27] performed an analytical analysis of interlaminar failure mechanism for composites by implementing a finite element model. In this study, a 3D model was developed for determining the interlaminar failure initiation, growth and ultimate failure loads by using a finite element program of Abaqus.

The non-linear stress and strain relations for a single-layered composite were taken into consideration under compressive transverse loads. The purpose of this study is to implement an implicit solution to the model. Daniel [26] investigated failure theories and its procedures to predict and analyze failure in composite structures. In this study, both laminate and lamina failures are examined. At the part of single layer failure, Tsai-Wu, Tsai-Hill, Hashin-Rotem, Maximum stress and strain failure theories were compared by means of failure envelopes for different materials and different stress states. Figure 8 shows the failure envelopes of UD Carbon/Epoxy lamina under normal and shear loading by using the different failure theories. According to the Figure 8.a, Tsai-Hill is most conservative than other failure theories used in this study when a single layer of composite is subjected to biaxial normal tension ( $\sigma_1 > 0, \sigma_2 > 0$ ) and compression ( $\sigma_1 < 0, \sigma_2 < 0$ ). On the other hand, as it is seen in Figure 8.b, Tsai-Hill is most conservative failure criterion for a lamina which is subjected to transverse shear and compression while Tsai-Wu is most conservative for a lamina under transverse shear and tension.



a) Under biaxial normal loading      b) Under transverse normal and shear loading

Figure 8 Failure envelopes for UD carbon/epoxy (AS4/3501-6) lamina [27]

In the light of this information, this study approaches the intra-laminar failure of composites under maximum aerodynamic loads at supersonic velocity profile.

In order to perform a parametric study for ply orientation and determine the least deflected composite missile fin, Maximum Stress, Tsai-Hill, Tsai-Wu and Hoffman failure criteria are utilized.

### 3.1 Maximum Stress Failure Criterion

Maximum Stress Failure Criterion evaluates whether the stresses on composite structures exceed the allowable stress or not. In other words, this criterion directly compares the stress components with specified critical stresses by assuming that there is no interaction between the stress components acting on lamina [28].

There are two different failure conditions shown in Eq. (1-5).

Fiber Failure:

$$\sigma_1 \geq X_t \quad (1)$$

$$|\sigma_1| \geq X_c \quad (2)$$

Matrix Failure:

$$\sigma_2 \geq Y_t \quad (3)$$

$$|\sigma_2| \geq Y_c \quad (4)$$

$$\sigma_{12} \geq S \quad (5)$$

Note that, in all failure equations presented in this study, “1” and “2” components of stress symbols symbolize fiber and transverse directions respectively. The material strength components which are tensile, compressive and shear strengths are denoted by “X”, “Y” and “S” respectively. Also, “t” and “c” represent the direction of tension and compression.

### 3.2 Tsai- Hill Failure Criterion

This criterion is extended version of yield criterion of distortional energy called von-Mises yield criterion, for anisotropic materials [29]. Hill performed an extension to von-Mises criterion for anisotropic materials, and Tsai applied this theory o to unidirectional lamina by assuming the compressive and tensile strength of composite materials are equal [30].

The governing equation of Tsai-Hill theory is given in Eq. (6). According to this theory, “FI” term called as failure index, must be less than one in order to say that the material does not fail. This equation does not consider a difference between tensile and compressive strength so, it is noted that the appropriate values of tensile and compressive strength of material in longitudinal and transverse direction which are “ $X_t$ ”, “ $X_c$ ”, “ $Y_t$ ”, “ $Y_c$ ”, have to be used depending on the sign of  $\sigma_1$  and  $\sigma_2$  [6].

$$FI = \frac{\sigma_1^2}{X^2} - \frac{\sigma_1\sigma_2}{X^2} + \frac{\sigma_2^2}{Y^2} + \frac{\sigma_{12}^2}{S^2} \quad (6)$$

### 3.3 Tsai-Wu Failure Criterion

Tsai-Wu failure criterion is commonly used in failure analysis of composite structures. This criterion is the extension of Tsai-Hill criterion by adding the number of terms in the failure index equation. [31] There is a basic assumption that a failure surface exists in the stress-domain in the scalar form shown in Eq. (7). According to this theory, failure index denoted as “FI” defined in Eq. (8) must be less than one. Otherwise, the composite structure fails. The strength parameters, F terms in equation, must be determined by experiment [32].

$$F_i + F_{ij}\sigma_i\sigma_j = 1 \quad i, j = 1, 2, \dots, 6 \quad (7)$$

$$FI = F_1\sigma_1 + F_{11}\sigma_1^2 + F_2\sigma_2 + F_{22}\sigma_2^2 + F_{66}\sigma_{12}^2 + F_{12}\sigma_1\sigma_2 \quad (8)$$

Where

$$F_1 = \frac{1}{X_t} - \frac{1}{X_c} \quad F_{11} = \frac{1}{X_t X_c} \quad F_2 = \frac{1}{Y_t} - \frac{1}{Y_c} \quad F_{22} = \frac{1}{Y_t Y_c} \quad F_{66} = \frac{1}{S^2} \quad (9)$$

And the interaction coefficient is shown in Eq. (10).

$$F_{12} = -\frac{1}{2\sqrt{X_t X_c Y_t Y_c}} \quad (10)$$

### 3.4 Hoffman Failure Criterion

Hoffman Failure theory is a form of Tsai-Hill failure criterion. In Tsai-Hill failure theory, strength parameters are acquired by neglecting difference between tension and compression. However, Hoffman added some linear terms so as to differentiate tension and compression strength components. For the plane stress, the governing equation of this theory is given in Eq. (11) [6].

$$FI = -\frac{\sigma_1^2}{X_c X_t} + \frac{\sigma_1 \sigma_2}{X_c X_t} - \frac{\sigma_2^2}{Y_c Y_t} + \frac{X_c + X_t}{X_c X_t} \sigma_1 + \frac{Y_c + Y_t}{Y_c Y_t} \sigma_2 + \frac{\sigma_{12}^2}{S^2} \quad (11)$$

According to Hoffman theory, “FI” term called as failure index, have to be less than one in order to say that the material does not fail under exerted loads. Note that, for equal tensile and compressive strength terms, this theory turns into Tsai-Hill failure theory in Eq. (6).



## CHAPTER 4

### CFD MODELING AND WIND TUNNEL TESTING

#### 4.1 Methodology and Geometry Description

In this study, a surface-to-surface missile with laminated composite control surfaces is modeled with respect to static aeroelastic response. First of all, 3D CFD analyses at different angle of attack are performed in order to obtain maximum pressure distribution on control surfaces.

The missile geometry used in this study, has four main parts which are nose, body, fixed wings, control surfaces. The nose contains seeker and the body consists of guidance-autopilot system, warhead and flight motor parts. In analyses part, two main missile models are used. The only difference between these is cross-sections of control surfaces. The control surfaces used in both cases, have same span lengths, thicknesses and chord lengths. However, they have different cross-sections although they are both modified double-wedged type control surfaces. In this way, both control surfaces are compared in terms of the aerodynamic and structural performances.

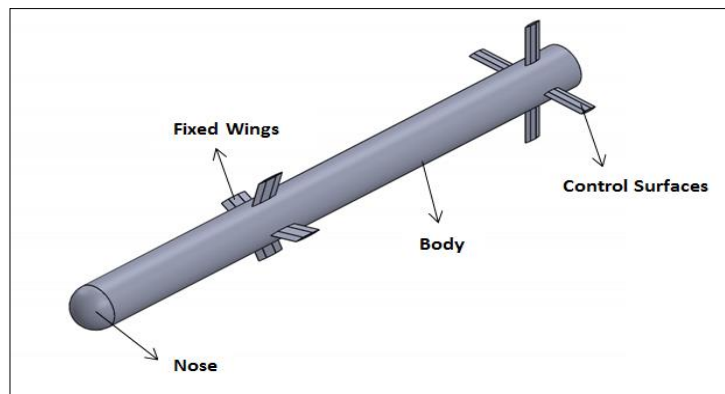


Figure 9 Parts of missile Model

The general dimensions of missile are shown in Figure 10. The missile length is 1040 mm, and body diameter is 80 mm. Fixed wings are swept wings with the angle of  $20^\circ$ .

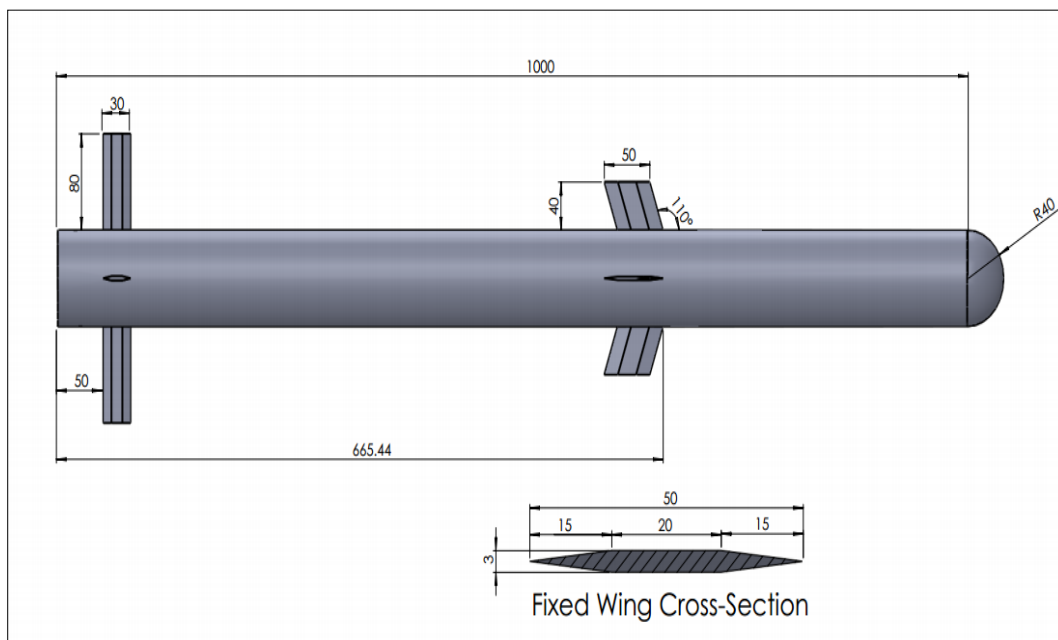


Figure 10 Missile and fixed wing dimensions (mm)

#### 4.1.1 Model 1

In model 1, control surfaces have double wedges with %60 of the chord length and a flat surface with %40 length of chord. In this model, chord length of control surfaces is 30 mm, thickness is 3.6 mm wedge lengths are 9 mm and flat surface length is 12 mm. The cross-section of Model-1 is shown in Figure 11.

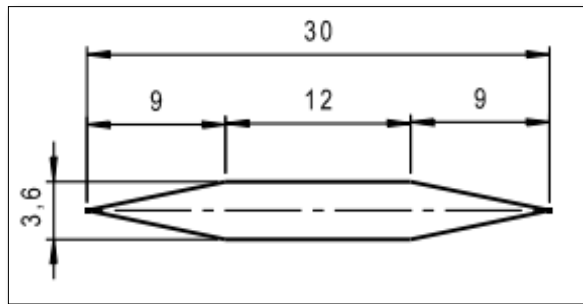


Figure 11 Control surface dimensions of missile model-1

#### 4.1.2 Model 2

In model 2, control surfaces have double wedges with %80 of the chord length and a flat surface with %20 length of chord. In this model, chord length of control surfaces is 30 mm, thickness is 3.6 mm wedge lengths are 12 mm and flat surface length is 6 mm. The cross-section of Model-1 is shown in Figure 12.

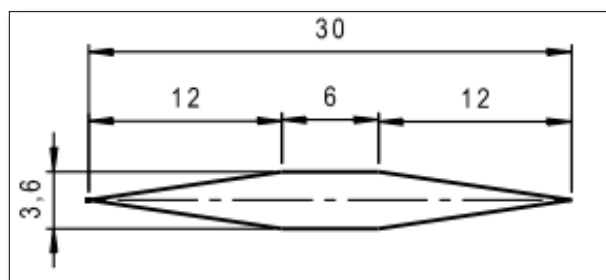


Figure 12 Control surface dimensions of missile model-1

### 4.1.3 CFD Grid Generation

In CFD analyses, unstructured elements are used in order to obtain a better model. First of all, boundary layers of missile and faces of outer domain are modeled with triangular surface elements in Gambit®. Face size functions are used in order to obtain low skewness and high element quality. In mesh generation part, mesh refinement study is performed. For better turbulence modeling, boundary layers are modeled by prism elements with TGrid®. In both coarse and fine mesh cases, 20 layers are generated on missile surfaces. After forming surface meshes and boundary layers, volumetric tetrahedral elements are generated by using TGrid®. Number of elements, faces and nodes is shown in Table 4 for both coarse and fine meshes of Model-1 and Model-2. The number of wedge and tetrahedral elements is given in Table 5 for both control surface models.

Table 4 Mesh Refinement Study

	Grid	Number of Element	Number of Face	Number of Node
Model-1	Fine	9513067	20667999	2668249
	Coarse	5263478	12567432	1496470
Model-2	Fine	8835488	19167609	2460812
	Coarse	4985231	11598741	1368723

Table 5 Wedge and tetrahedral elements in missile models

	Element Type	Number of Elements
Model-1	Wedge	2848420
	Tetrahedral	5986568
Model-2	Wedge	3112400
	Tetrahedral	6400667

The grid of the model-1 for fine mesh and its boundary layers for nose, fixed wing and control surface are shown in Figure 13.

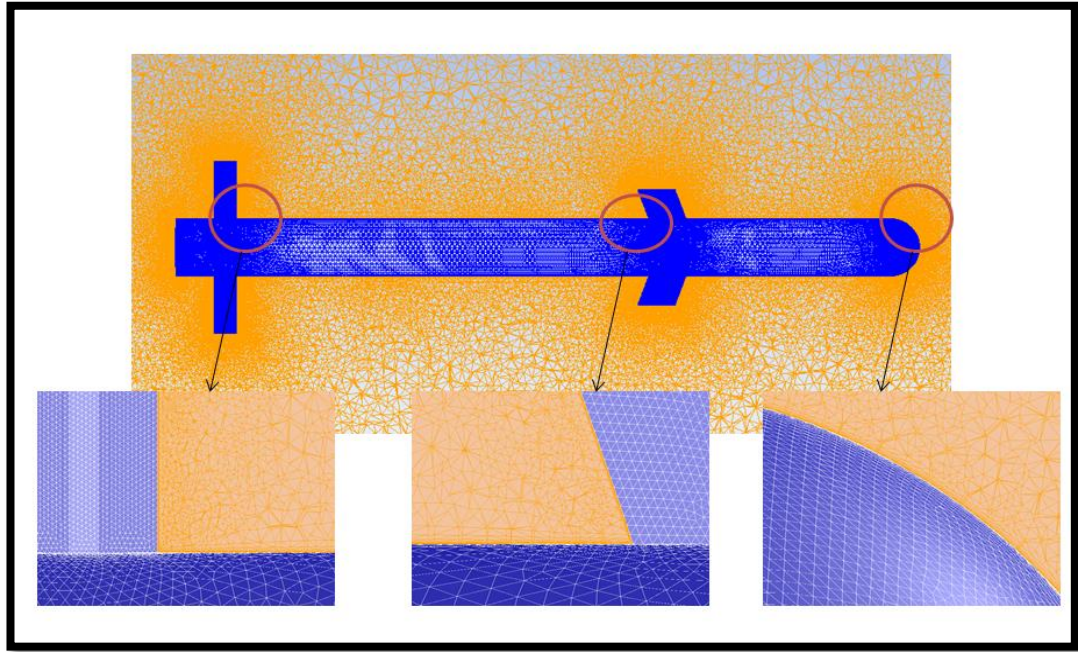


Figure 13 Fine grid details

#### 4.2 Grid Quality Analysis

The grid quality and number of elements affect the convergence and results of the CFD analyses. So as to obtain better solution, the grid quality has to be fine enough. For CFD analyses, two aspects of quality are mostly used which are skewness and aspect ratio. The aspect ratio of a cell is defined as the ratio of the longest edge length to shortest edge length. For an ideal cell, the aspect ratio should be close to 1. Then, skewness is a quality measurement whether an element is appropriate to ideal form [33]. In other words, skewness is a ratio of the difference between optimal cell size and cell size used in mesh model to the optimal cell size. Skewness ratio is given in Eq. 12.

$$\text{Skewness} = \frac{\text{Optimal Cell Size} - \text{Cell Size}}{\text{Optimal Cell Size}} \quad (12)$$

According to skewness measurement method, 0 value of skewness is the ideal form, and 1 is the worst element quality. In Table 6, skewness ratio range with respect to grid quality is shown.

Table 6 Skewness ratio with respect to element quality [34]

Value of Skewness	Cell Quality
1	Degenerate
0.9-1	Bad
0.75-0.9	Poor
0.5-0.75	Fair
0.25-0.5	Good
0-0.25	Excellent
0	Equilateral

In CFD analyses part, skewness of all elements is examined for both model-1 and model-2. Skewness with the element distribution are given in Figure 14 and 15.

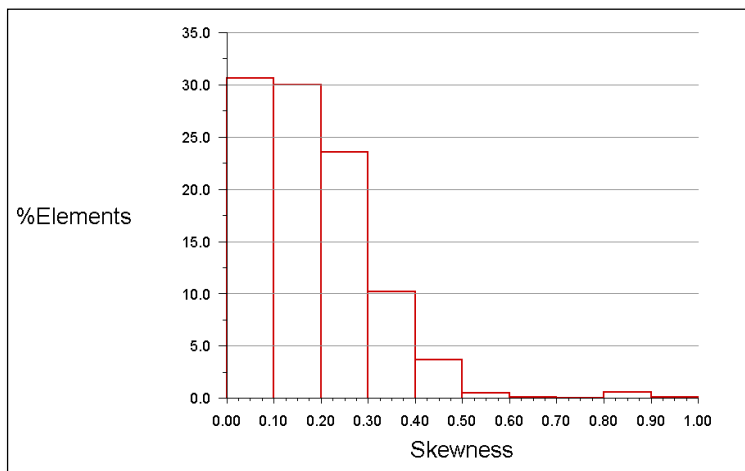


Figure 14 Skewness ratio of Model-1

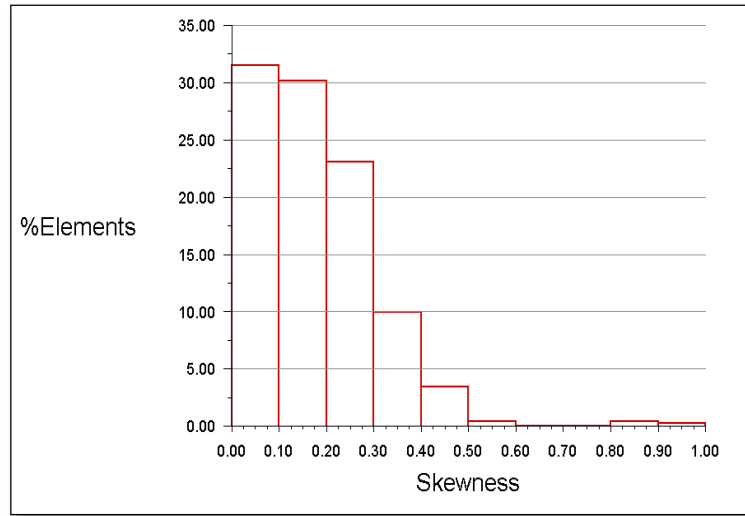


Figure 15 Skewness ratio of Model-2

### 4.3 Boundary Layer Model

Turbulent boundary layer consists of some sub-layers. In order to obtain better turbulence model,  $y^+$  calculation is required.  $y^+$  is a non-dimensional distance to describe distance to the wall boundary condition. It is important in turbulence modeling to determine the proper size of the cells near domain walls. Turbulent region is divided into three main sublayers in terms of the  $y^+$  values namely viscous sublayer, buffer layer and fully-turbulent region. The outer region of turbulent boundary layer is called fully-turbulent region or log-law region. The layer near wall is called viscous sublayer. The layer between viscous sublayer and fully turbulent region is named buffer layer or blending region. In turbulent flow modeling, it is recommended that  $y^+$  values are equal or less than 1 for enhanced near-wall modeling [34].  $y^+$  values of turbulent region are shown in Figure 16.

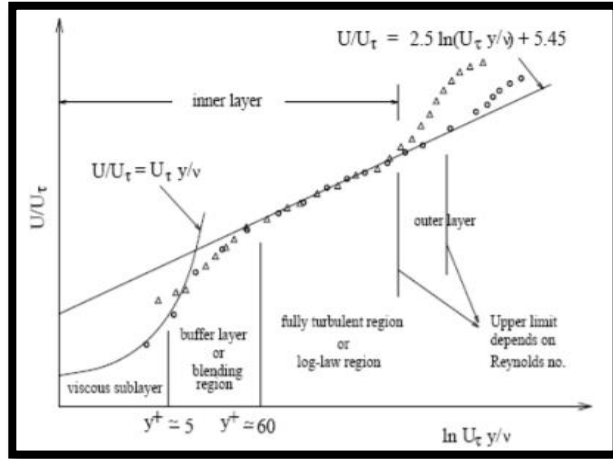


Figure 16  $y^+$  values of turbulent layers [35]

In CFD Analysis part, the operating conditions at sea level altitude is utilized [36]. The used conditions are shown in Table 7.

Table 7 Operating Conditions [36]

Altitude [m]	0
Atmospheric Pressure [Pa]	101325
Air Density [kg/m <sup>3</sup> ]	1.225
Dynamic Viscosity [N.s/m <sup>2</sup> ]	1.79x10 <sup>-5</sup>
Temperature [°K]	288.16
Speed of Sound [m/s]	340.3

The Reynolds number [37] is calculated in order to get  $y^+$  values lower than the 1. Thus, the first layer thickness of the turbulent boundary layer is determined in Eq. (13-17). At the first step to obtain desired first layer thickness of boundary layer, Reynolds number denoted by “Re” is calculated by Eq. 13. Then, coefficient of friction on wall boundary condition denoted by “ $C_f$ ”, wall shear stress denoted by “ $\tau_\omega$ ”, and frictional velocity denoted by “ $U_\tau$ ” are calculated by using Eq. 14, 15, and 16 respectively. Finally, desired first layer thickness denoted by “ $\Delta y_1$ ” is calculated by using Eq. 17. Note that, freestream velocity is 1.6 Mach and length of missile is 1.04 m.

$$Re = \frac{\rho V L}{\mu} \quad (13)$$

$$C_f = 0.058 Re^{-0.2} \text{ (for external flow)} \quad (14)$$

$$\tau_\omega = \frac{1}{2} \rho V^2 C_f \quad (15)$$

$$U_\tau = \sqrt{\frac{\tau_\omega}{\rho}} \quad (16)$$

$$\Delta y_1 = \frac{y^+ \mu}{\rho U_\tau} \quad (17)$$

Then, the maximum first boundary layer thickness of missile model so that  $y^+$  is equal to 1 is calculated and shown in Table 8. Note that, these values are obtained for each part of missile by using the own length of the parts when calculating Reynolds numbers.

Table 8 Maximum first boundary layer thickness of missile parts

Parts	Re	$C_f$	$\tau_\omega$ [Pa]	$U_\tau$ [m/s]	$\Delta y_1$ [m]
Nose	14904760	0.0021	387.11	17,78	8.22e-07
Fixed Wings	1863095	0.0032	586.75	21,89	6.68e-07
Body	37261899	0.0017	322.29	16,22	9.01e-07
Control Surfaces	1117857	0.0035	649.86	23,03	6.34e-07

According to Table 8 least first layer thicknesses are obtain for control surfaces when desired  $y^+$  value is 1. As a result of this, first layer thickness of the missile model should be less than 0.0006 mm to get enhanced near-wall solution.

$y^+$  values of missile parts for both model-1 and model-2 are shown in Figure 17 and 18. Note that, in order to get low skewness, transition between the elements of boundary layer and interior part for solution domain has to be smooth.

In other words, the size of the elements near boundary layers has to be very close to each other. Otherwise, there may be a convergence problem. For this reason, to decrease size of the tetrahedral elements of solution domain, desired  $y^+$  values are chosen as 0.1 by reducing the first layer height of boundary layers.

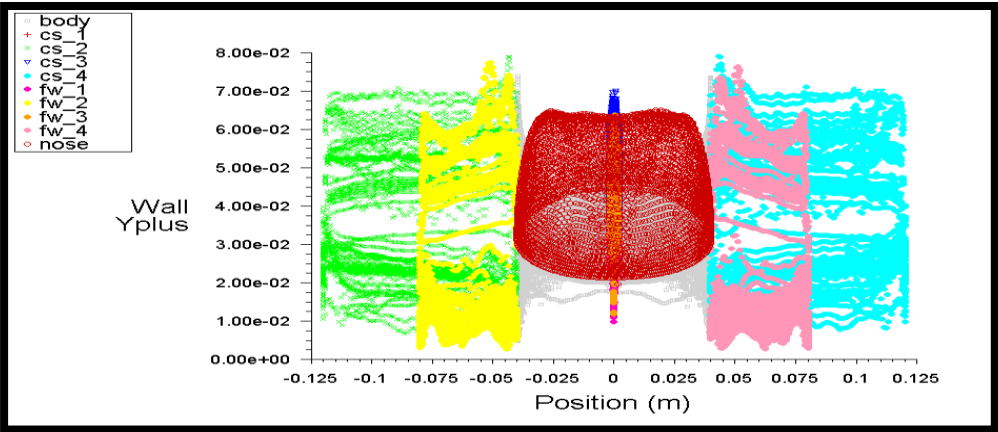


Figure 17  $y^+$  values of missile model-1

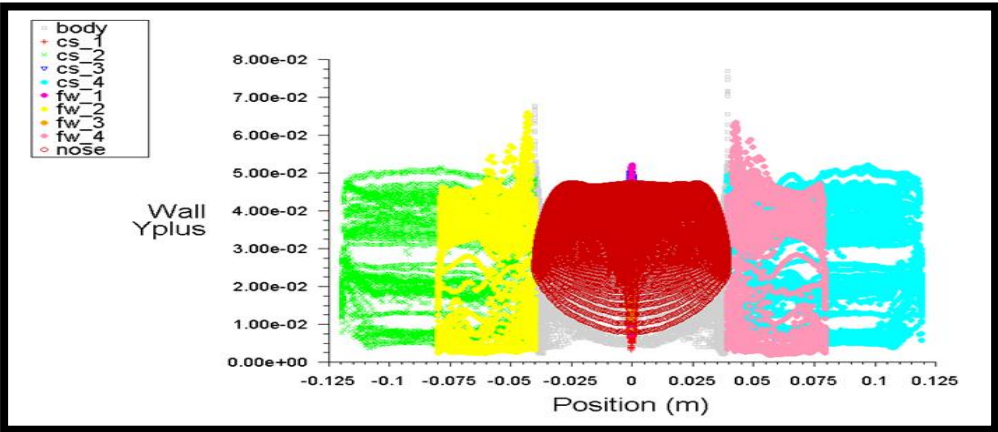


Figure 18  $y^+$  values of missile model-2

As it is seen in Figure 17 and Figure 18, solution domain of all missile parts have boundary layers with the values of wall  $y^+$  is less than 0.1 so all turbulent boundary layers shown in Figure 17, can be examined on the surfaces of both missile models.

#### **4.4 Solution Method and Boundary Conditions**

For both model-1 and model-2 steady-state CFD analyses with 3D solution domain are performed at different angle of attack respectively  $0^\circ$ ,  $3^\circ$ ,  $6^\circ$ ,  $9^\circ$ ,  $12^\circ$ ,  $15^\circ$  by using the Fluent® solver. Missile surfaces are modeled as “wall” boundary conditions. Wall boundary conditions are used to connect fluid and solid regions. In the solution including viscous flow, no-slip boundary condition is enforced at wall surfaces [38]. In this study, no-slip boundary conditions are also utilized when modeling missile surfaces as “wall”.

Outer surfaces of solution domain are modeled as “pressure far-field”. This boundary conditions help to model free-stream flow regime at infinite surface of the solution domain. In this kind of boundary conditions, free-stream velocity is defined in terms of the Mach number. This boundary condition utilizes “Riemann Invariants” in order to define flow variables at the surface of boundaries. It is highly recommended that this boundary condition is practicable when the density is obtained from the Ideal-Gas Law available in density-based solver [38]. Also, in order to obtain better turbulence modeling, k- $\epsilon$  turbulence model with enhanced wall treatment is used for turbulence modeling in CFD analyses. In this study, free-stream velocity defined in pressure far-field boundary condition is constant and 1.6 Mach.

In Figure 19 and 20, solution domain of CFD analyses and its dimensions are given. The domain is formed by a cylinder. The cylinder has 20 m diameter and 30 m height. Origin of the missile geometry is located at 10 meters away from inlet surface and at the center axis of the cylinder.

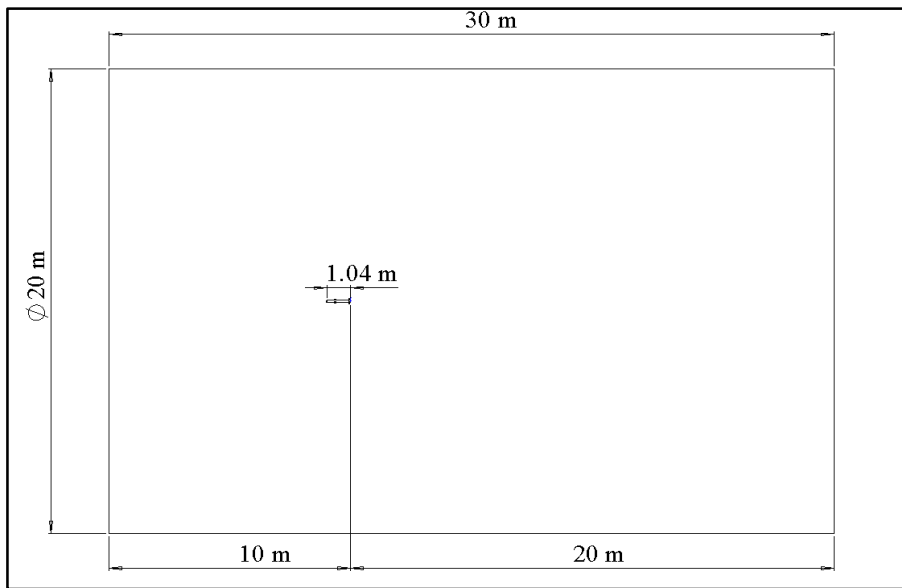


Figure 19 Dimensions of solution domain in m

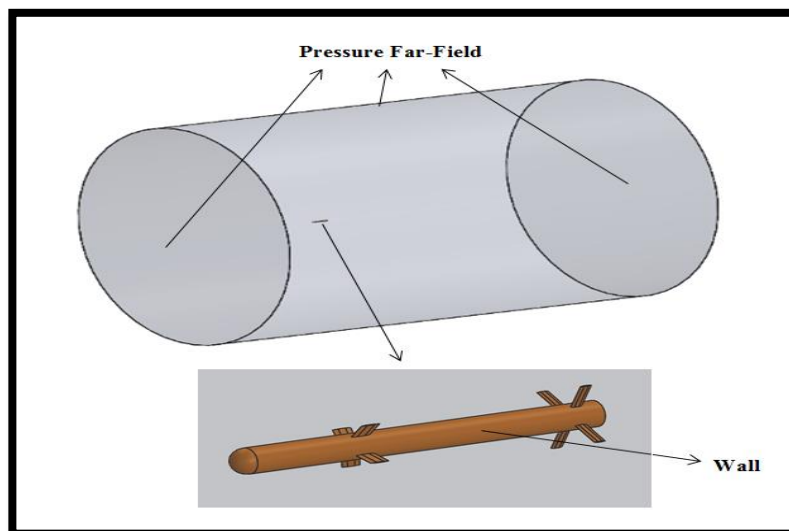


Figure 20 Solution domain of CFD

All analyses in this study, are carried out at constant flow velocity which is 1.6 Mach. Due to the supersonic flow regime, density based solution are utilized. For turbulence modeling,  $k-\epsilon$  turbulence model with enhanced wall treatment are used. Ideal gas option and Sutherland's law with three coefficient method are utilized in order to define air properties. Sutherland, in 1893, defined a correlation between the viscosity and absolute temperature for an ideal gas.

Sutherland's law depends on kinetic theory of ideal gas and it is shown in Eq. 18 and 19 [39].

$$\mu = \frac{C_1 T^2}{1 + \frac{S}{T}} \quad (18)$$

$\mu$ ,  $T$ , and  $S$  refer to dynamic viscosity, absolute temperature and Sutherland temperature of an ideal gas respectively. Also,  $\mu_{ref}$  and  $T_{ref}$  refer to reference dynamic viscosity and temperature of flow respectively. Then,  $C_1$  is a constant which can be written as:

$$C_1 = \frac{\mu_{ref}}{T_{ref}^{3/2}} (T_{ref} + S) \quad (19)$$

Implicit formulation is used during the analyses, and at the beginning of the solution first order solutions are performed. At progressive stages of solution, second order solutions are used. Courant Number is increased by starting from 1 when residuals converge certain values or become horizontal. Courant-Friedrichs-Lewy (CFL) number is a condition while solving some hyperbolic partial differential equations with finite difference method. In density-based implicit formulation, the default CFL is 5 in Fluent®. It is probable to increase it depending upon the complication of problem [40]. For both models, solutions are converged between 2500 and 3000 iterations.

#### 4.5 Results

In this part of study, the main purpose is to obtain pressure distribution on the control surfaces. By this way, it will be used in structural part of the study to composite modeling. During the CFD analyses, 24 different analyses are carried out including mesh refinement study of two different models. These models are analyzed at supersonic velocity which is 1.6 Mach and 6 different angles of attack including 0°, 3°, 6°, 9°, 12°, and 15°. Missile surfaces modeled as wall boundary conditions. However, each part of body are named by separately in order to get compare the results of each cases. These parts are shown in Figure 21.

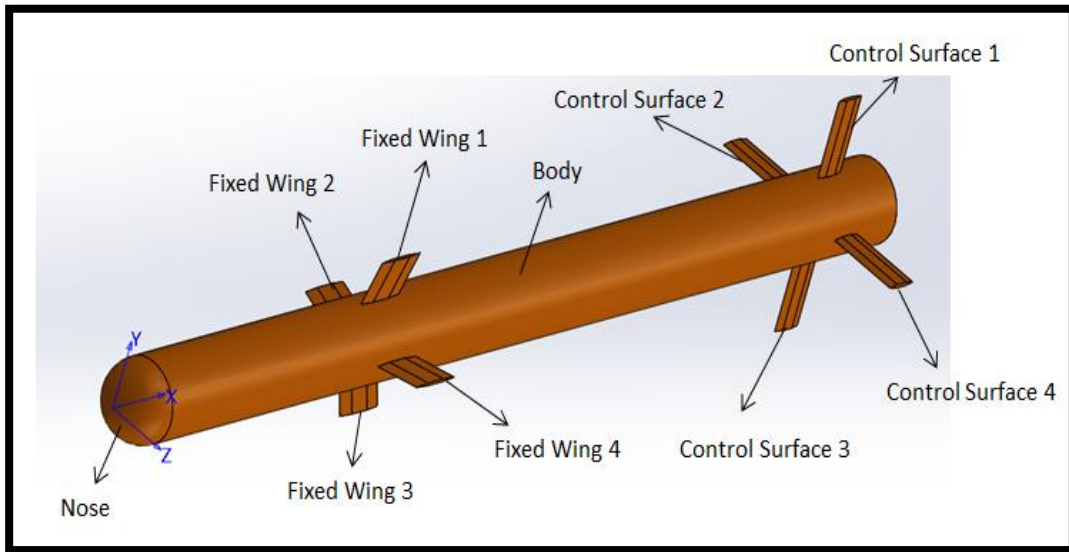


Figure 21 Missile part notations

The main purpose of CFD part is to get worst cases of aerodynamic loading which give maximum lift and drag forces on control surfaces. These cases are the cases of  $15^\circ$  of angle of attack for both model-1 and model-2. Lift and drag coefficients for each part is obtained. They are obtained for both fine and coarse meshes are shown in Figures 21-26. According to these Figures, there are some key points in order to say that solution is converged. First of all, in the cases of fine and coarse meshes, lift and drag coefficients are very close to each other for each part. Secondly, for model-1 and model-2 case, nose, body and fixed wing geometries are unique and it is expected that their lift and drag coefficients should be close to each other at a certain angle of attack. In other words, flow characteristics are the same until flow reaches the control surfaces having different cross-sections for model-1 and model-2 so, in both missile models, lift and drag coefficients of nose and fixed wings should be close to each other. This may be evaluated as another convergence criterion.

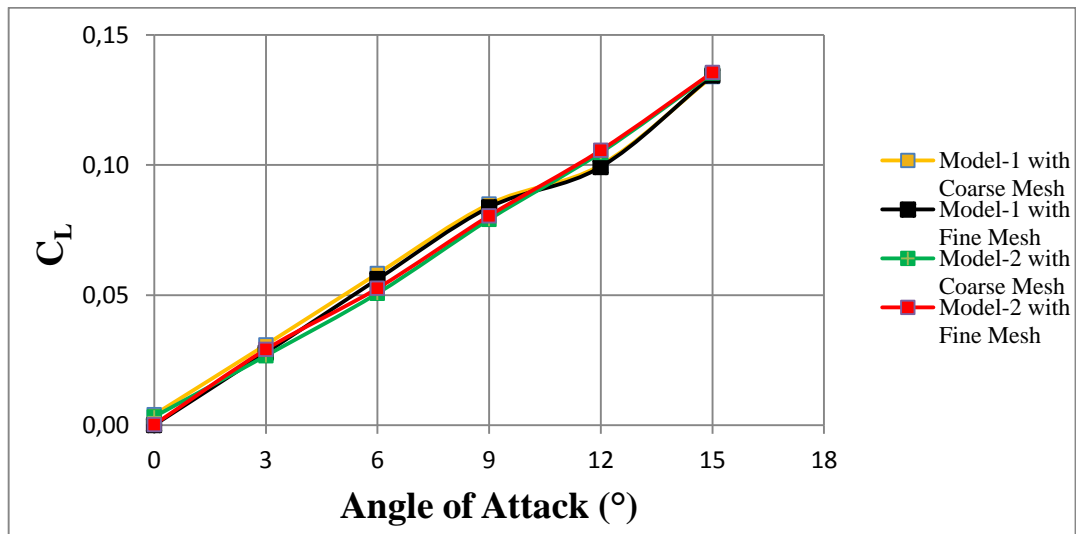


Figure 22  $C_L$  vs.  $\alpha$  ( $^\circ$ ) graph of nose

As it is seen in Figure 22, lift coefficients of nose are obtained for both model-1 and model-2 with the mesh refinement study. It is obvious that, coarse and fine mesh results are very close to each other for both missile models. The maximum percentage difference between coarse and fine mesh of model-1 is 3.8% approximately which occurs at  $6^\circ$  angle of attack analyses. This value is 3.7% for model-2 mesh refinement study. On the other hand, the maximum percentage difference between the cases of fine meshes of model-1 and model-2 is 4.3% occurring at  $12^\circ$  angle of attack analyses. The maximum lift coefficient values are 0.14 for noses of missile model-1 and missile model-2.

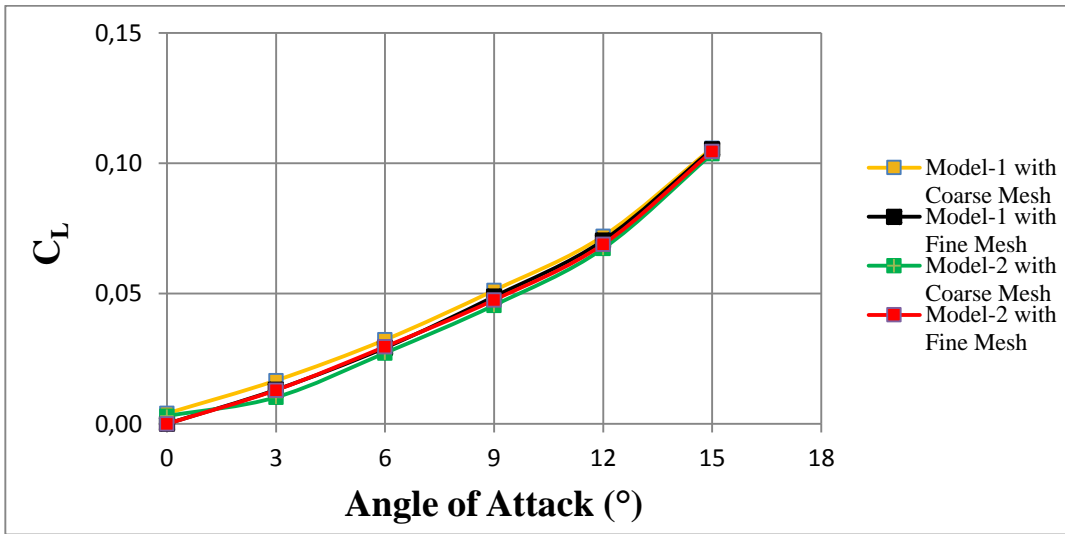


Figure 23  $C_L$  vs.  $\alpha$  (°) graph of body

In Figure 23, lift coefficients of missile bodies are shown. It can be seen that, results of each cases are very close to each other. For missile body, the maximum percentage difference between coarse and fine mesh of model-1 is 4.8% approximately which occurs at 9° angle of attack analyses. This value is 5.3% for model-2 mesh refinement study. On the other hand, the maximum percentage difference between the cases of fine meshes of model-1 and model-2 is 2.7% occurring at 6° angle of attack analyses. The maximum lift coefficient values are 0.11 for bodies of missile model-1 and missile model-2.

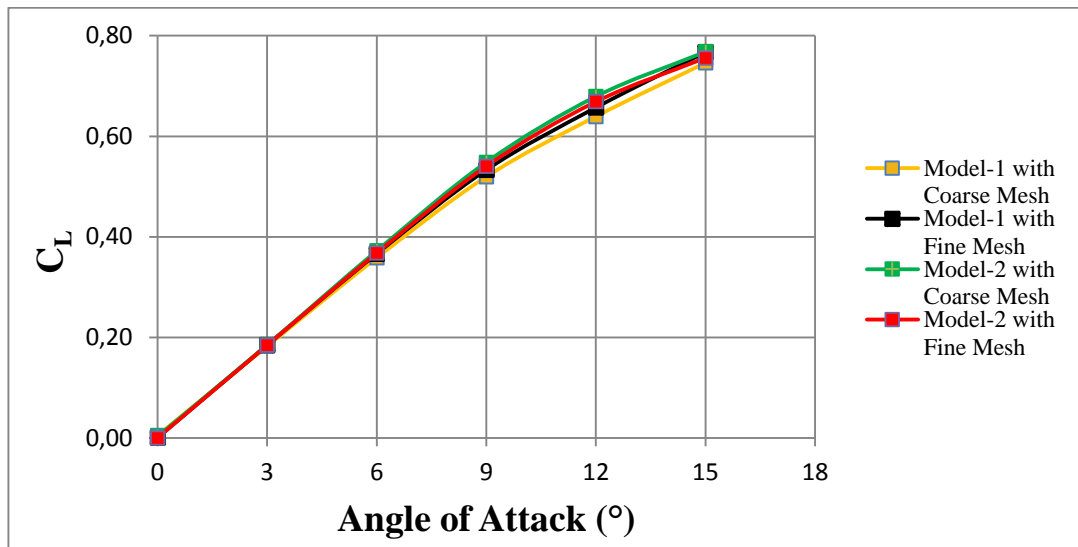


Figure 24  $C_L$  vs.  $\alpha$  (°) graph of fixed wing-4

In Figure 24, lift coefficients of fixed wings-4 are shown. For fixed wing, the maximum percentage difference between coarse and fine mesh of model-1 is 3.1% approximately which occurs at 12° angle of attack analyses. This value is 2.0% for model-2 mesh refinement study. On the other hand, the maximum percentage difference between the cases of fine meshes of model-1 and model-2 is 3.7% occurring at 12° angle of attack analyses. The maximum lift coefficient values are 0.76 for fixed wings of missile model-1 and missile model-2.

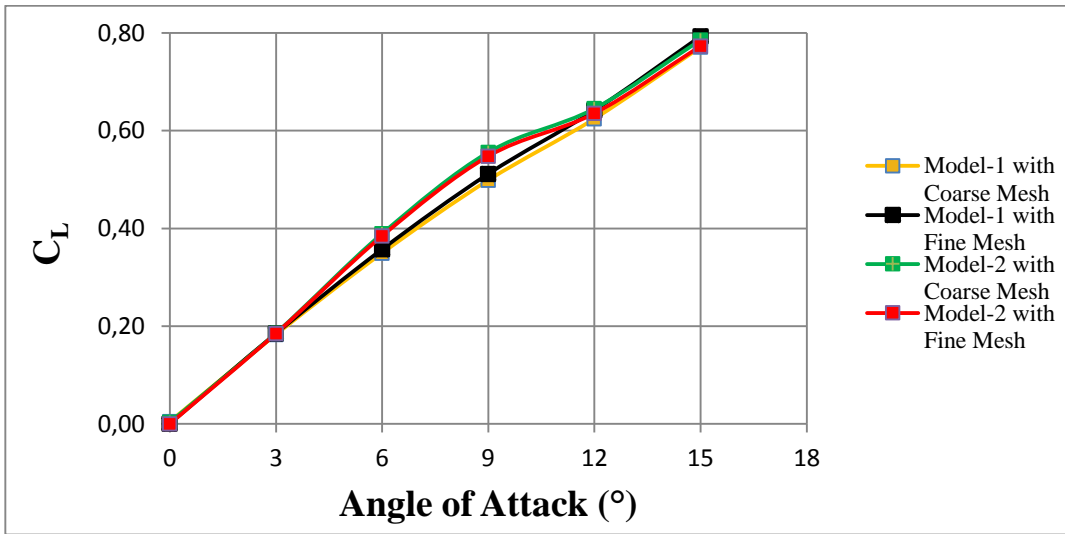


Figure 25  $C_L$  vs.  $\alpha$  (°) graph of control surface-4

In Figure 25, lift coefficients of control surfaces-4 with respect to angle of attack are shown. For control surface, the maximum percentage difference between coarse and fine mesh of model-1 is 2.0% approximately which occurs at 9° angles of attack analyses. This value is 2.4% for model-2 mesh refinement study at 12° angles of attack analyses. The maximum lift coefficient value of model-1 is 0.79 while the maximum lift coefficient of model-2 is 0.77.

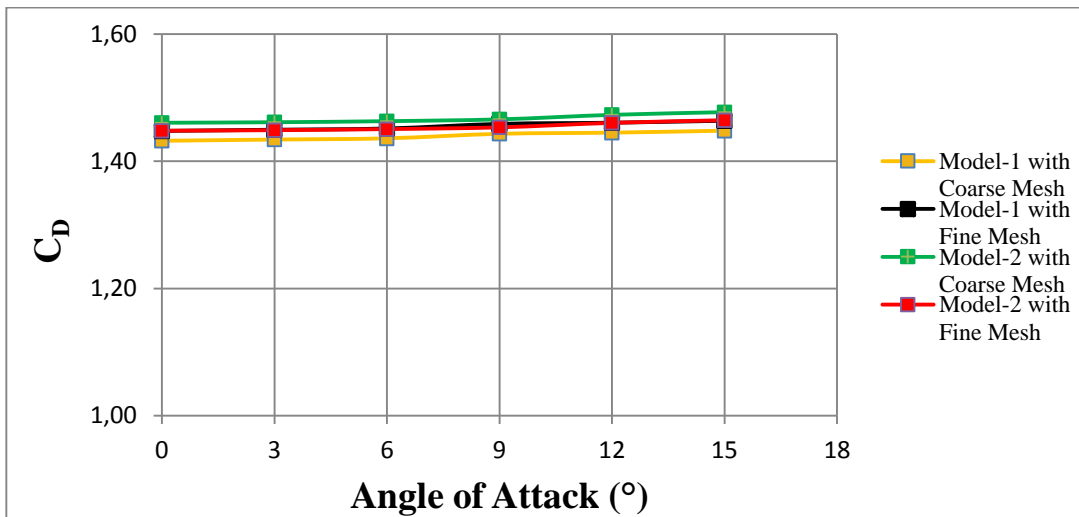


Figure 26  $C_D$  vs.  $\alpha$  (°) graph of nose

In Figure 26, drag coefficients of missile noses are shown. The maximum percentage difference between coarse and fine mesh of model-1 is 5.1% approximately which occurs at 6° angle of attack analyses. This value is 3.9% for model-2 mesh refinement study. On the other hand, the maximum percentage difference between the cases of fine meshes of model-1 and model-2 is 1.7% occurring at 6° angle of attack analyses. The maximum drag coefficient values are 1.46 for noses of missile model-1 and missile model-2.

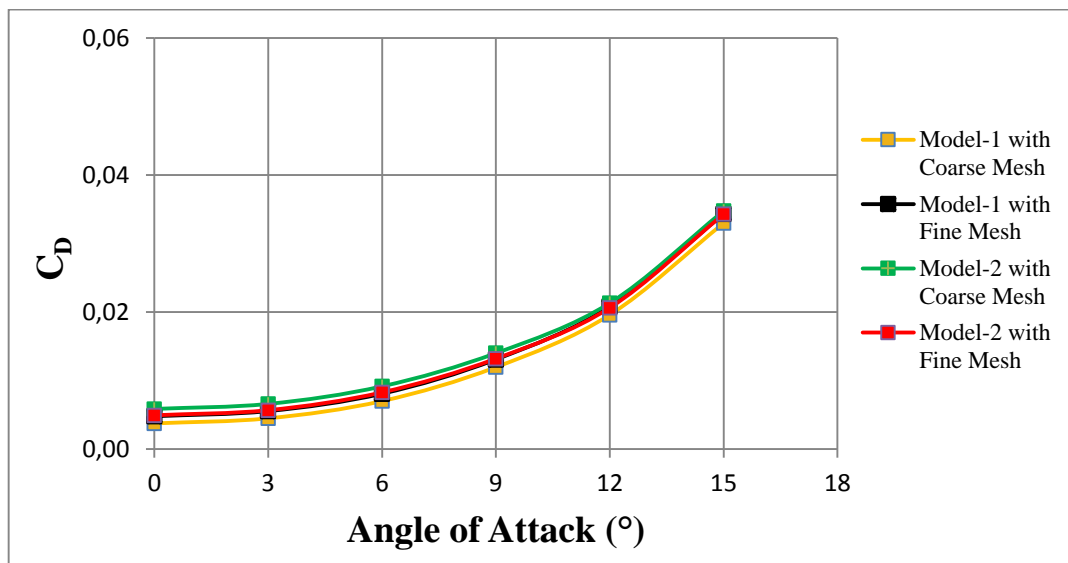


Figure 27  $C_D$  vs.  $\alpha$  (°) graph of body

In Figure 27, drag coefficients of missile bodies are shown. It can be seen that, results of each cases are very close to each other. For missile body, the maximum percentage difference between coarse and fine mesh of model-1 is 2.8% approximately which occurs at 3° angle of attack analyses. This value is 3.4% for model-2 mesh refinement study. On the other hand, the maximum percentage difference between the cases of fine meshes of model-1 and model-2 is 2.8% occurring at 6° angle of attack analyses. The maximum drag coefficients values are 0.03 for bodies of missile model-1 and missile model-2.

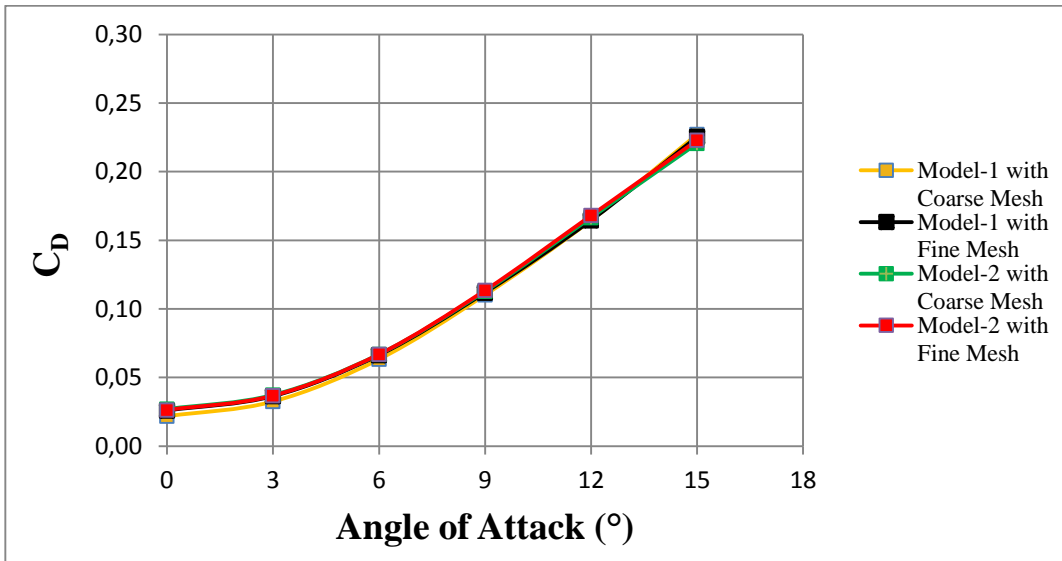


Figure 28  $C_D$  vs.  $\alpha$  (°) graph of fixed wing-4

In Figure 28, drag coefficients of fixed wings-4 are shown. For fixed wing, the maximum percentage difference between coarse and fine mesh of model-1 is 2.1% approximately which occurs at 3° angle of attack analyses. This value is 2.0% for model-2 mesh refinement study. On the other hand, the maximum percentage difference between the cases of fine meshes of model-1 and model-2 is 2.7% occurring at 3° angle of attack analyses. The maximum drag coefficient values are 0.22 for fixed wings of missile model-1 and missile model-2.

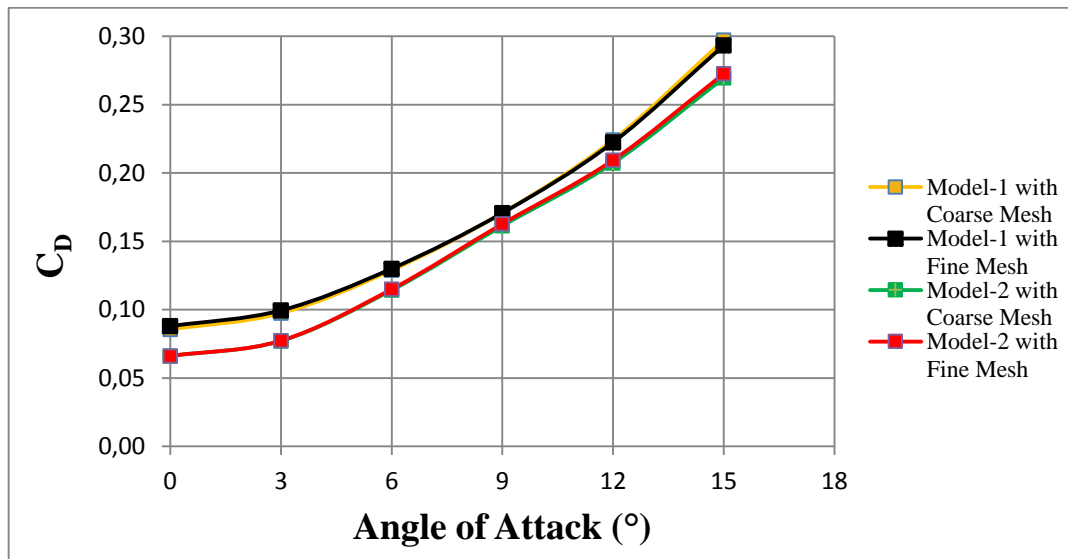


Figure 29  $C_D$  vs.  $\alpha$  (°) graph of control surface-4

In Figure 29, drag coefficients of control surfaces-4 with respect to angle of attack are shown. For control surface, the maximum percentage difference between coarse and fine mesh of model-1 is 1.6% approximately which occurs at 15° angles of attack analyses. This value is 1.8% for model-2 mesh refinement study at 15° angles of attack analyses. The maximum drag coefficient value of model-1 is 0.29 while maximum drag coefficient of model-2 is 0.27.

Lift and drag coefficient variations are obtained for fine and coarse grid for both missile models in order to compare and discuss the results of mesh refinement study. Free-stream is the same for both missile models until it reaches the control surfaces with different cross-sections. As a result of this, CFD models of noses and fixed wings of both missile models have nearly same lift and drag coefficients at all angles of attack as expected. Moreover, as it is seen in fine and coarse mesh results of lift and drag variation figures of nose and fixed wings, drag and lift coefficients are very close to each other in each angle of attack analysis so CFD solutions can be considered as converged. Then, normal force and axial force variations with angle of attack is obtained during the study.

Since mesh refinement study is performed for only lift and drag coefficients, normal force, axial force and center of pressure variations are considered by using only fine grids of missile models.

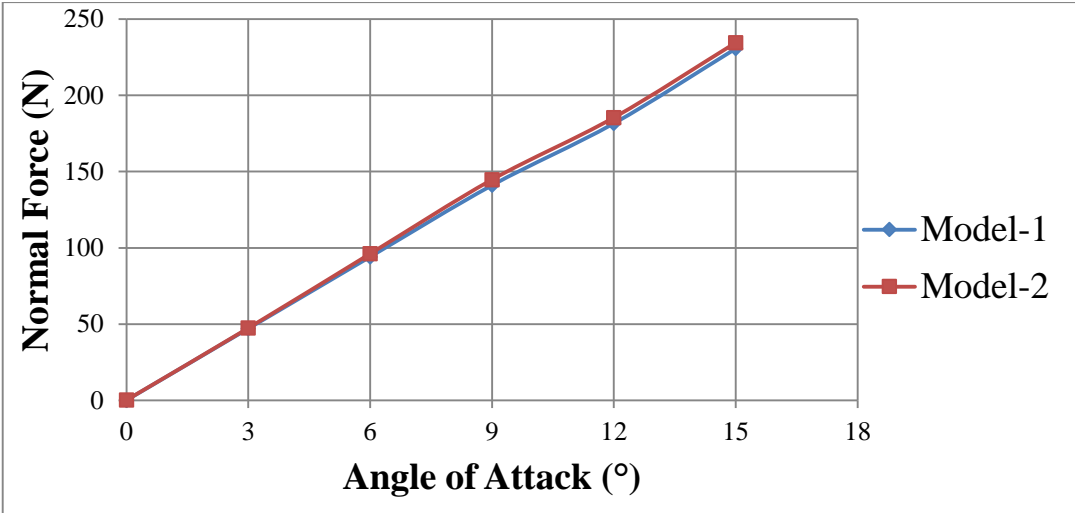


Figure 30 Normal Force (N) vs.  $\alpha$  (°) graph of nose

Normal force variations with angle of attack for nose parts of model-1 model-2 are given in Figure 30. According to the Figure, normal forces acting on the nose part increase with angle of attack as expected. It is seen that, force values are very close to each other due to the unique geometry of this part in both model. The maximum normal force occurs at 15° angle of attack for both cases. The maximum normal force value of model-1 is 230.7 N while this value is 234.6 N for model-2. Also, the maximum percent difference of normal forces between two models is %2.56 which is obtained by 9° angle of attack analyses.

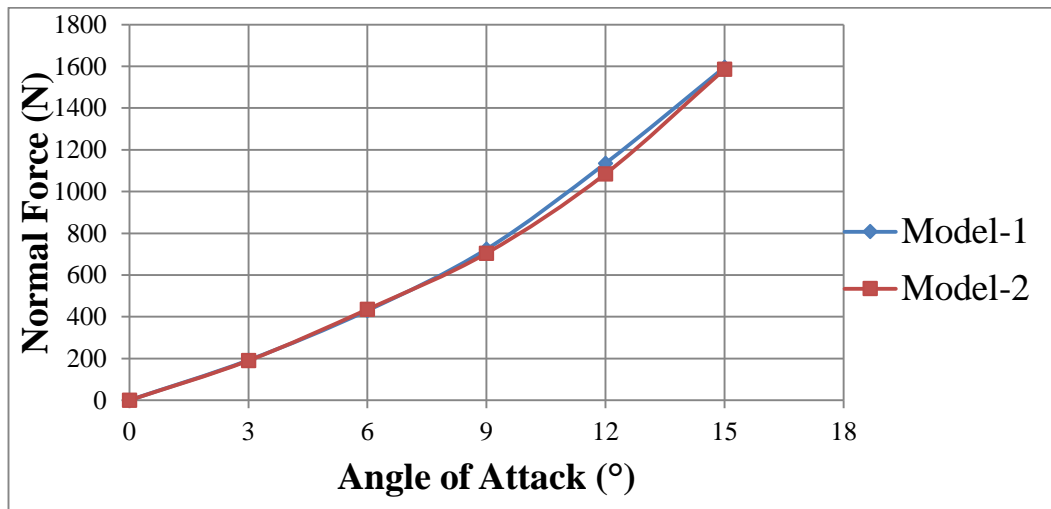


Figure 31 Normal Force (N) vs.  $\alpha$  ( $^{\circ}$ ) graph of body

In Figure 31, normal forces varying with the angles of attack are shown for body parts of model-1 and model-2. In this Figure, it is obvious that, normal forces acting on the body parts increase with angle of attack as expected for both cases. Due to the same geometric dimensions of body parts of model-1 model-2, values of normal force are close to each other. The maximum normal force value is obtained from  $15^{\circ}$  angle of attack analyses for each model. This is 1595.6 N for model-1 and 1585.6 N for model-2. Moreover, the maximum percent difference of normal forces between two models is %5.26 which is obtained by  $12^{\circ}$  angle of attack analyses.

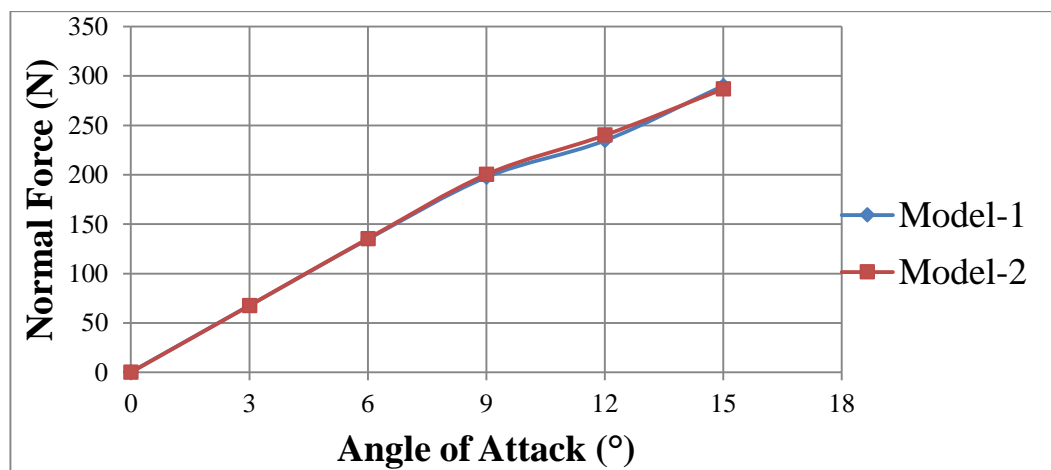


Figure 32 Normal Force (N) vs.  $\alpha$  ( $^{\circ}$ ) graph of fixed wing-4

Normal force variations with angle of attack for fixed wings of model-1 and model-2 are given in Figure 32. According to the Figure, normal forces acting on the wings increase with angle of attack as expected. It is seen that, force values are very close to each other due to the unique geometry of fixed wings in both model. The maximum normal force occurs at 15° angle of attack for both cases. The maximum normal force value of model-1 is 290.4 N while this value is 286.79 N for model-2. Also, the maximum percent difference of normal forces between two models is %2.26 which is obtained by 12° angle of attack analyses.

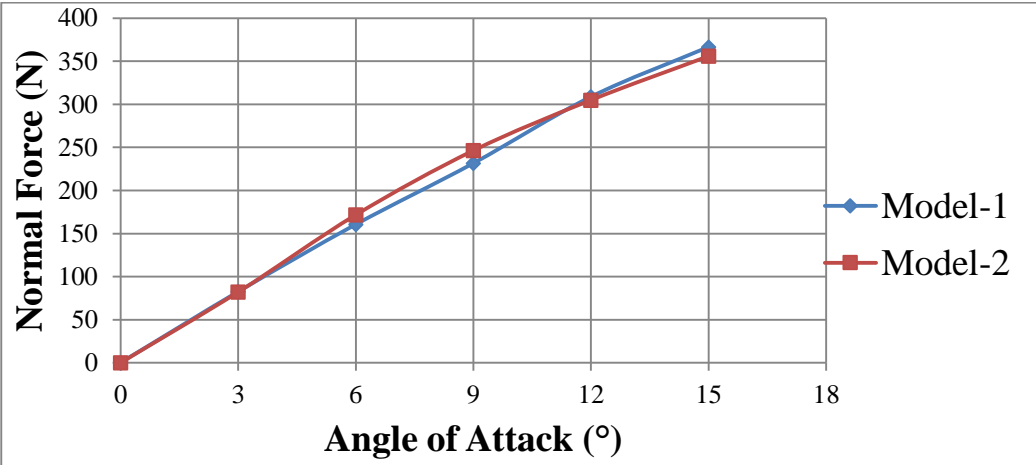


Figure 33 Normal Force (N) vs.  $\alpha$  (°) graph of control surface 4

Variation in normal forces of control surfaces of model-1 and model-2 with angle of attack is given in Figure 33. According to the Figure, normal forces acting on the wings increase with angle of attack as expected. The maximum normal force occurs at 15° angle of attack for both cases. The maximum normal force value of model-1 is 366.34 N while this value is 356.17 N for model-2.

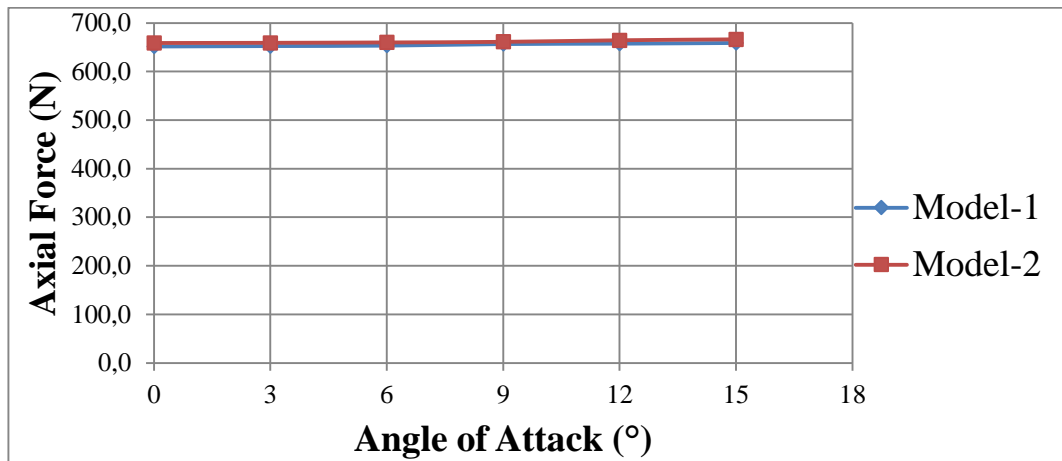


Figure 34 Axial Force (N) vs.  $\alpha$  (°) graph of nose

Axial force variations with angle of attack for nose parts of model-1 and model-2 are given in Figure 34. According to the Figure, axial forces acting on the nose part increase with angle of attack as expected. It is seen that, force values are very close to each other due to the unique geometry of this part in both model. The maximum axial force occurs at 15° angle of attack for both cases. The maximum axial force value of model-1 is 658.9 N while this value is 665.4 N for model-2. Also, the maximum percent difference of axial forces between two models is %1.6 which is obtained by 6° angle of attack analyses.

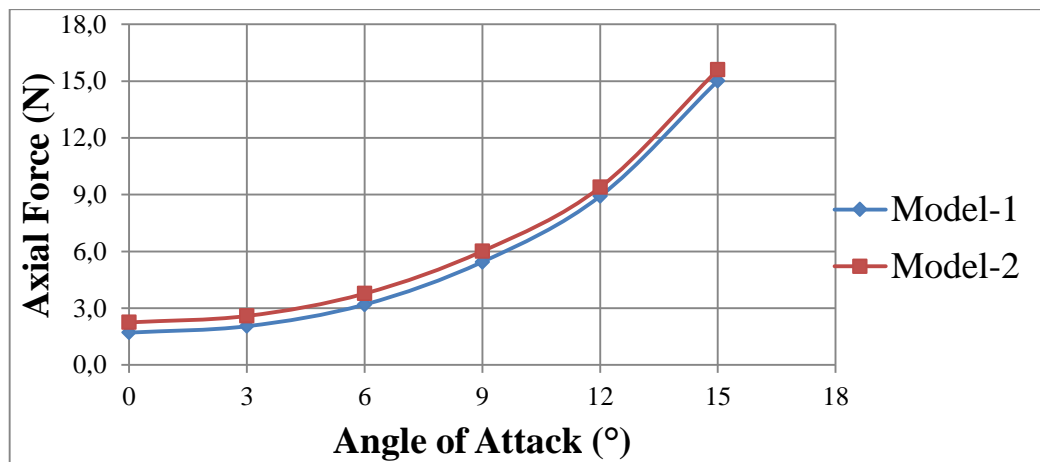


Figure 35 Axial Force (N) vs.  $\alpha$  (°) graph of body

Variation in axial forces of body of model-1 model-2 with angle of attack is given in Figure 35. According to the Figure, axial forces acting on the missile body increase with angle of attack as expected. The maximum axial force occurs at 15° angle of attack for both cases. The maximum axial force value of model-1 is 15.0 N while this value is 15.2 N for model-2. Also, the maximum percent difference of axial forces between two models is %4.8 which is obtained by 6° angle of attack analyses.

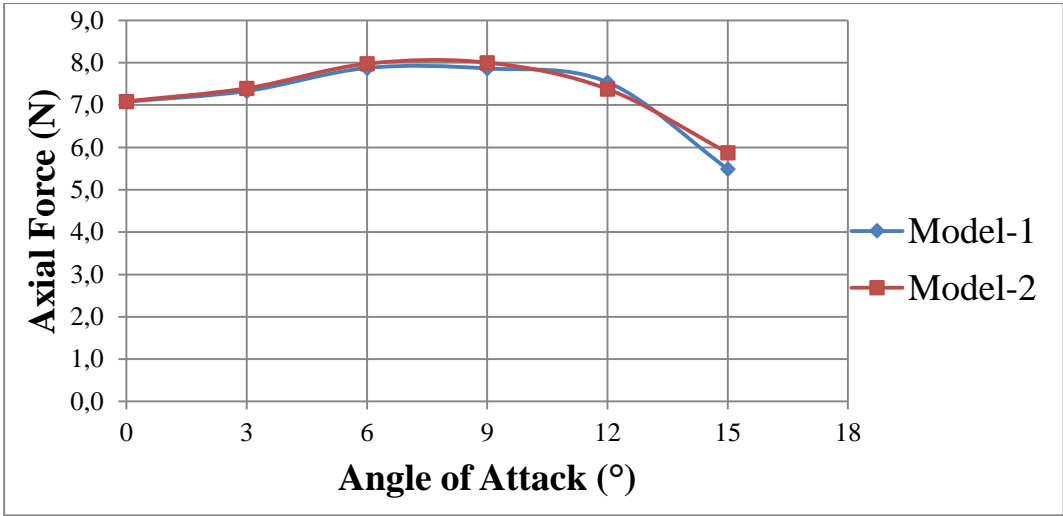


Figure 36 Axial Force (N) vs.  $\alpha$  (°) graph of fixed wing-4

Axial force variations with angle of attack for fixed wings of model-1 model-2 are given in Figure 36. It is seen that, force values are very close to each other due to the unique geometry of fixed wings in both model. The maximum axial force occurs at 6° angle of attack for both cases. The maximum axial force value of model-1 is 7.98 N while this value is 8.01 N for model-2. Also, the maximum percent difference of axial forces between two models is %4.86 which is obtained by 15° angle of attack analyses.

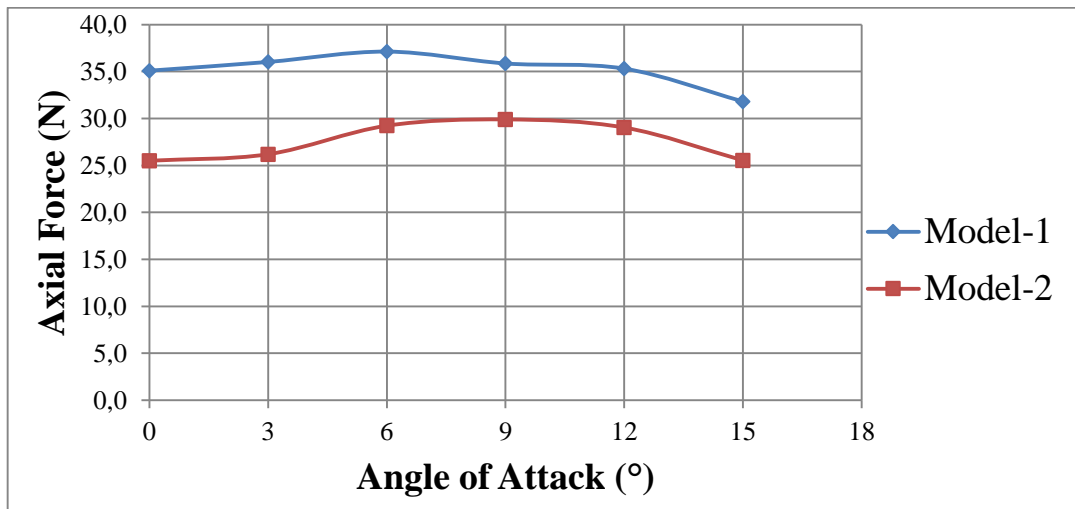


Figure 37 Axial Force (N) vs.  $\alpha$  ( $^{\circ}$ ) graph of control surface 4

Variation in axial forces of control surfaces of model-1 model-2 with angle of attack is given in Figure 37. The maximum axial force occurs at  $6^{\circ}$  angle of attack for model-1 and  $9^{\circ}$  angle of attack for model-2. These values are very close to each other as it is seen. The maximum axial force value of model-1 is 37.13 N while this value is 29.90 N for model-2.

Maximum normal force acting on missile model-1 is approximately 3139.4 N. Normal force acting on control surface-4 of model-1 is 11.68% of maximum normal force acting on missile model-1. Also, maximum normal force acting on missile model-2 is approximately 3106.1 N. Normal force acting on control surface-4 of model-2 is 11.45% of normal force acting on missile model-2.

Maximum axial force acting on missile model-1 is approximately 833.5 N. Axial force acting on control surface-4 of model-1 is 4.45% of maximum axial force acting on missile model-1. Also, maximum axial force acting on missile model-2 is approximately 808.7 N. Axial force acting on control surface-4 of model-2 is 3.68% of maximum axial force acting on missile model-2.

The main goal of CFD part of this study is to obtain maximum resultant force acting on control surface-4 due to pressure distribution. In order to perform structural analyses, pressure center location of the flight condition at which the control surfaces are subjected to maximum aerodynamic loads is also needed. This condition occurs at 15° angle of attack for both missile models.

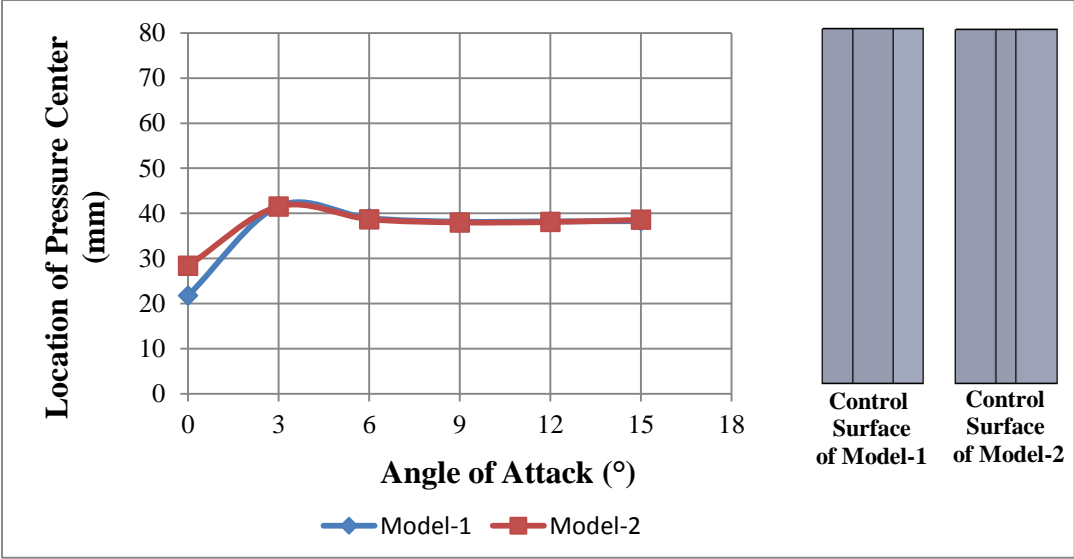


Figure 38 Spanwise variation of C.P. location via  $\alpha$  (°)

In Figure 38, pressure center variations of control surfaces with angle of attack through the span are shown. For control surface of model-1 the pressure center is 38.26 mm away from root of control surface at 15° angle of attack. This distance is 38.57 mm for control surface of model-2.

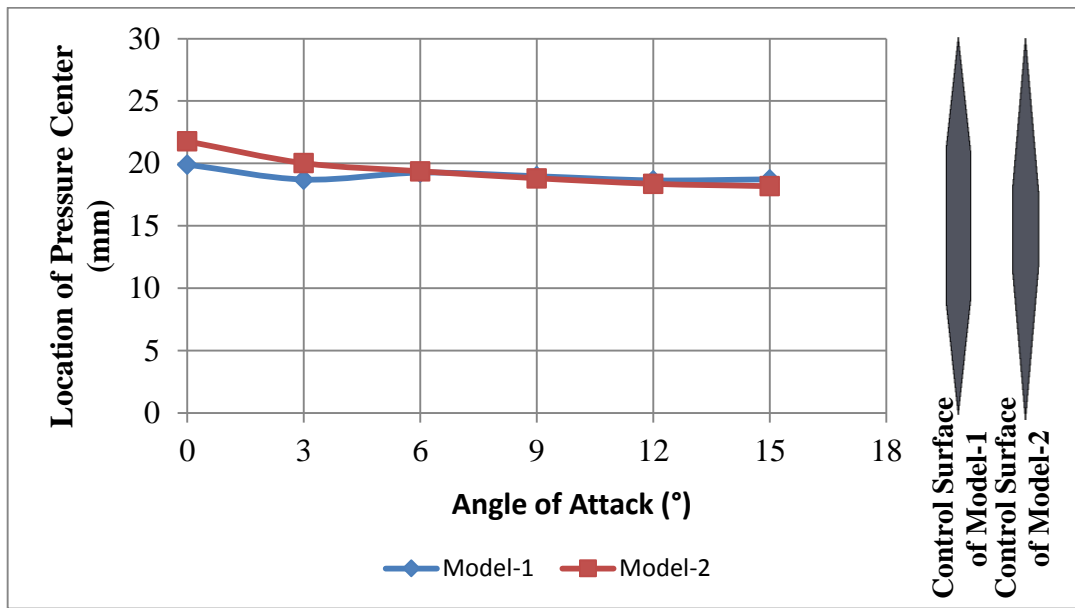


Figure 39 Variation of C.P. location through the chord length via  $\alpha$  ( $^{\circ}$ )

In Figure 39, pressure center variations of control surfaces with angle of attack through the chord are shown. For control surface of model-1 the pressure center is 11.83 mm away from leading edge at  $15^{\circ}$  angle of attack. This distance is 11.27 mm for control surface of model-2.

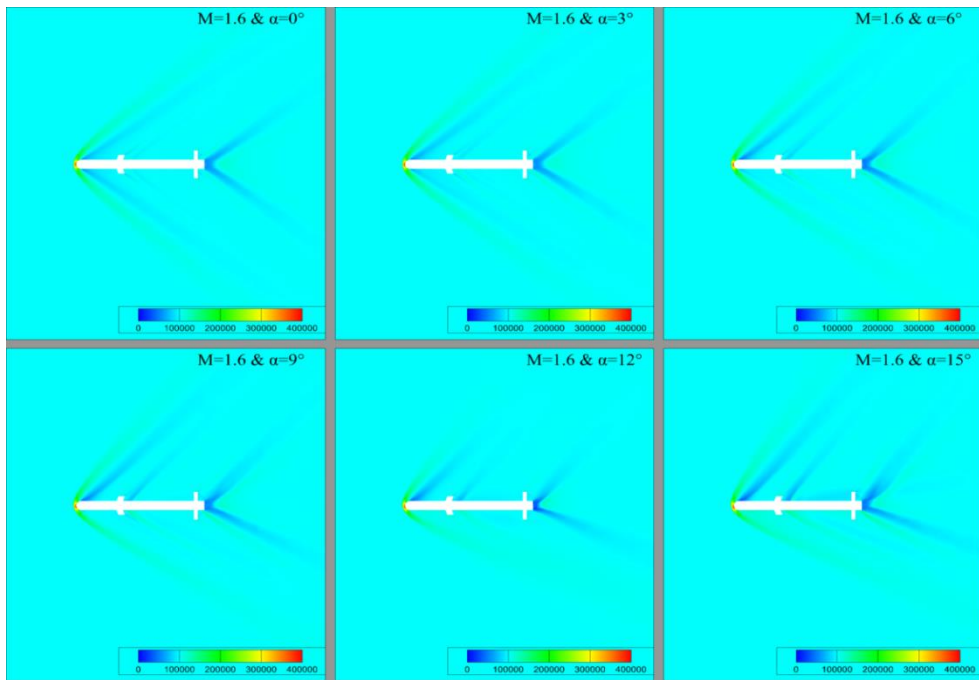


Figure 40 Static pressure (MPa) distribution of model-1 at different  $\alpha$  ( $^\circ$ )

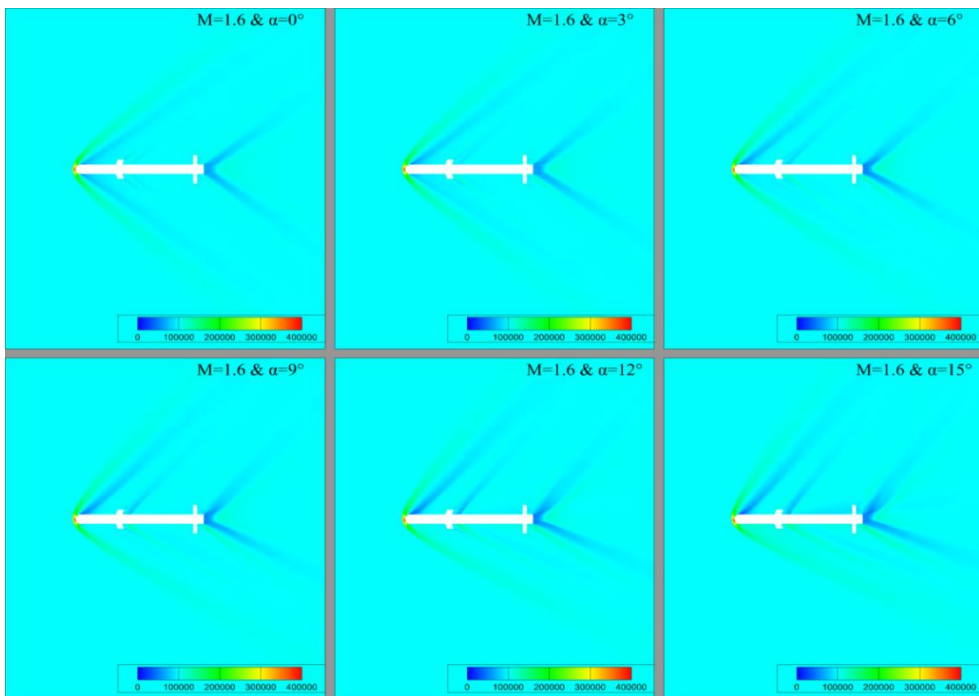


Figure 41 Static pressure (MPa) distribution of model-2 at different  $\alpha$  ( $^\circ$ )

In Figure 41 and 42, static pressure distributions at different angles of attack for model-1 model-2 are shown. At the mid-plane of missiles, pressure distributions are obtained at  $0^\circ$ ,  $3^\circ$ ,  $6^\circ$ ,  $9^\circ$ ,  $12^\circ$  and  $15^\circ$  angles of attack respectively. According to these figures, maximum static pressure occurs at noses of model-1 and model-2 due to the curved bow shock waves. Also, the maximum static pressures of all flight conditions are very close to each other due to the shapes of noses. Since the noses have spherical shape, free-stream lines are always parallel to the surface normal of it regardless of angle of attack. Thus, the maximum static pressure acting on nose surfaces are 382 kPa approximately for all cases.

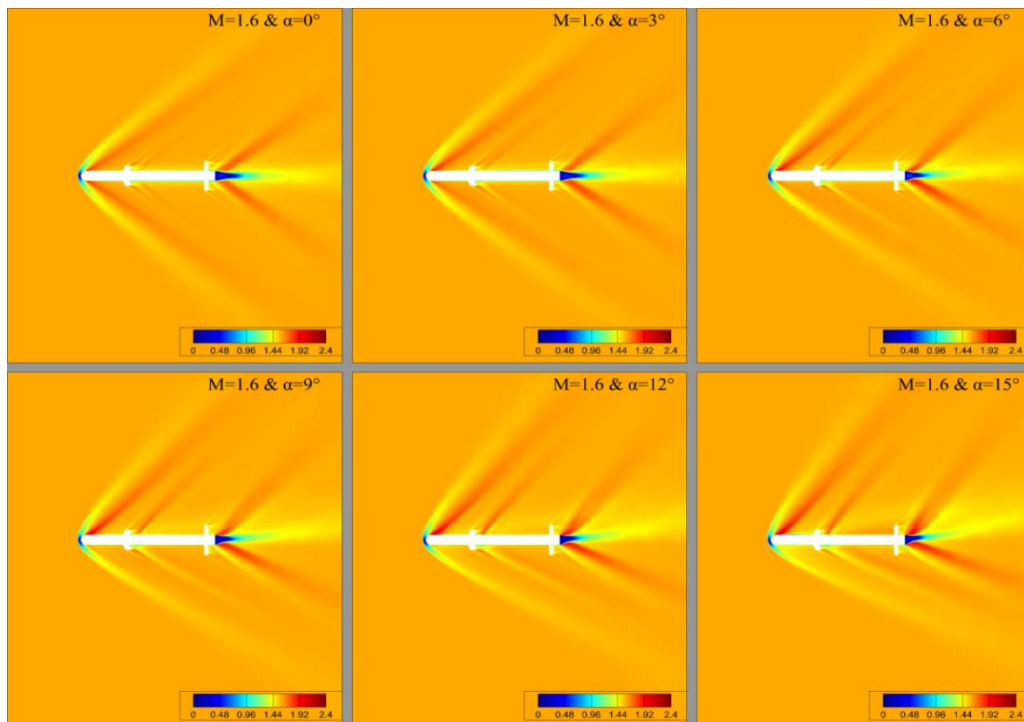


Figure 42 Mach number distribution of model-1 at different  $\alpha$  ( $^\circ$ )

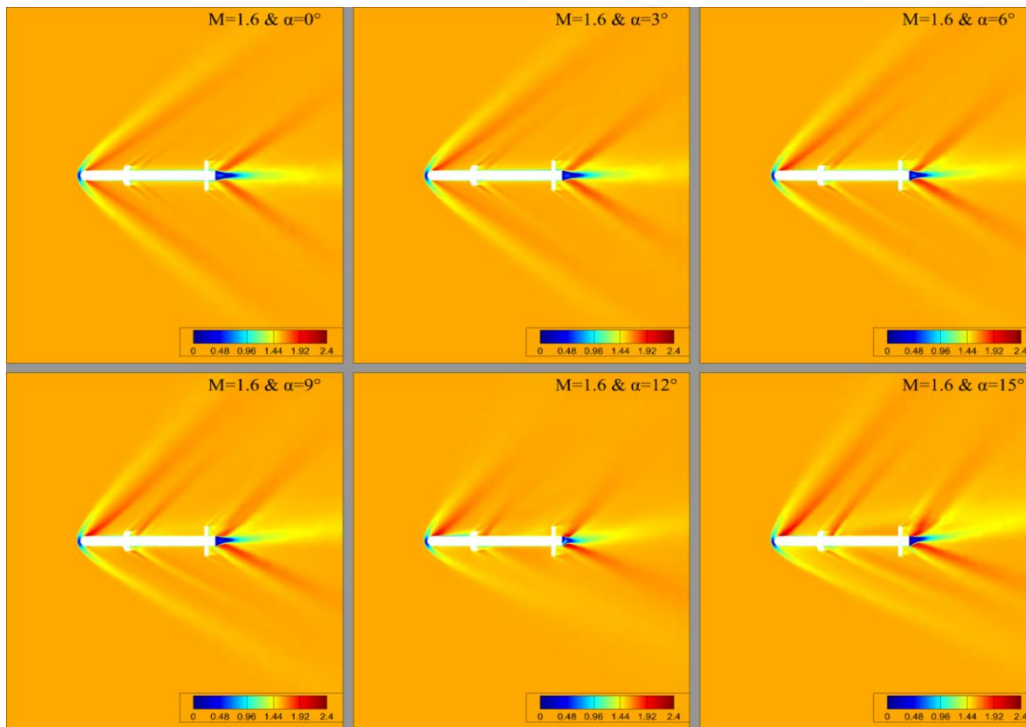


Figure 43 Mach number distribution of model-2 at different  $\alpha$  ( $^{\circ}$ )

In Figure 42 and 43, Mach number distributions at different angles of attack for model-1 and model-2 are given. At the mid-plane of missile, Mach numbers are obtained at  $0^{\circ}$ ,  $3^{\circ}$ ,  $6^{\circ}$ ,  $9^{\circ}$ ,  $12^{\circ}$  and  $15^{\circ}$  angles of attack respectively. The maximum Mach number occurs at  $15^{\circ}$  angle of attack case, and it is 2.27 Mach. Expansion waves acting on the top of noses of both missile models cause an increase in Mach number for  $15^{\circ}$  angle of attack flight condition, and the maximum Mach numbers are seen in these regions for both missile model-1 and model-2.

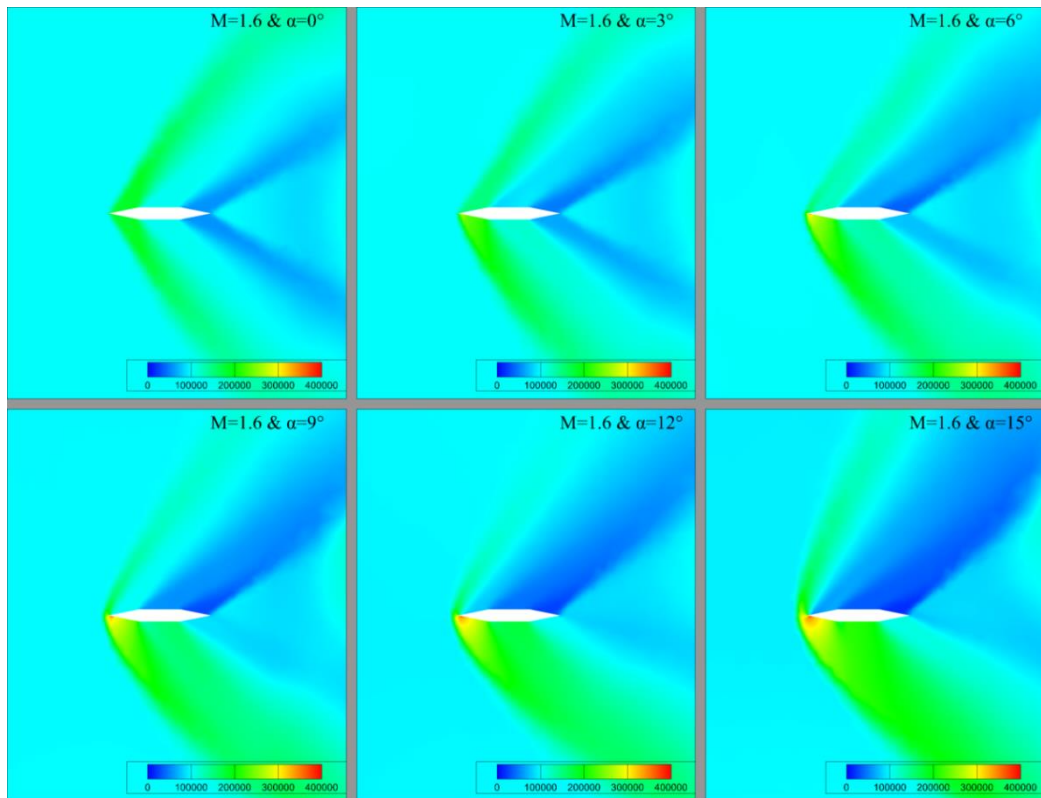


Figure 44 Static pressure (MPa) distribution of control surface-4 of model-1 at different  $\alpha$  ( $^{\circ}$ )

In Figure 44, static pressure distributions at different angles of attack for control surface-4 of model-1 are given. At the mid-plane of control surface, pressure distributions are obtained at  $0^{\circ}$ ,  $3^{\circ}$ ,  $6^{\circ}$ ,  $9^{\circ}$ ,  $12^{\circ}$  and  $15^{\circ}$  angles of attack respectively. The maximum pressure occurs at  $15^{\circ}$  angle of attack case, and it is 375000 Pa. For model-1, control surface wedge angle is approximately  $11.31^{\circ}$ . There are two symmetric oblique shock waves at the top and bottom of front wedge when angle of attack is  $0^{\circ}$ . However, when the angle of attack is increased to  $3^{\circ}$ , detached shock is observed at the bottom surface of the front wedge. This is also seen in  $6^{\circ}$ ,  $9^{\circ}$ ,  $12^{\circ}$  and  $15^{\circ}$  angle of attack Figures. Moreover, these surfaces are the regions at which maximum pressure is observed for these angles of attacks.

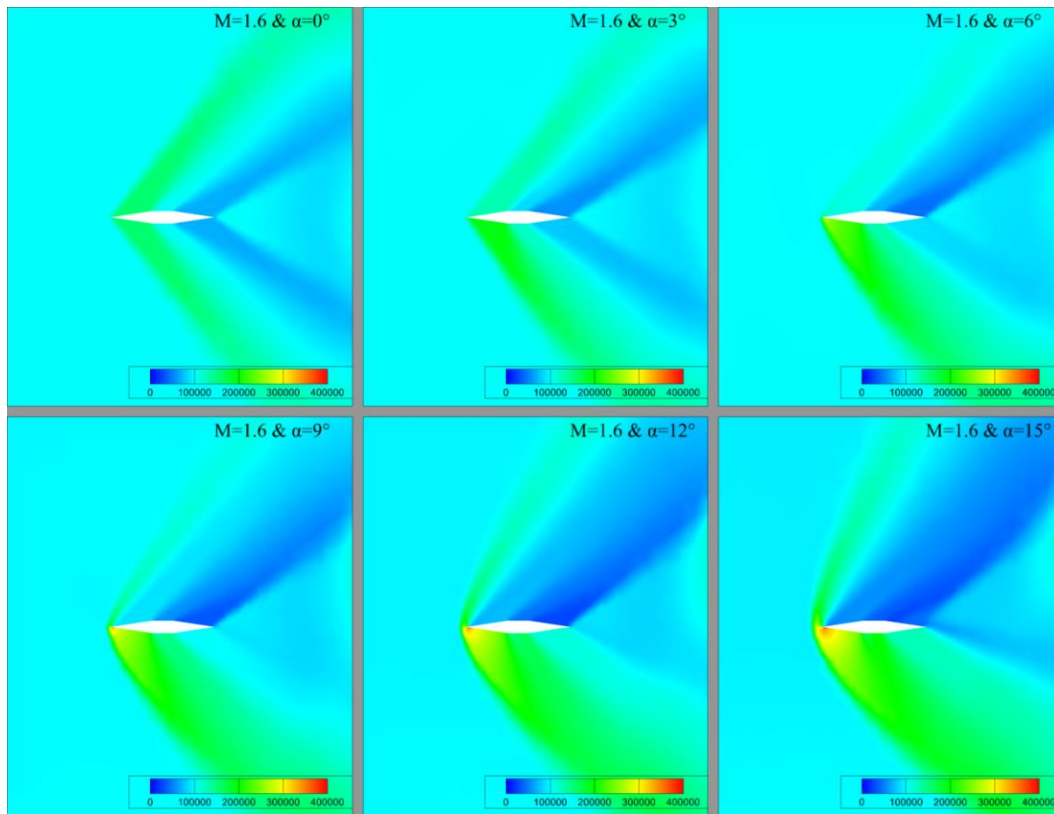


Figure 45 Static pressure (MPa) distribution of control surface-4 of model-2 at different  $\alpha$  ( $^{\circ}$ )

In Figure 45, static pressure distributions at different angles of attack for control surface-4 of model-2 are given. At the mid-plane of control surface, pressure distributions are obtained at  $0^{\circ}$ ,  $3^{\circ}$ ,  $6^{\circ}$ ,  $9^{\circ}$ ,  $12^{\circ}$  and  $15^{\circ}$  angles of attack respectively. The maximum pressure occurs at  $15^{\circ}$  angle of attack case, and it is 371000 Pa. For model-1, control surface wedge angle is approximately  $8.53^{\circ}$ . There are two symmetric oblique shock waves at the top and bottom surfaces of front wedge when angle of attack is  $0^{\circ}$ . At  $3^{\circ}$  angle of attack, two oblique shock waves are observed but shock waves are stronger at the bottom surfaces of front wedges. However, when the angle of attack is increased to  $6^{\circ}$ , detached shock occurs at the bottom surface of the front wedge. This is also seen from  $6^{\circ}$ ,  $9^{\circ}$ ,  $12^{\circ}$  and  $15^{\circ}$  angle of attack Mach number contours in Figure 46. Moreover, these regions are the regions at which maximum pressure is observed for these angles of attacks.

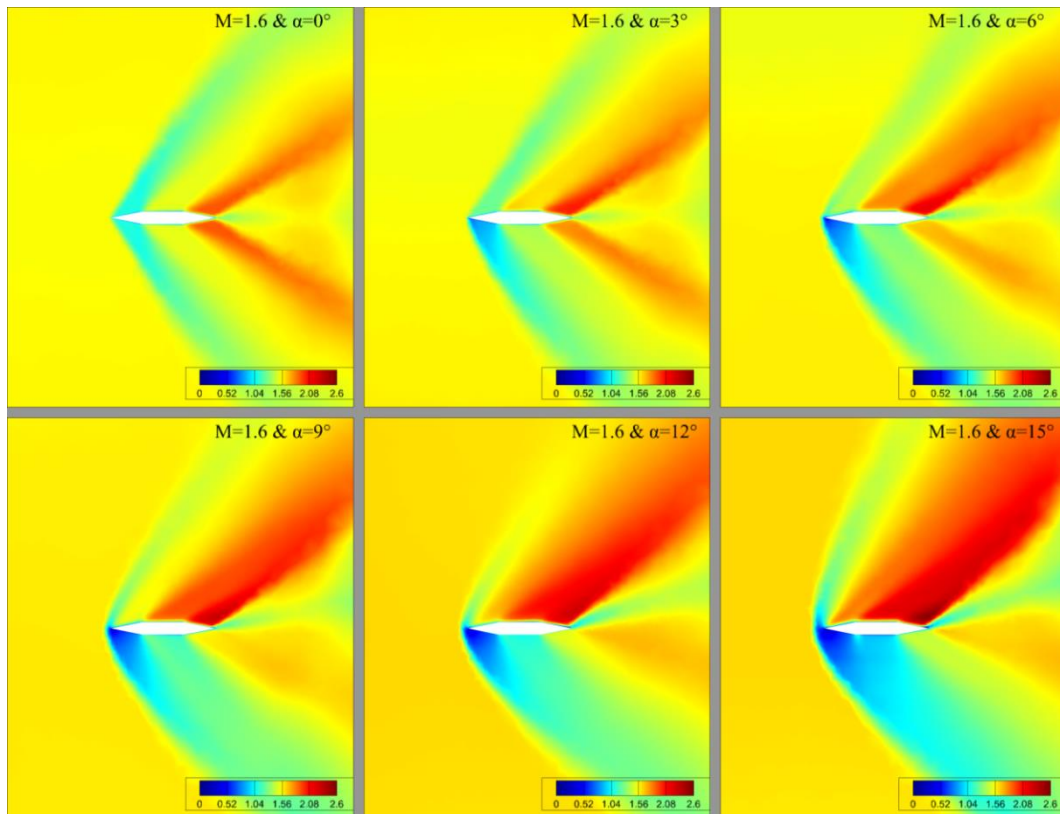


Figure 46 Mach number distribution of control surface-4 of model-1 at different  $\alpha$

In Figure 46, Mach number distributions at different angles of attack for control surface-4 of model-1 are given. At the mid-plane of control surface, Mach numbers are obtained at  $0^\circ$ ,  $3^\circ$ ,  $6^\circ$ ,  $9^\circ$ ,  $12^\circ$  and  $15^\circ$  angles of attack respectively. The maximum Mach number occurs at  $15^\circ$  angle of attack case, and it is 2.58 Mach. An expansion wave acting on the top surface of back wedge causes increase in Mach number for  $15^\circ$  angle of attack flight condition, and the maximum Mach number is seen in this region. Detached shock waves are seen at the bottom surface of front wedge in the Figure except  $0^\circ$  angle of attack case. In the Figure of  $0^\circ$  angle of attack, two symmetric oblique shock waves are obtained on the front wedge surfaces. These can be also seen in static pressure figure which is Figure 44.

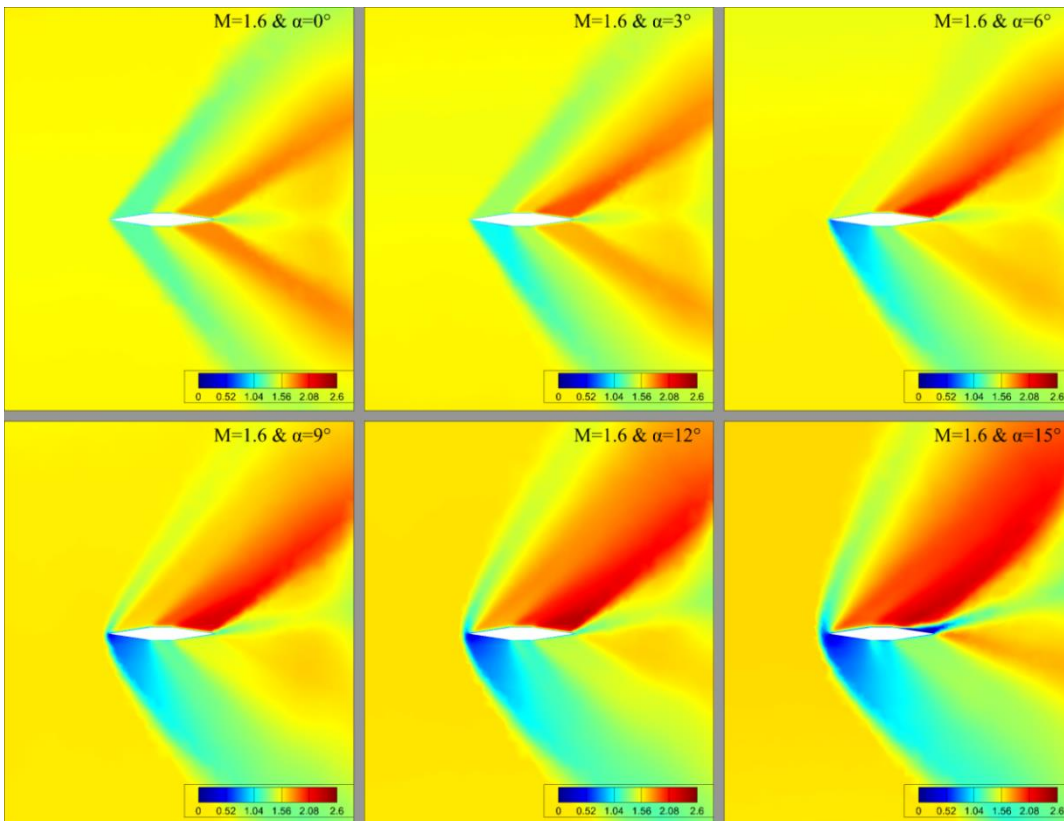


Figure 47 Mach number distribution of control surface-4 of model-2 at different  $\alpha$

In Figure 47, distributions of Mach number at different angles of attack for control surface-4 of model-2 are given. At the mid-plane of control surface, Mach numbers are obtained at  $0^\circ$ ,  $3^\circ$ ,  $6^\circ$ ,  $9^\circ$ ,  $12^\circ$  and  $15^\circ$  angles of attack respectively. The maximum Mach number occurs at  $15^\circ$  angle of attack case, and it is 2.35 Mach. An expansion wave acting on the top surface of back wedge causes increase in Mach number for  $15^\circ$  angle of attack flight condition, and the maximum Mach number is seen in this region. Detached shock waves are seen at the bottom surface of front wedge in the Figure except the Figures of  $0^\circ$  and  $3^\circ$  angles of attack. In the Figure of  $0^\circ$  angle of attack, two symmetric oblique shock waves are obtained on the front wedge surfaces. Moreover, there are two oblique shock waves occurring at front wedge surfaces in the Figure of  $3^\circ$  angle of attack but the shock wave acting on the bottom surface is stronger than wave at top surface. These can be also seen in static pressure figure which is Figure 45.

Control surfaces which will be used in structural analyses were examined in terms of aerodynamic loads, pressure distributions on them and some aerodynamic coefficients. The most critical case is the case of 15° angle of attack for both control surface models since maximum resultant aerodynamic pressure and normal forces occurs at 15° angle of attack. In Table 9, a summary of results which will be used in structural analyses is listed for both control surface models.

Table 9 CFD results Comparison between control surface models at  $\alpha=15^\circ$

	$C_{L,max}$	$C_{D,max}$	$F_{N,\alpha=15^\circ}$ (N)	$F_{A,\alpha=15^\circ}$ (N)	$X_{C.P.}$ (mm)	$Y_{C.P.}$ (mm)
Control Surface of Model-1	0.79	0.29	366.34	37.13	38.26	11.83
Control Surface of Model-1	0.77	0.27	356.17	29.90	38.57	11.27

It is seen in Table 9 that, aerodynamic coefficients including lift and drag, aerodynamic forces including normal and axial forces and center of pressure locations are close to each other for both control surfaces of model-1 and model-2. Since they have same thickness, span and chord length, lift coefficients and normal forces are close to each other. However, due to their different cross-sections and wedge angles, there are significant differences between drag coefficients and axial forces of both control surfaces. Control surface of model-1 has higher drag coefficients and it is subjected to higher axial forces because its wedge angle is greater than the wedge angle of control surface of model-2.

#### 4.6 Wind Tunnel Testing

In this section, small 3-D models of control surfaces are tested in supersonic wind tunnel. The goal of this section is to compare shock wave angles of control surface models at constant supersonic flight velocity and 0° angle of attack. Test specimens of both control surface models were tested at 1.6 Mach and 0° angle of attack. These specimens were manufactured from steel and they are shown in Figure 48 with their

chord lengths. As it is seen in Figure, specimens are manufactured with cylindrical bar in order to connect them with test setup.



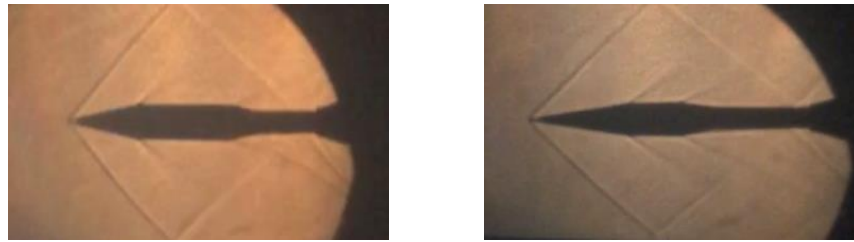
Figure 48 Test specimens and their chord lengths [mm]

Supersonic wind tunnel GA-10 is test section with stored high pressurized dry air in air storage tank. This air is discharged through a test chamber with variable cross-sectional areas and supersonic nozzle so supersonic flow occurs. Mach number is arranged in terms of test run pressure. Test setup is composed of six main parts which are high pressure tank, pressure control section, test settling chamber, supersonic nozzle, test section, exit throat and screens for monitoring the shock waves. Moreover, supersonic flow test can be performed at different angle of attack between  $-10^\circ$  and  $+10^\circ$ . The parts of test setup are shown in Figure 49.



Figure 49 Supersonic wind tunnel

Tests were carried out at  $0^\circ$  angle of attack and constant stream velocity which is 1.6 Mach for both control surface models. Due to the geometric limitation of wind tunnel, test specimens were manufactured with 10 mm span length. The chord length and thickness of specimen and control surface models are the same. The shock wave images of control surfaces are shown in Figure 50.



a) Control Surface of Model-1

b) Control Surface of Model-2

Figure 50 Shock waves at  $M=1.6$  and  $\alpha=0^\circ$

Moreover, control surface models are examined by 2D oblique shock wave theory. A shock wave with an oblique angle in terms of upstream flow is called oblique shock waves. Oblique shock angle,  $\beta$ , and downstream Mach number,  $M_2$ , can be calculated for a given Mach number of upstream flow,  $M_1$ , and wedge deflection angle,  $\theta$ , by oblique shock wave theory which is shown in Figure 51.

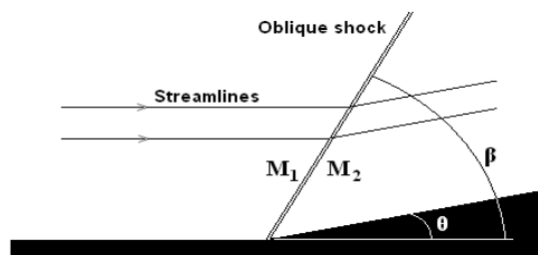


Figure 51 Oblique Shock wave over a wedge [36]

Oblique shock wave angle can be calculated by relation between  $\theta$ ,  $\beta$  and Mach number. By using the continuity equations and assuming that tangential velocity is the same across the shock, the trigonometric relation between Mach number, wedge deflection angle and shock angle is represented in Eq. 20. Note that, this equation is valid for perfect gas. [36]

$$\tan\theta = 2\cot(\beta)\frac{(M_1^2\sin^2\beta) - 1}{M_1^2(\gamma + \cos 2\beta) + 2} \quad (20)$$

Figure 52 [36] shows that oblique shock angle,  $\beta$ , is a function of wedge deflection angle,  $\theta$ , for a constant Mach number. In this Figure, wedge angles of control surfaces and shock wave angles at  $M=1.6$  are shown.

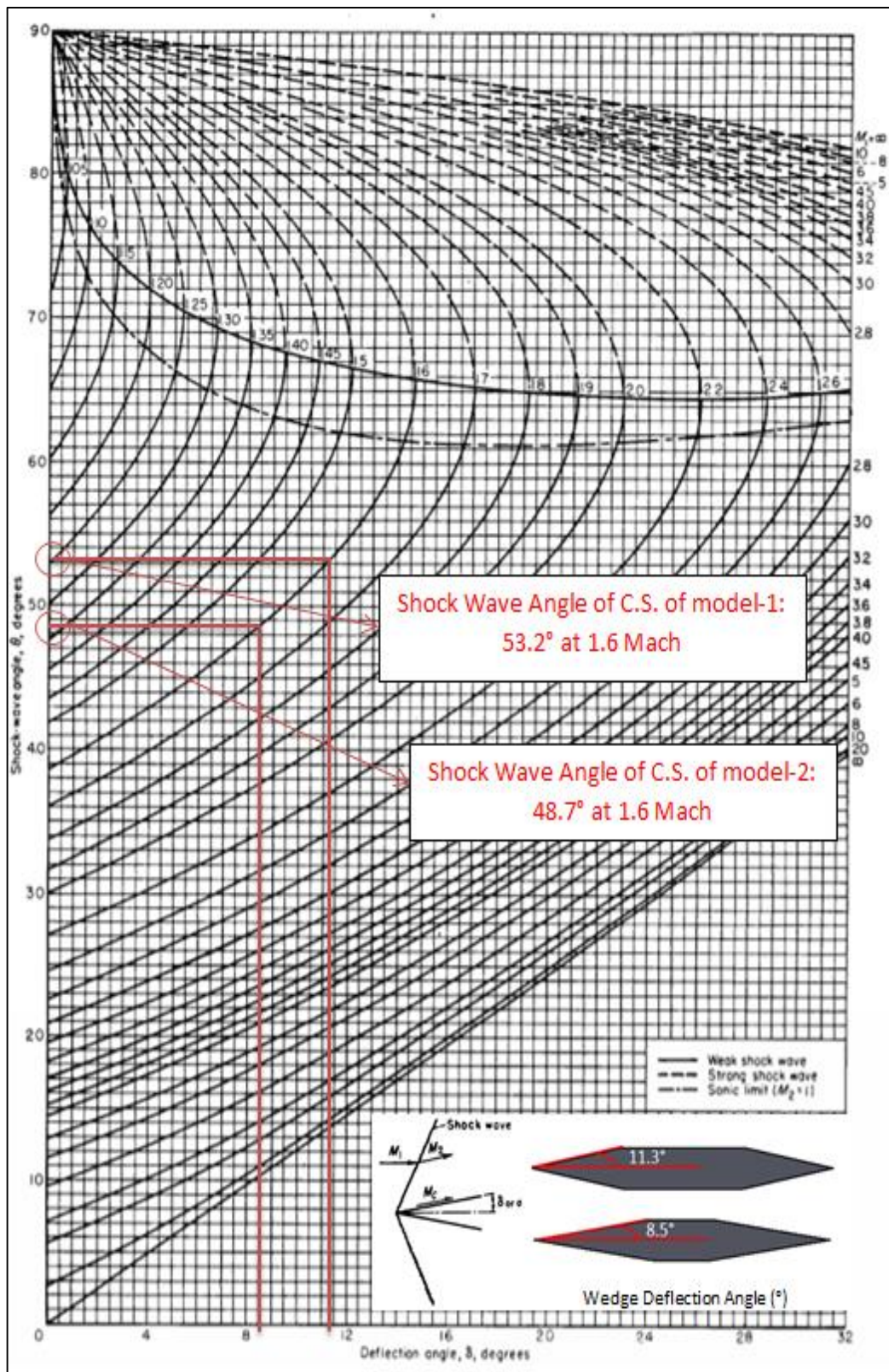


Figure 52 Shock Wave versus Deflection angle of wedge with control surface 2D theoretical results [36]

Then, shock wave angles obtained from test, 3D CFD analyses and 2D oblique shock wave theory are compared. The shock wave angles of test and CFD analyses of both control surface models are shown in Figure 53.

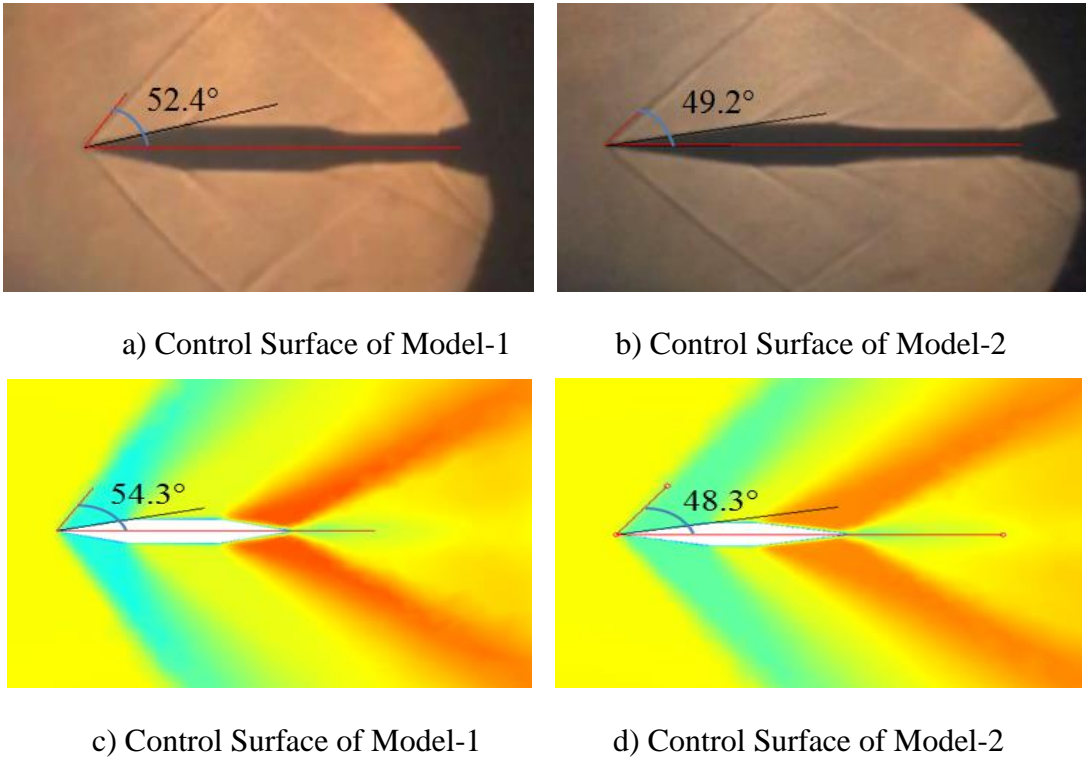


Figure 53 Shock wave comparison of CFD and test data at M=1.6 and  $\alpha=0^\circ$

The shock wave angles at 1.6 Mach and  $0^\circ$  angle of attack acquired from test data, 3D CFD results and 2D oblique shock wave theory are listed in Table 10.

Table 10 Shock wave comparison Table

	Shock Wave Angle of Control Surface of Model-1 [°]	Shock Wave Angle of Control Surface of Model-2 [°]
Test Result (3D)	52.4	49.2
CFD Result (3D)	54.3	48.3
Shock Wave Theory (2D)	53.2	48.7

According to Table 10, there are some difference between test, CFD and analytical results. It can be one of the reasons of difference between test data and analytical solution is manufacturing tolerances. The machining process of wedge-typed geometries is very difficult due to the sensitivity of wedge angle and the hardness of material. As a result of this difficulty, designer should form the technical drawing with larger tolerance intervals. These conditions cause some percentage difference between test data and 2D analytical solution.



## CHAPTER 5

### STRUCTURAL ANALYSIS AND TESTS

In this chapter, control surfaces of model-1 and model-2 are examined in terms of their strengths. Control surfaces with modified double wedge are modeled laminated composite structure and different stacking sequences including  $0^\circ$ ,  $30^\circ$ ,  $45^\circ$ ,  $60^\circ$ , and  $90^\circ$  unidirectional layers are investigated in order to decrease maximum tip deflection under the maximum aerodynamic loads. A set of static structural analyses are conducted by using the Nastran® 101 solver which is linear static analysis tool. Different ply orientations of the laminated control surfaces are examined by using an algorithm created in Matlab®. A verification study is carried out so as to verify the algorithm. During the verification study, a laminated composite plate subjected to bending moment is analyzed by using 2D shell elements. Also, the analytical solutions are performed in order to compare the analytical solutions with 2-D analysis results. At the parametric study stage, the algorithm changes the orientation angles of each lamina and runs the Nastran® in each step. The main goal of the algorithm is manipulate the input file of Nastran having “.bdf” extension and run the Nastran solver for every manipulated step. During the analyses, unidirectional carbon/epoxy layers are used. In order to obtain desired strength and tip deflection all configurations of laminated control surfaces are examined in terms of four different failure criteria which are Tsai-Wu, Maximum Stress, Tsai- Hill and Hoffman failure criteria.

## 5.1 Description of Material

Laminated composites are composed of more than one single layer called lamina. Lamina consists of a matrix material and reinforcing fibers. For better understanding of the lamina macromechanics, the knowledge about mechanical properties of materials is required. The materials can be divided into five main categories depending on their anisotropic behavior. These are anisotropic, monoclinic, orthotropic, transversely isotropic and isotropic materials.

Most general anisotropic materials have no plane of symmetry in terms of the material properties. In other words, they have different mechanical properties in different directions and these materials are directionally dependent. Stress-strain relationship in  $x_1$ ,  $x_2$  and  $x_3$  for an anisotropic material is given in Eq. 21 [41].

$$\begin{Bmatrix} \sigma_1 \\ \sigma_2 \\ \sigma_3 \\ \tau_{23} \\ \tau_{13} \\ \tau_{12} \end{Bmatrix} = \begin{bmatrix} C_{11} & C_{12} & C_{13} & C_{14} & C_{15} & C_{16} \\ C_{21} & C_{22} & C_{23} & C_{24} & C_{25} & C_{26} \\ C_{31} & C_{32} & C_{33} & C_{34} & C_{35} & C_{36} \\ C_{41} & C_{42} & C_{43} & C_{44} & C_{45} & C_{46} \\ C_{51} & C_{52} & C_{53} & C_{54} & C_{55} & C_{56} \\ C_{61} & C_{62} & C_{63} & C_{64} & C_{65} & C_{66} \end{bmatrix} \begin{Bmatrix} \epsilon_1 \\ \epsilon_2 \\ \epsilon_3 \\ \gamma_{23} \\ \gamma_{13} \\ \gamma_{12} \end{Bmatrix} \quad (21)$$

Where,

$$C_{ij} = C_{ji} \ \& \ i, j = 1, 2, \dots, 6 \quad (22)$$

Note that “ $C_{ij}$ ” is the elements of stiffness matrix in  $x_1$ ,  $x_2$  and  $x_3$  directions. Due to the symmetry of stiffness matrix in  $x$ ,  $y$  and  $z$  directions, 21 of 36 elements are independent in stiffness matrix.

Monoclinic materials have single symmetry plane with respect to material properties. Different from most general anisotropic materials, stiffness matrices of monoclinic materials have some zero terms due to the plane of symmetry. Stress-strain relationship in  $x_1$ ,  $x_2$  and  $x_3$  for a monoclinic material is given in Eq. 23 [41].

$$\begin{Bmatrix} \sigma_1 \\ \sigma_2 \\ \sigma_3 \\ \tau_{23} \\ \tau_{13} \\ \tau_{12} \end{Bmatrix} = \begin{bmatrix} C_{11} & C_{12} & C_{13} & 0 & 0 & C_{16} \\ C_{21} & C_{22} & C_{23} & 0 & 0 & C_{26} \\ C_{31} & C_{32} & C_{33} & 0 & 0 & C_{36} \\ 0 & 0 & 0 & C_{44} & C_{45} & 0 \\ 0 & 0 & 0 & C_{54} & C_{55} & 0 \\ C_{61} & C_{62} & C_{63} & 0 & 0 & C_{66} \end{bmatrix} \begin{Bmatrix} \epsilon_1 \\ \epsilon_2 \\ \epsilon_3 \\ \gamma_{23} \\ \gamma_{13} \\ \gamma_{12} \end{Bmatrix} \quad (23)$$

If the x-y plane is considered as plane of symmetry, shear stresses from the other planes which are y-z and z-x contributes only to the shear strains. Normal stresses do not contributes any shear strains. In addition to this, due to the symmetry of stiffness matrix in x, y and z directions, 13 of 36 elements are independent in stiffness matrix. Orthotropic materials have three mutually orthogonal symmetric planes of material properties. Composites with reinforcing fibers are generally categorized as orthotropic materials due to their three orthogonal plane of symmetry. Stress-strain relationship in  $x_1$ ,  $x_2$  and  $x_3$  for an orthotropic material is given in Eq. 24.

$$\begin{Bmatrix} \sigma_1 \\ \sigma_2 \\ \sigma_3 \\ \tau_{23} \\ \tau_{13} \\ \tau_{12} \end{Bmatrix} = \begin{bmatrix} C_{11} & C_{12} & C_{13} & 0 & 0 & 0 \\ C_{21} & C_{22} & C_{23} & 0 & 0 & 0 \\ C_{31} & C_{32} & C_{33} & 0 & 0 & 0 \\ 0 & 0 & 0 & C_{44} & 0 & 0 \\ 0 & 0 & 0 & 0 & C_{55} & 0 \\ 0 & 0 & 0 & 0 & 0 & C_{66} \end{bmatrix} \begin{Bmatrix} \epsilon_1 \\ \epsilon_2 \\ \epsilon_3 \\ \gamma_{23} \\ \gamma_{13} \\ \gamma_{12} \end{Bmatrix} \quad (24)$$

The intersections of three plane of symmetry are called principal material directions. When the normal stresses are applied in this direction, the material called specially orthotropic material. These materials have 9 independent elastic constants in their stiffness matrix [41].

Transversely isotropic materials have three plane of symmetry like orthotropic materials but, the difference between them is that in transversely isotropic materials, one of the planes of symmetry shows the properties of isotropic materials. Composites reinforced with continuous fibers can be given as an example of such

materials. Stress-strain relationship in  $x_1$ ,  $x_2$  and  $x_3$  for a transversely isotropic material is given in Eq. 25.

$$\begin{Bmatrix} \sigma_1 \\ \sigma_2 \\ \sigma_3 \\ \tau_{23} \\ \tau_{13} \\ \tau_{12} \end{Bmatrix} = \begin{bmatrix} C_{11} & C_{12} & C_{12} & 0 & 0 & 0 \\ C_{12} & C_{22} & C_{23} & 0 & 0 & 0 \\ C_{12} & C_{23} & C_{22} & 0 & 0 & 0 \\ 0 & 0 & 0 & \frac{C_{22} - C_{23}}{2} & 0 & 0 \\ 0 & 0 & 0 & 0 & C_{66} & 0 \\ 0 & 0 & 0 & 0 & 0 & C_{66} \end{bmatrix} \begin{Bmatrix} \epsilon_1 \\ \epsilon_2 \\ \epsilon_3 \\ \gamma_{23} \\ \gamma_{13} \\ \gamma_{12} \end{Bmatrix} \quad (25)$$

Note that, there are 5 independent terms in stiffness matrix of transversely isotropic materials.

Isotropic materials are the materials that properties of them are the same in all directions. Thus, these materials contain an infinite number of symmetry planes. Stress-strain relationship in  $x_1$ ,  $x_2$  and  $x_3$  for an isotropic material is given in Eq. 26 [41].

$$\begin{Bmatrix} \sigma_1 \\ \sigma_2 \\ \sigma_3 \\ \tau_{23} \\ \tau_{13} \\ \tau_{12} \end{Bmatrix} = \begin{bmatrix} C_{11} & C_{12} & C_{12} & 0 & 0 & 0 \\ C_{12} & C_{11} & C_{12} & 0 & 0 & 0 \\ C_{12} & C_{12} & C_{11} & 0 & 0 & 0 \\ 0 & 0 & 0 & \frac{C_{11} - C_{12}}{2} & 0 & 0 \\ 0 & 0 & 0 & 0 & \frac{C_{11} - C_{12}}{2} & 0 \\ 0 & 0 & 0 & 0 & 0 & \frac{C_{11} - C_{12}}{2} \end{bmatrix} \begin{Bmatrix} \epsilon_1 \\ \epsilon_2 \\ \epsilon_3 \\ \gamma_{23} \\ \gamma_{13} \\ \gamma_{12} \end{Bmatrix} \quad (26)$$

Note that, there are 2 independent terms in stiffness matrix of transversely isotropic materials. In Table 11, number of non-zero and independent elastic constants is given for both two and three dimensional states.

Table 11 Elastic constants of Different Materials [42]

Material	2-D State		3-D State	
	Number of Non-zero Constants	Number of Independent Constants	Number of Non-zero Constants	Number of Independent Constants
Anisotropic	9	6	36	21
Generally Orthotropic	9	4	36	9
Specially Orthotropic	5	4	12	9
Transversely Isotropic	5	4	12	5
Isotropic	5	2	12	2

In structural analysis and testing part, mechanical properties of CE 1007/310/37 which is a carbon/epoxy type of prepreg are used. Also, thickness a single layer after curing operation is 0.3 mm. This material is a unidirectional prepreg and typically orthotropic material which is shown in Figure 54. Also, thickness a single layer after curing operation is 0.3 mm.

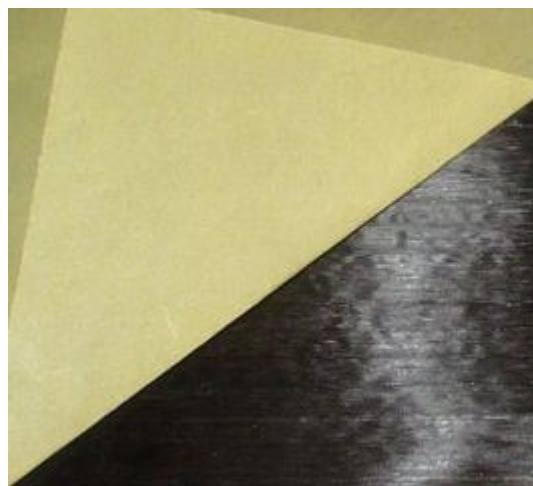


Figure 54 Carbon/Epoxy CE 1007/310/37 Prepreg

The mechanical properties of CE 1007/310/37 are shown in Table 12.

Table 12 Mechanical Properties of CE 1007/310/37 [43]

<b>Material Properties</b>	<b>Value</b>
E <sub>1</sub>	130563 MPa
E <sub>2</sub>	6873 MPa
$\nu_{12}$	0.32
G <sub>12</sub>	4953 MPa
X <sub>t</sub>	1968 MPa
X <sub>c</sub>	953 MPa
Y <sub>t</sub>	29 MPa
Y <sub>c</sub>	119 MPa
S	51 MPa

## 5.2 Initial structural Analysis

In this chapter, laminated composite control surfaces with symmetric lay-up are analyzed in order to obtain ply orientations causing less tip deflection of both models. Before the parametrization, both control surfaces are modeled as unidirectional laminates. At this step, each layer is modeled as 0° in Patran®. Patran® is a pre and post-processing software providing modeling materials, simulating loads, meshing and analysis setup for a solver such as Nastran®, Marc® and Abaqus®. The reason why each layers modeled as 0° is to obtain an input file for Nastran® solver. This file has an extension of “.bdf”. After running the first analysis, the output file of Nastran with the extension of “.f06” is also obtained. Control surfaces are modeled in 2-D plane and meshed with shell elements in order to reduce computational cost. The first model of control surfaces is shown in Figure 55 and 56.

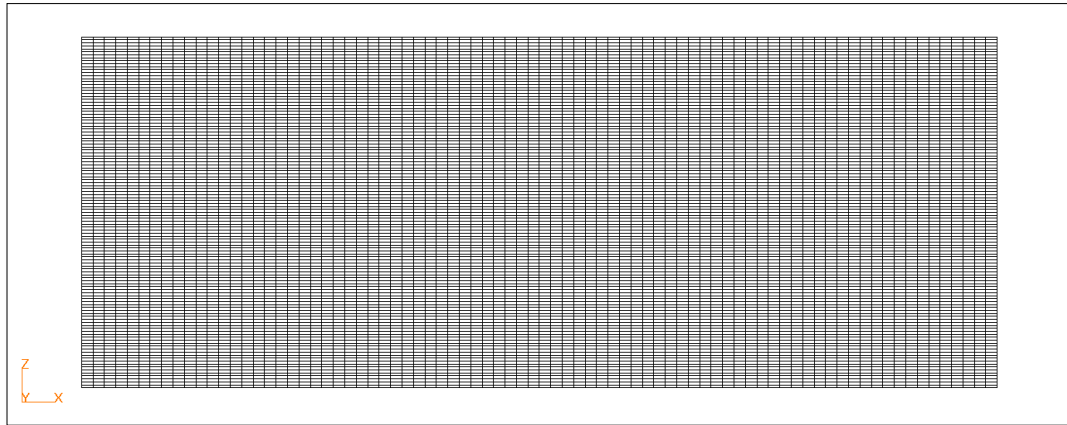
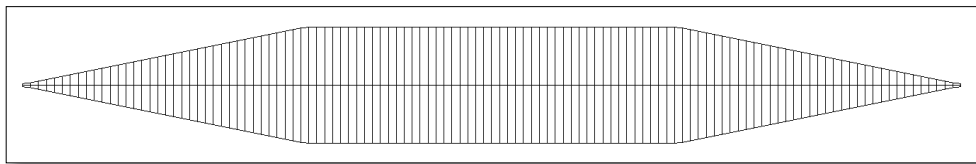
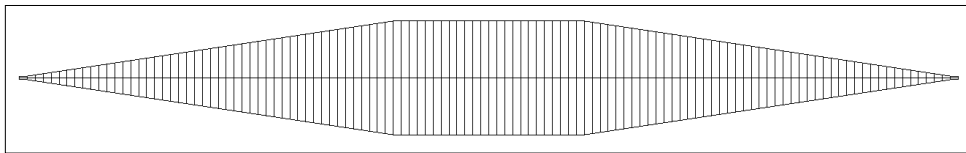


Figure 55 Shell mesh model of structural analyses



a) Control Surface of Model-1

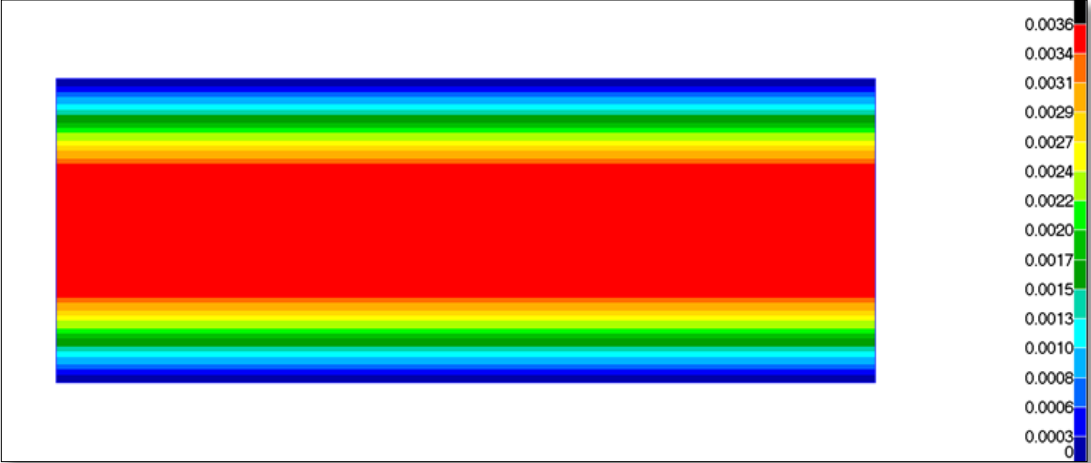


b) Control Surface of Model-2

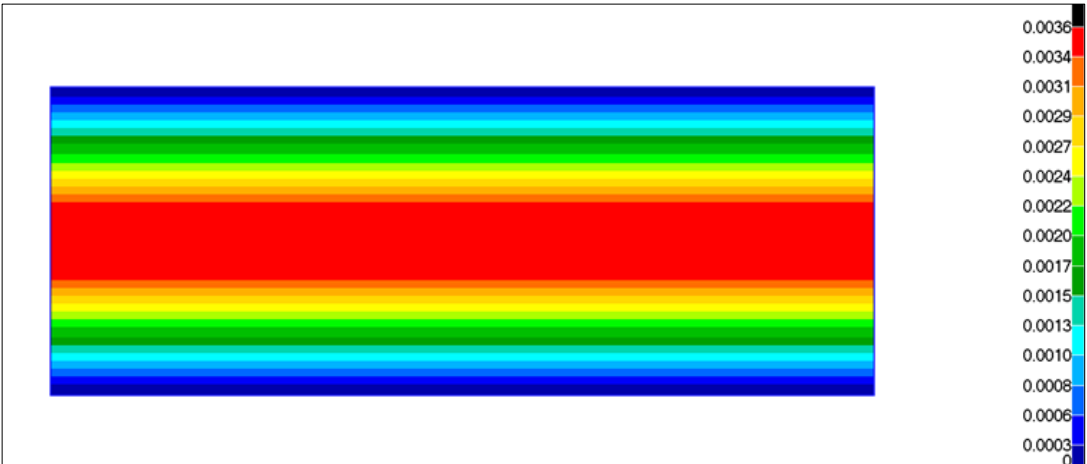
Figure 56 Shell element thicknesses

Due to the same chord and span length of control surfaces of model-1 and model-2, same mesh model are used. In this model, there are 9440 elements. The significant thing is to arrange the element thicknesses in order to model wedge slopes. The thickness of control surfaces is 3.6 mm and the lamina thickness is 0.3 mm, so there are 12 main layers in this model. In order to arrange slopes of the wedges, different thickness are assigned to the each shell. In Figure 57, shell element thicknesses are shown for both control surface models.

It is seen in Figure 57 that, different thicknesses are assigned to each elements through the span in order to model wedge angles of control surfaces.



a) Elements of control surface of model-1



b) Elements of control surface of model-2

Figure 57 Shell element thicknesses (given in meter)

**5.3 Boundary Conditions of Initial Analysis**

In order to get “.bdf” and “.f06” files for the parametrization part, all plies are aligned in the direction of x axis so unidirectional laminated composite is formed. The stacking sequence is  $[0^\circ/0^\circ/0^\circ/0^\circ/0^\circ/0^\circ]_s$ .

First of all, material properties are assigned to each element of models. After that, boundary conditions are applied. Nodes at the root of the control surfaces are modeled as fixed support. Maximum pressure distributions obtained from CFD analyses are applied so as to simulate aerodynamic loading. To perform this step, the output file of Fluent® including the pressure distribution on the control surfaces is utilized as an input file of Patran®.

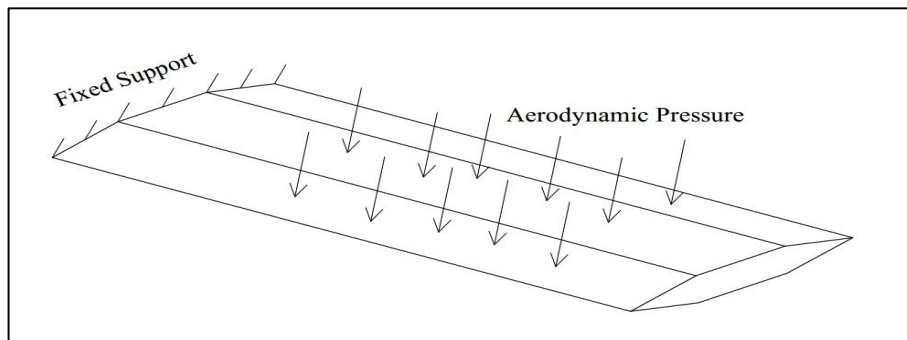
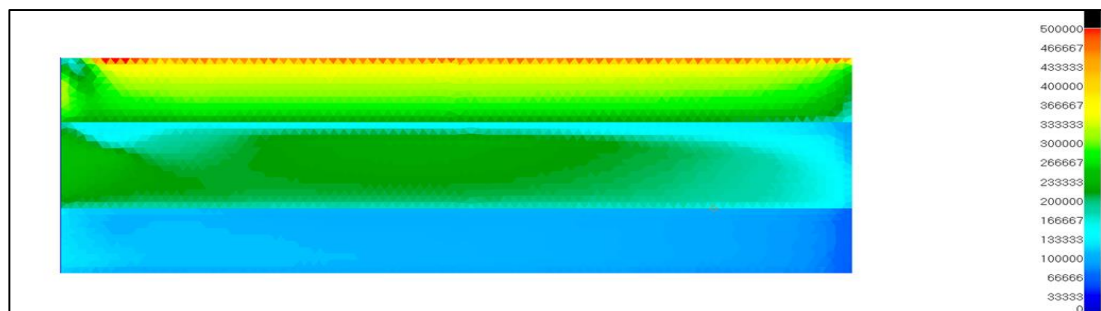
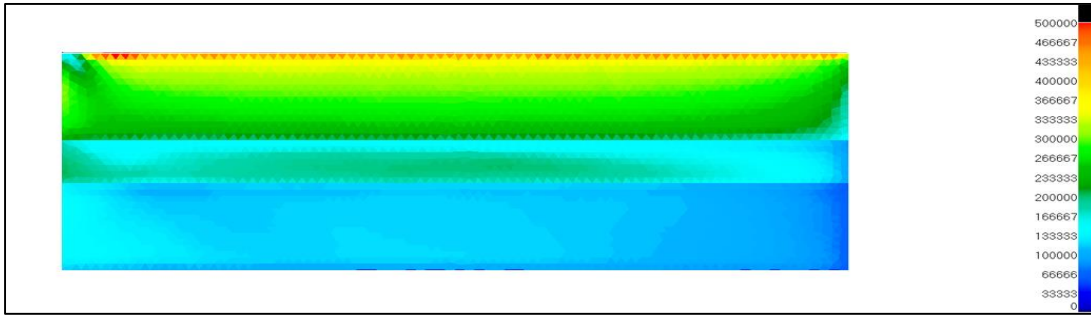


Figure 58 Boundary conditions of control surfaces

Boundary conditions of structural analysis part of the study are shown in Figure 58. Pressure values of each element are interpolated to the 2-D structural elements. Pressure distribution of the initial analyses of both control surface models are shown in Figure 59.



a) Elements of control surface of model-1

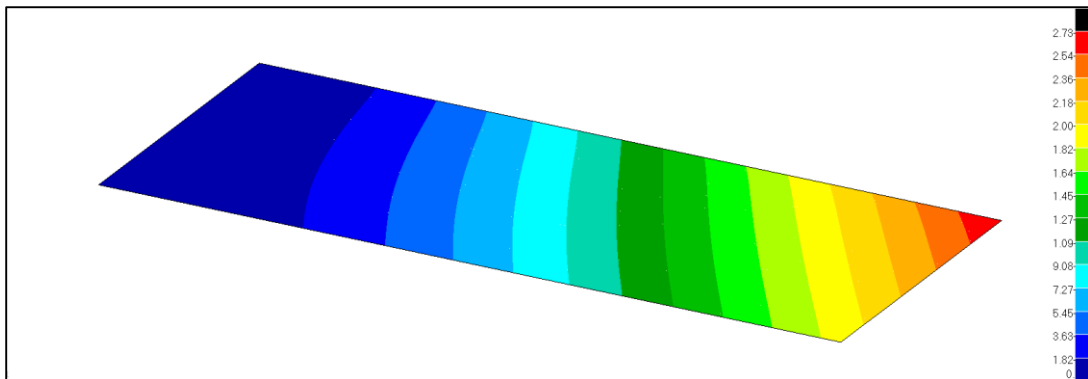


b) Elements of control surface of model-2

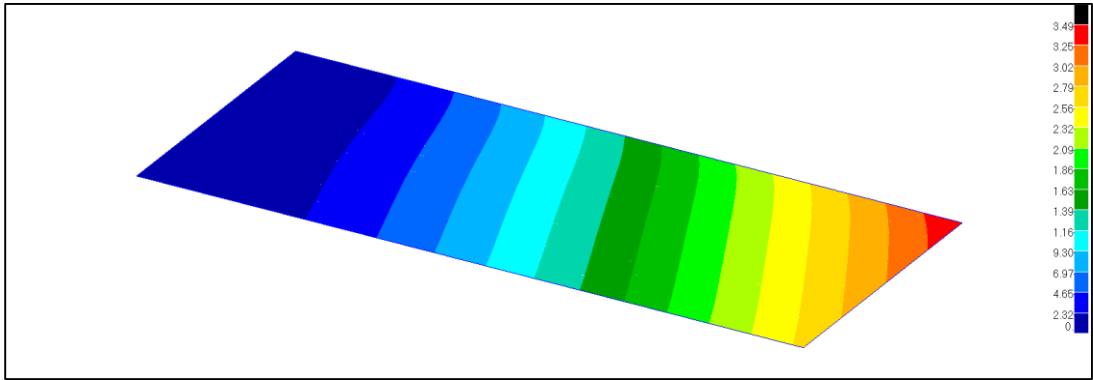
Figure 59 Pressure distributions in Pa at  $\alpha=15^\circ$

#### 5.4 Results of Initial Analysis

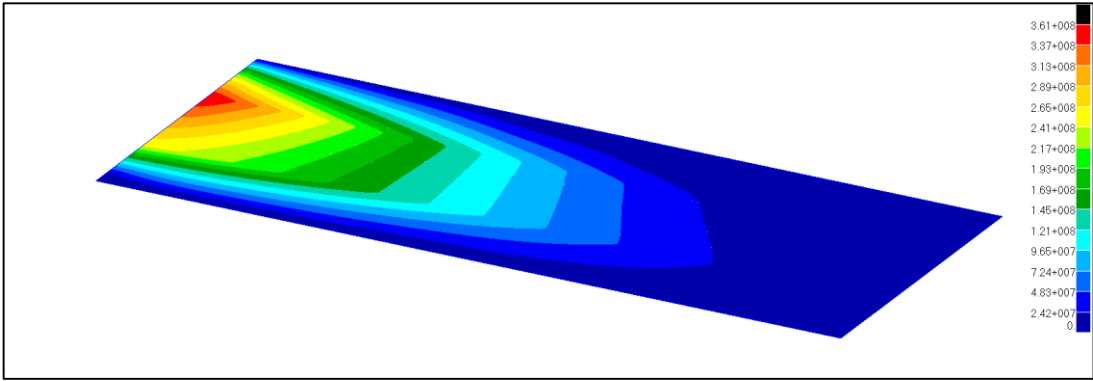
Initial analyses are performed for both control surfaces of model-1 and model-2. The input file, “.bdf”, and output file “.f06” of Nastran® are obtained in order to use them in parametric study of stacking sequences. Moreover, stress distribution on the control surfaces and total deformation due to aerodynamic loading are shown in Figures 60 and 61.



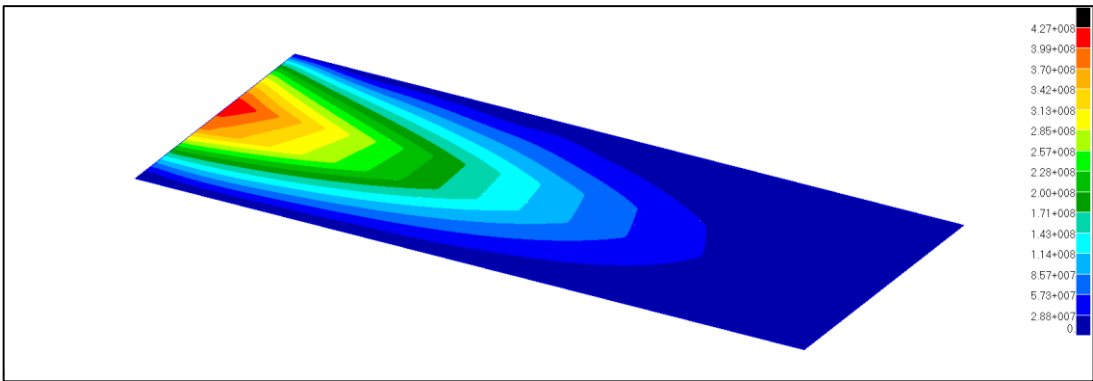
a) Elements of control surface of model-1



b) Elements of control surface of model-2  
 Figure 60 Total Deformation in mm



a) Elements of control surface of model-1



b) Elements of control surface of model-2  
 Figure 61 Von Mises stress distribution in Pa

The maximum tip deflection and maximum stress results of control surfaces is listed in Table 13.

Table 13 Results of Initial Analysis

	Control Surface of Model-1	Control Surface of Model-2
Maximum Tip Deflection [mm]	2.73	3.49
Maximum von Mises Stress [MPa]	361	427

**5.5 Mesh Sensitivity Analysis**

In this section, mesh convergence study is carried out in order to obtain converged mesh. Maximum tip deflection values which are observed at same element for all mesh sizes are utilized. In this part of the study, four different mesh sizes are used. In In Figure 62, maximum tip deflection variation with mesh sizes of control surface of model-1 having  $[0^\circ/0^\circ/0^\circ/0^\circ/0^\circ/90^\circ]_s$  lay-up is shown.

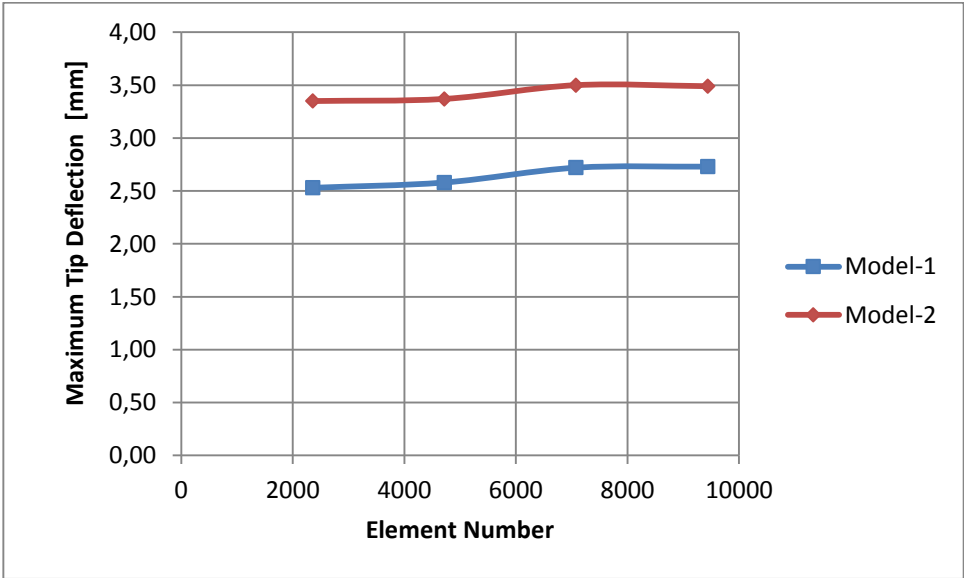


Figure 62 Maximum tip deflections of different mesh sizes in mm

Maximum tip deflection values converge at the mesh size with 9440 elements and this mesh is used in structural parametric study part of the thesis.

## **5.6 Parametric Study of Stacking Sequence**

In this part of this study, ply orientations of laminated composite control surfaces are investigated in terms of the tip deflections by considering four different failure criteria. These are Tsai-Wu, Maximum Stress, Tsai-Hill and Hoffman failure theories. Maximum aerodynamic pressure obtained from 15° angle of attack CFD analyses, is implemented to the 2D structural model. One-way static aeroelastic analyses are carried out by this way. The only parameter which is investigated and modified in parametric study part is the layer orientation of laminated control surfaces. For this step, two different algorithms are created in Matlab® for both control surface models. In the algorithm, “.bdf” and “.f06” files are modified in terms of the orientation of the unidirectional composite layers. As it is mentioned in the part of initial structural analysis, control surfaces are formed of 12 layers. Due to the symmetric lay-up, there are 6 of 12 layers in order to change their orientations. During the parametrization, 0°, 30°, 45°, 60° and 90° angles of orientations are used. In other words, 6 layers are examined in terms of 5 different ply orientation so 15625 different analyses are carried out for each control surface model.

### **5.6.1 Parametric Study Routine**

First of all, an algorithm written in Matlab® opens and reads the “.bdf” file and it creates a new “.bdf” file. It writes all required information to the new file line by line with the “fprintf” command. When it comes to PCOMP card, the material orientation angles of each element are increased and new PCOMP card is written in new input file. The boundary conditions are printed without any change. After forming all lines, new input file is closed by the code with the “fclose” command. Then, the algorithm runs Nastran by using new input file and an output file is obtained. By using “fopen” command, the algorithm save all stress and displacement values to the Matlab workspace. After getting these values, the code forms a matrix with the dimension of number of elements in order to print element status. Failure status of each element is investigated with respect to failure equations. If an element failed in terms of a failure criteria, the code prints “0” to the element failure status matrix otherwise it is written “1”.

By this way, all elements are investigated in terms of four different criteria. This step is repeated for each failure criterion. Finally, the algorithm prints results and material orientations to an “.xlsx” file line by line. Printed results are maximum deformations, maximum stress values in each direction (x, y, and xy directions), and failure status of all theories which are Maximum Stress, Tsai-Wu, Tsai-Hill and Hoffman failure criteria. The algorithm is given in Figure 63.

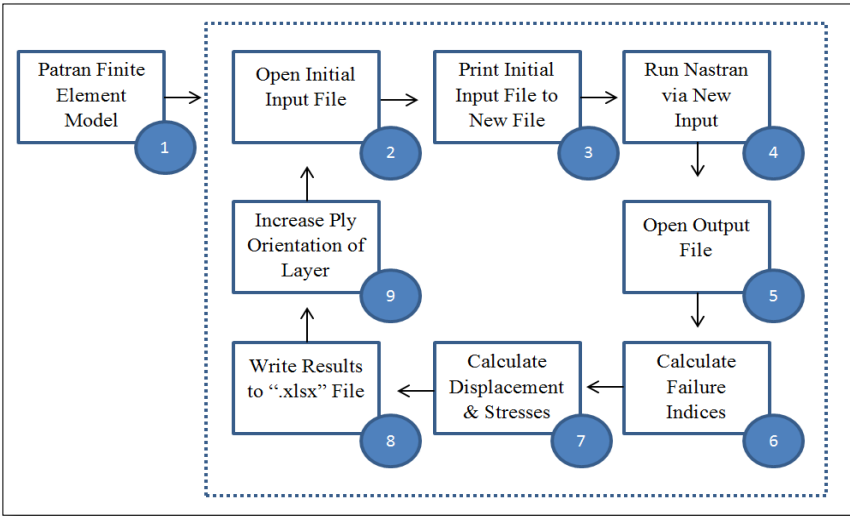


Figure 63 Algorithm flowchart of parametric study for stacking sequence

**5.6.2 Code Verification Study**

In order to verify the algorithm modifying ply orientations, a case verification study is performed. In this section, an analytical and a finite element solution are obtained for a laminated composite plate subjected to bending load. For better understanding of the structural analysis of laminated composites, the knowledge of classical lamination theory is essential.

**5.6.2.1 Classical Lamination Theory**

A laminate is a batch of unidirectional composite layers. It is defined by the fiber directions of each layer. In Figure 64, an example of laminate and its notation is shown.

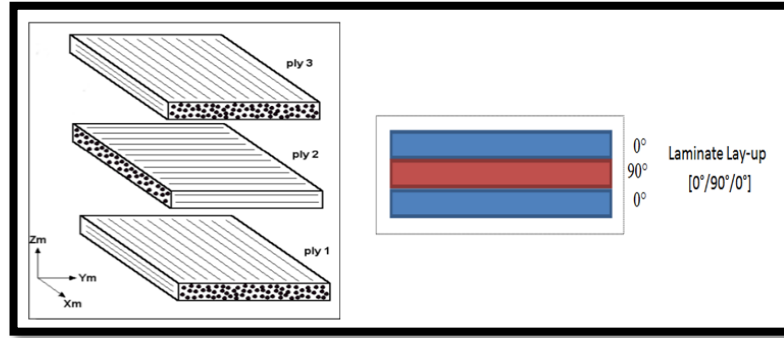


Figure 64 Laminate with  $[0^\circ/90^\circ/0^\circ]$  ply orientation

Classical lamination theory is an extension of classical plate theory proposed by Kirchhoff-Love. On the other hand, the extended theory for laminates needs some modification by considering the inhomogeneity in thickness direction. In order to simplify the theory, there are some assumptions. The first one is that, the laminates are composed to excellently bonded layers. In other words, there is no slip condition between layers. Secondly, lamina is taken into consideration as homogeneous layer with effective properties. Thirdly, each lamina is considered in a plane stress state and it can exhibit isotropic, transversely isotropic or orthotropic behavior. Finally, a laminated structure deforms according to Kirchhoff-Love assumptions that the mid-plane normal remains straight after deformation and normal keeps the same length [45].

According to the theory, in-plane displacements change linearly throughout the laminate thickness. As a result of this, in-plane strains are non-zero including 2 normal strains and 1 shear strains varying linearly through the thickness. These are expressed in Eq. 27. In this equation,  $\epsilon_1^0$  and  $\epsilon_2^0$  terms are the mid-plane strains,  $\epsilon_6^0$  term is mid-plane shear strain,  $\kappa_1$  and  $\kappa_2$  are curvatures of bending,  $\kappa_6$  is the twisting curvature and  $z$  is the thickness.

$$\begin{Bmatrix} \epsilon_1 \\ \epsilon_2 \\ \epsilon_6 \end{Bmatrix} = \begin{Bmatrix} \epsilon_1^0 \\ \epsilon_2^0 \\ \epsilon_6^0 \end{Bmatrix} + z \begin{Bmatrix} \kappa_1 \\ \kappa_2 \\ \kappa_6 \end{Bmatrix} \quad (27)$$

The stress state in a layer which is denoted by k can be shown in Eq. 28.

$$\begin{Bmatrix} \sigma_1 \\ \sigma_2 \\ \sigma_6 \end{Bmatrix} = \begin{bmatrix} \bar{Q}_{11} & \bar{Q}_{12} & \bar{Q}_{16} \\ \bar{Q}_{12} & \bar{Q}_{22} & \bar{Q}_{26} \\ \bar{Q}_{16} & \bar{Q}_{26} & \bar{Q}_{66} \end{bmatrix}_k \begin{Bmatrix} \epsilon_1 \\ \epsilon_2 \\ \epsilon_6 \end{Bmatrix} \quad (28)$$

The matrix with “ $\bar{Q}$ ” terms is called as transformed reduced stiffness matrix of a composite layer and it can be shown in Eq. 29.

$$[\bar{Q}] = [T]^{-1}[Q][T]^T \quad (29)$$

Matrix [T] is second order transformation matrix and it can be expressed as:

$$[T] = \begin{bmatrix} \cos^2\theta & \sin^2\theta & 2\cos\theta\sin\theta \\ \sin^2\theta & \cos^2\theta & -2\cos\theta\sin\theta \\ -\cos\theta\sin\theta & \cos\theta\sin\theta & \cos^2\theta - \sin^2\theta \end{bmatrix} \quad (30)$$

Also, matrix [Q] is the reduced stiffness matrix which can be expressed for plane stress condition of an orthotropic material as:

$$[Q] = \begin{bmatrix} \frac{E_1}{1 - \nu_{12}\nu_{21}} & \frac{\nu_{12}E_2}{1 - \nu_{12}\nu_{21}} & 0 \\ \frac{\nu_{12}E_2}{1 - \nu_{12}\nu_{21}} & \frac{E_2}{1 - \nu_{12}\nu_{21}} & 0 \\ 0 & 0 & G_{12} \end{bmatrix} \quad (31)$$

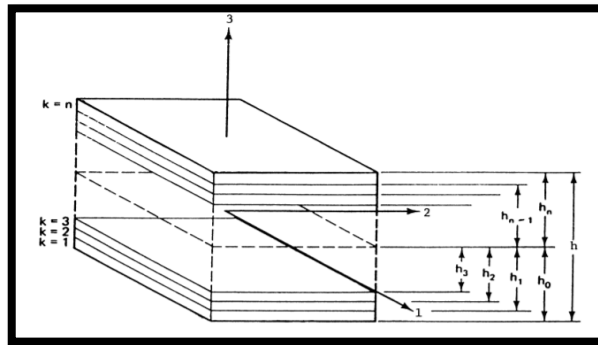
The in-plane forces per unit width can be expressed by the Eq. 32 for a laminated plate with “n” number of plies.  $N_1$ ,  $N_2$  is normal forces of in-plane state and  $N_6$  is shear force of in-plane stress state.

$$\begin{Bmatrix} N_1 \\ N_2 \\ N_6 \end{Bmatrix} = \int_{-h/2}^{h/2} \begin{Bmatrix} \sigma_1 \\ \sigma_2 \\ \sigma_6 \end{Bmatrix} dz = \sum_{k=1}^n \int_{h_{k-1}}^{h_k} \begin{Bmatrix} \sigma_1 \\ \sigma_2 \\ \sigma_6 \end{Bmatrix} dz \quad (32)$$

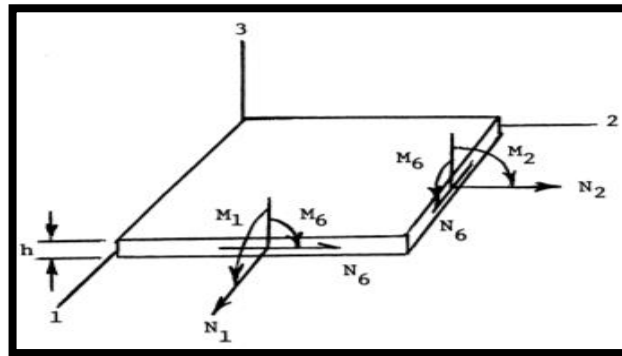
In a similar way, resultant moment components are expressed by equation 33.  $M_1$ ,  $M_2$  is bending moments of in-plane state and  $M_6$  is twisting moment per unit width.

$$\begin{Bmatrix} M_1 \\ M_2 \\ M_6 \end{Bmatrix} = \int_{-h/2}^{h/2} z \begin{Bmatrix} \sigma_1 \\ \sigma_2 \\ \sigma_6 \end{Bmatrix} dz = \sum_{k=1}^n \int_{h_{k-1}}^{h_k} z \begin{Bmatrix} \sigma_1 \\ \sigma_2 \\ \sigma_6 \end{Bmatrix} dz \quad (33)$$

The laminate with “n” number of plies and resultant in-plane forces and moments acting on the laminate is shown in Figure 65 [46].



b) n-ply laminate



b) In-plane forces and moments

Figure 65 n-ply laminate and in-plane forces and moments [46]

By substituting Eq. 27 and Eq. 28 into Eq. 32 and Eq. 33 respectively, Eq. 34 and 35 are obtained. Thus, resultant force and moments of in-plane state is calculated after obtaining the extensional, coupling and bending stiffness matrix.

The matrix with “A” terms is called extensional stiffness matrix, the matrix with “B” terms is called coupling stiffness matrix and matrix with “D” terms is called bending stiffness matrix.

$$\begin{Bmatrix} N_1 \\ N_2 \\ N_6 \end{Bmatrix} = \begin{bmatrix} A_{11} & A_{12} & A_{16} \\ A_{12} & A_{22} & A_{26} \\ A_{16} & A_{26} & A_{66} \end{bmatrix} \begin{Bmatrix} \epsilon_1^0 \\ \epsilon_2^0 \\ \epsilon_6^0 \end{Bmatrix} + \begin{bmatrix} B_{11} & B_{12} & B_{16} \\ B_{12} & B_{22} & B_{26} \\ B_{16} & B_{26} & B_{66} \end{bmatrix} \begin{Bmatrix} K_1 \\ K_2 \\ K_6 \end{Bmatrix} \quad (34)$$

$$\begin{Bmatrix} M_1 \\ M_2 \\ M_6 \end{Bmatrix} = \begin{bmatrix} B_{11} & B_{12} & B_{16} \\ B_{12} & B_{22} & B_{26} \\ B_{16} & B_{26} & B_{66} \end{bmatrix} \begin{Bmatrix} \epsilon_1^0 \\ \epsilon_2^0 \\ \epsilon_6^0 \end{Bmatrix} + \begin{bmatrix} D_{11} & D_{12} & D_{16} \\ D_{12} & D_{22} & D_{26} \\ D_{16} & D_{26} & D_{66} \end{bmatrix} \begin{Bmatrix} K_1 \\ K_2 \\ K_6 \end{Bmatrix} \quad (35)$$

Extensional stiffness matrix terms are calculated by using the Eq. 36.

$$A_{ij} = \int_{-h/2}^{h/2} \bar{Q}_{ij} dz = \sum_{k=1}^n (h_k - h_{k-1}) (\bar{Q}_{ij})_k \quad i, j = 1, 2, 6 \quad (36)$$

Coupling stiffness matrix terms are calculated by using the Eq. 37.

$$B_{ij} = \int_{-h/2}^{h/2} z \bar{Q}_{ij} dz = \frac{1}{2} \sum_{k=1}^n (h_k^2 - h_{k-1}^2) (\bar{Q}_{ij})_k \quad i, j = 1, 2, 6 \quad (37)$$

Then, bending stiffness matrix terms are calculated by using the Eq. 38.

$$D_{ij} = \int_{-h/2}^{h/2} z^2 \bar{Q}_{ij} dz = \frac{1}{3} \sum_{k=1}^n (h_k^3 - h_{k-1}^3) (\bar{Q}_{ij})_k \quad i, j = 1, 2, 6 \quad (38)$$

### 5.6.2.2 Plate Bending Analysis with Parametric Study Algorithm

The goals of this section are to control the accuracy of the finite element results obtained by the Matlab® code and compare these with the results of analytical solution. Finite element results are acquired by using the algorithm without change in stacking sequence. In other words, parametric study algorithm is run for an iteration including single ply orientation of the plate. However, a modification is required to form PCOMP card of the input file. All elements in plate model have same material properties and layer thicknesses while elements of control surface models have different material properties and layer thicknesses due to their tapered sections. As a result of this, printing method of material properties in input file is modified.

The plate model and its boundary conditions used in case verification study are shown in Figure 66. As it is seen in this Figure, the plate has same length, width and thickness with control surface models. At the free end of plate, a transverse load causing the bending moment is applied. Also, the mechanical properties of carbon-epoxy CE 1007/310/37 are used. Ply orientation of the plate is  $[0^\circ/90^\circ/0^\circ]$ .

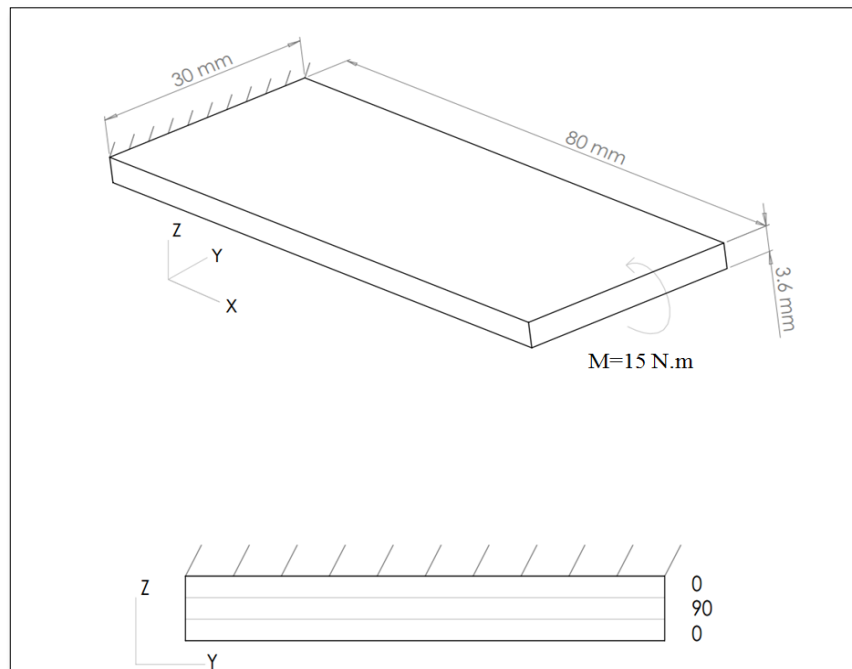


Figure 66 Plate model under bending moment

Edge distributed moment is applied at the free end of plate in order to simulate pure bending. 2-D plate model and applied boundary conditions are shown in Figure 67. In finite element pre-process model, 1600 shell elements are used.

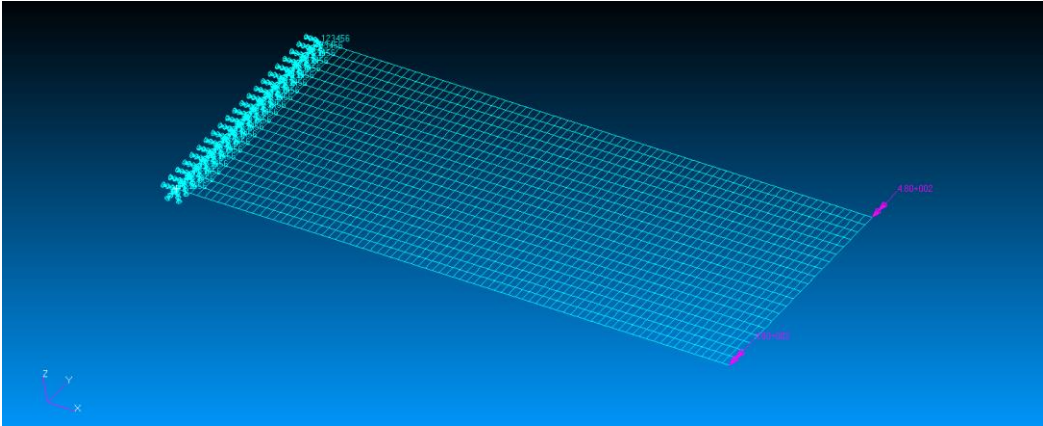


Figure 67 2D plate model and its boundary conditions

The maximum deflection is 3.13 mm at the free edge. Due to the symmetric laminate and pure bending conditions, maximum stresses occurs top and bottom layers and they are 229.47 MPa. Note that, the top layer is exposed to compressive stress while the bottom layer is exposed to tensile stress. The output of Matlab code is given in Table 14.

Table 14 Results of code for a single step

	<b>Maximum Deflection (mm)</b>	<b><math>\sigma_{max,x}</math> [MPa]</b>	<b><math>\sigma_{max,y}</math> [MPa]</b>
Matlab® Code Output	3.26	239.47	12.03

### 5.6.2.3 Analytical Solution

The stress strain relation of orthotropic materials is expressed in Eq. 39.

$$\begin{aligned} \begin{Bmatrix} \sigma_x \\ \sigma_y \\ \sigma_{xy} \end{Bmatrix}_k &= \begin{bmatrix} \bar{Q}_{11} & \bar{Q}_{12} & 0 \\ \bar{Q}_{12} & \bar{Q}_{22} & 0 \\ 0 & 0 & \bar{Q}_{66} \end{bmatrix}_k \begin{Bmatrix} \epsilon_x \\ \epsilon_y \\ \epsilon_{xy} \end{Bmatrix}_k \\ &= \begin{bmatrix} \bar{Q}_{11} & \bar{Q}_{12} & 0 \\ \bar{Q}_{12} & \bar{Q}_{22} & 0 \\ 0 & 0 & \bar{Q}_{66} \end{bmatrix}_k \left\{ \begin{Bmatrix} \epsilon_x^0 \\ \epsilon_y^0 \\ \epsilon_{xy}^0 \end{Bmatrix} + z \begin{Bmatrix} \kappa_x \\ \kappa_y \\ \kappa_{xy} \end{Bmatrix} \right\} \end{aligned} \quad (39)$$

In order to obtain the layer stresses, transformed reduced stiffness matrix has to be calculated. Transformed reduced stiffness matrices of  $0^\circ$  and  $90^\circ$  layers are shown in Eq. 40 and Eq. 41 respectively.  $\bar{Q}_{16}$  and  $\bar{Q}_{26}$  terms are 0 since the material is orthotropic.

$$[\bar{Q}]_{0^\circ} = \begin{bmatrix} 131.27 & 6.91 & 0 \\ 6.91 & 2.21 & 0 \\ 0 & 0 & 4.95 \end{bmatrix} \times 10^3 \text{ (MPa)} \quad (40)$$

$$[\bar{Q}]_{90^\circ} = \begin{bmatrix} 2.21 & 6.91 & 0 \\ 6.91 & 131.27 & 0 \\ 0 & 0 & 4.95 \end{bmatrix} \times 10^3 \text{ (MPa)} \quad (41)$$

Resultant force and moments can be written with respect to extensional strains and curvatures and they are expressed in Eq. 42.

$$\begin{bmatrix} N \\ M \end{bmatrix} = \begin{bmatrix} A & B \\ B & D \end{bmatrix} \begin{bmatrix} \epsilon^0 \\ \kappa \end{bmatrix} \quad (42)$$

Extensional stiffness matrix, [A], is shown in Eq. 43.

$$[A] = \begin{bmatrix} 323.4 & 7.96 & 0 \\ 7.96 & 174.20 & 0 \\ 0 & 0 & 17.83 \end{bmatrix} \times 10^3 \text{ (N/mm)} \quad (43)$$

Bending stiffness matrix of laminate denoted as  $[D]$  is given in Eq. 44.

$$[D] = \begin{bmatrix} 492.6 & 8.60 & 0 \\ 8.60 & 44.78 & 0 \\ 0 & 0 & 19.26 \end{bmatrix} \times 10^3 (N/mm^3) \quad (44)$$

Due to the symmetric lay-up, matrix  $[B]$  called coupled stiffness matrix is zero. Also, since there is only bending moment exerted on plate,  $N_x$ ,  $N_y$ ,  $N_{xy}$ ,  $M_y$  and  $M_{xy}$  terms are zero. Then, curvatures due to pure bending are expressed in Eq. 45.

$$\begin{Bmatrix} \kappa_x \\ \kappa_y \\ \kappa_{xy} \end{Bmatrix} = [D]^{-1} \begin{Bmatrix} M_1 \\ 0 \\ 0 \end{Bmatrix} \quad (45)$$

The inverse of bending stiffness matrix is given Eq. 45.

$$[D]^{-1} = \begin{bmatrix} 2.04 & -0.39 & 0 \\ -0.39 & 22.41 & 0 \\ 0 & 0 & 51.92 \end{bmatrix} \times 10^{-6} (mm^3/N) \quad (46)$$

Then, curvatures are:

$$\begin{Bmatrix} \kappa_x \\ \kappa_y \\ \kappa_{xy} \end{Bmatrix} = \begin{Bmatrix} -0.102 \\ 0.0196 \\ 0 \end{Bmatrix} \times 10^{-3} (1/mm) \quad (47)$$

Then, stresses of  $0^\circ$  layers are given in Eq. 48.

$$\begin{Bmatrix} \sigma_x \\ \sigma_y \\ \sigma_{xy} \end{Bmatrix}_{0^\circ} = \begin{Bmatrix} -132.50 z \\ -6.61 z \\ 0 \end{Bmatrix} MPa \quad (48)$$

And, stresses of 90° layers are given in Eq. 49.

$$\begin{Bmatrix} \sigma_x \\ \sigma_y \\ \sigma_{xy} \end{Bmatrix}_{90^\circ} = \begin{Bmatrix} -0.90 z \\ 18.65 z \\ 0 \end{Bmatrix} MPa \quad (49)$$

Maximum stress acting on plate occurs at top and bottom surfaces of 0° layers. At top surface, plate is under compression and at bottom surface, it is under tension. So the maximum stresses occurs at  $z=1.8$  mm and  $z=-1.8$  mm.

$$\begin{Bmatrix} \sigma_x \\ \sigma_y \\ \sigma_{xy} \end{Bmatrix}_{top, z=1.8 \text{ mm}} = \begin{Bmatrix} -238.50 \\ -11.91 \\ 0 \end{Bmatrix} (MPa) \quad (50)$$

$$\begin{Bmatrix} \sigma_x \\ \sigma_y \\ \sigma_{xy} \end{Bmatrix}_{bottom, z=-1.8 \text{ mm}} = \begin{Bmatrix} 238.5 \\ 11.91 \\ 0 \end{Bmatrix} (MPa) \quad (51)$$

The deflection of fixed-free plate can be expressed in Eq. 52.

$$\omega^0(x, y) = -\frac{1}{2} (x^2 \kappa_x + y^2 \kappa_y + xy \kappa_{xy}) \quad (52)$$

The maximum deflection which occurs at the free edges of plate is expressed as:

$$\omega^0(x = 80 \text{ mm}, y) = 3.26 \text{ mm} \quad (53)$$

The results of analytical and finite element methods are given in Table 15.

Table 15 Comparison of analytical solution and code results

	Maximum Deflection [mm]	$\sigma_{\max, x}$ [MPa]	$\sigma_{\max, y}$ [MPa]
Matlab® Code Output	3.26	239.47	12.03
Analytical Solution	3.26	238.50	11.91

## 5.7 Results of Stacking Sequence

Control surface models which consist of 12 layers are examined. Due to the laminate symmetry, there are 6 layers to examine for each model. In ply orientation parametric study, 0,30,45,60 and 90 degree layers are used so, 15625 different analyses are carried out for each control surface during this study. The algorithm written in Matlab® modifies the input file in each step and runs Nastran® solver. After that, code calculates the maximum deflection and maximum plane stresses each directions and failure indices of Maximum Stress, Tsai-Wu, Tsai-Hill and Hoffman failure equations. Then, it prints the results to external file for each ply orientation. A sample of printed results of algorithm is shown in Table 16.

Table 16 A part of printed results of parametric study algorithm

TW Status	H Status	TH Status	M.S. Status	$\sigma_{x,max}$ (MPa)	$\sigma_{y,max}$ (MPa)	$\sigma_{xy,max}$ (MPa)	Maximum Deflection (mm)	L1 (°)	L2 (°)	L3 (°)	L4 (°)	L5 (°)	L6 (°)
1	1	0	1	677.39	21.32	26.86	4.603	30	0	0	45	45	30
1	1	0	1	682.33	22.26	26.92	4.605	30	0	0	45	45	45
1	1	0	1	684.91	22.54	26.88	4.600	30	0	0	45	45	60
1	1	0	1	685.45	21.49	26.87	4.584	30	0	0	45	45	90
1	1	1	1	673.04	20.66	26.35	4.543	30	0	0	45	60	0
1	1	0	1	685.03	22.71	26.69	4.593	30	0	0	45	60	30
1	1	0	1	690.25	24.81	26.75	4.596	30	0	0	45	60	45
1	1	0	1	693.29	26.22	26.72	4.592	30	0	0	45	60	60
1	1	0	1	694.14	25.69	26.69	4.577	30	0	0	45	60	90
0	0	0	1	681.07	27.62	26.63	4.526	30	0	0	45	90	0
0	0	0	1	691.59	29.16	26.94	4.575	30	0	0	45	90	30
0	0	0	1	696.92	30.54	26.93	4.573	30	0	0	45	90	45
0	0	0	1	700.39	31.98	26.86	4.568	30	0	0	45	90	60
0	0	0	1	702.50	33.57	26.99	4.567	30	0	0	45	90	90
1	1	1	1	629.29	17.79	24.42	4.220	30	0	0	60	0	0
1	1	1	1	635.60	18.65	24.64	4.261	30	0	0	60	0	30
1	1	1	1	638.04	18.88	24.67	4.261	30	0	0	60	0	45
1	1	1	1	640.37	18.71	24.66	4.257	30	0	0	60	0	60
1	1	1	1	641.35	18.30	24.73	4.246	30	0	0	60	0	90

In Table 16, TW Status shows whether a ply orientation of the model fails or not under aerodynamic pressure loads with respect to Tsai-Wu failure criterion while H Status is the failure condition of a ply orientation with respect to Hoffman failure criterion. Also, TH Status denotes the failure condition of ply orientations with respect to Tsai-Hill and M.S. Status column indicate the failure status of ply orientations in terms of Maximum Stress failure criterion. In these columns, value of “1” shows that material with related ply orientation does not fail under aerodynamic loads and “0” values Show that failure occurs. Moreover, algorithm reads all data in

output file of each analysis and it prints maximum plane stresses in x, y, and xy directions and maximum total deformation of related stacking sequence. Finally, it prints ply orientations layer by layer. “L1” values show the layer orientation of bottom layer of control surfaces. Due to the symmetric lay-up it is also layer orientation of top layer. “L6” indicates the orientation of mid-layers so layer orientations is expressed that [L1/L2/L3/L4/L5/L6]<sub>s</sub>. In Figure 68, representation of ply orientation is shown on the semi-cross-section of model-1.

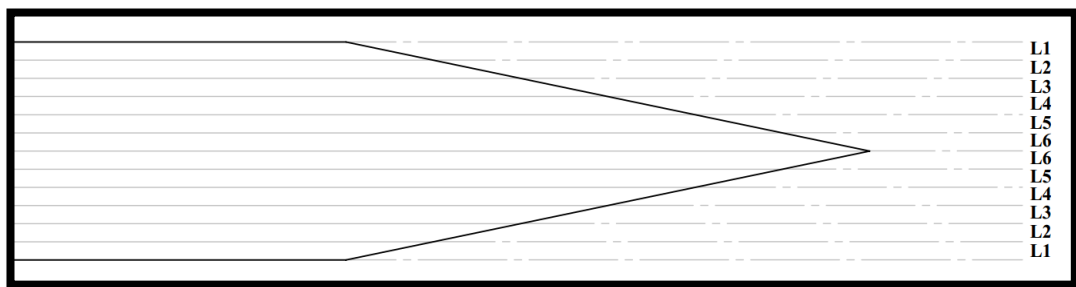


Figure 68 Representation of ply orientation

According to the results the least deflected ply orientation for both control surface model is [0°/0°/0°/0°/0°/90°]<sub>s</sub> in terms of the tip deflection value. It passes from all failure test including Tsai-Wu, Hoffman, Tsai-Hill and Maximum Stress. The stress values and maximum total deformation occurring at the tip is given in the Table 17.

Table 17 In-plane stresses and maximum tip deflection of least deflected ply orientations

<b>Control Surface Model</b>	<b>Ply Orientation</b>	<b><math>\sigma_{x,max}</math> [MPa]</b>	<b><math>\sigma_{y,max}</math> [MPa]</b>	<b><math>\sigma_{xy,max}</math> [MPa]</b>	<b>Maximum Total Deflection [mm]</b>
Model-1	[0°/0°/0°/0°/0°/90°] <sub>s</sub>	369.62	6.16	8.42	2.725
Model-2	[0°/0°/0°/0°/0°/90°] <sub>s</sub>	437.62	7.42	8.44	3.484

842 of 15625 ply orientations passed from all failure tests for control surface of model-1 while the amount of ply orientation not fail is 342 for control surface of model-2.

According to the parametric study results of control surface of model-1, there are 4140 different stacking sequences passed from Maximum Stress failure criteria. Also, 1249 different ply orientations pass from the failure test in terms of Tsai-Wu failure criterion. This value is 1108 for Hoffman failure criterion and 842 for Tsai-Hill failure theory. In Figure 69, the amount of ply orientations passed from failure tests is shown.

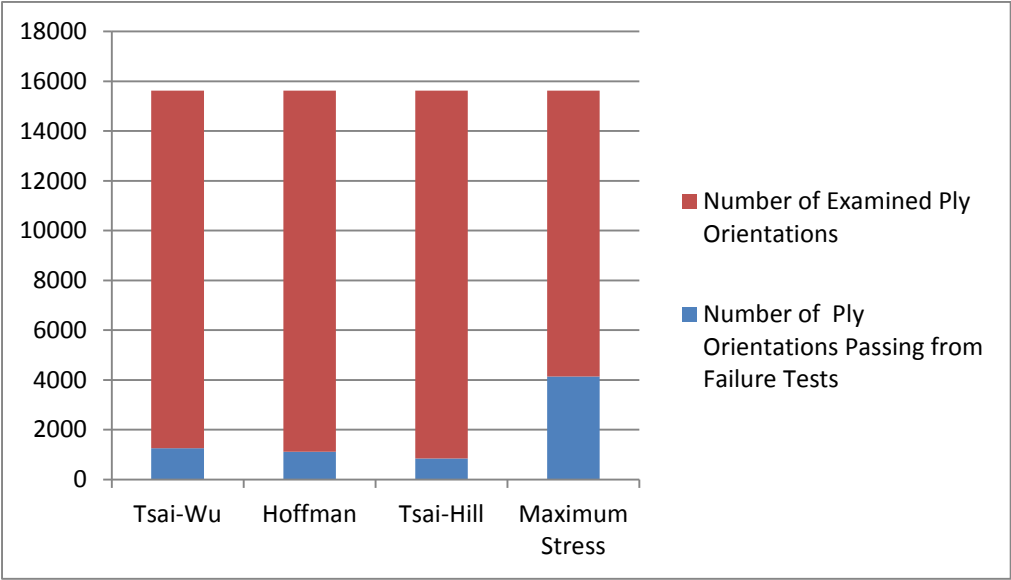


Figure 69 Amount of ply orientations passed from failure tests for control surface of model-1

As it is seen in Figure 69, the most conservative failure criterion is Tsai-Hill and the less conservative is Maximum Stress failure criterion in terms of the number of failed ply orientations for the control surface of model-1.

According to the parametric study results of control surface of model-2, there are 2796 different stacking sequences passed from Maximum Stress failure criteria. Also, 479 different ply orientations pass from the failure test in terms of Tsai-Wu failure criterion. This value is 425 for Hoffman failure criterion and 342 for Tsai-Hill failure theory.

In Figure 70, the amount of ply orientations passed from failure tests is shown.

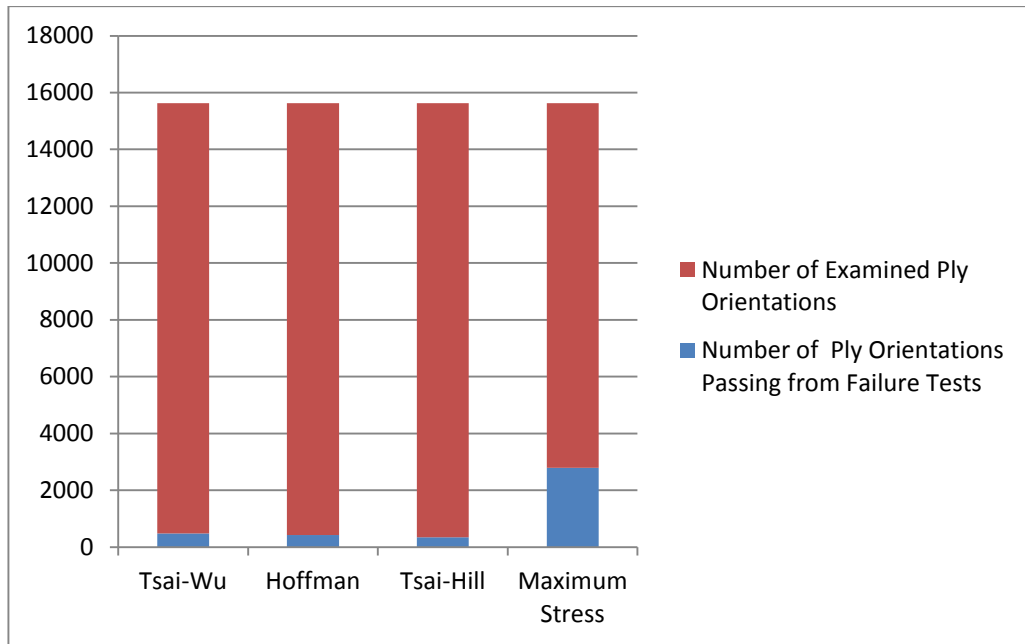


Figure 70 Amount of ply orientations passed from failure tests for control surface of model-2

As it is seen in Figure 70, the most conservative failure criterion is Tsai-Hill and the less conservative is Maximum Stress failure criterion in terms of the number of failed ply orientations for the control surface of model-2.

The less deformable 20 stacking sequence of control surface of model-1 is given in Table 18. These orientations do not fail in terms of all failure tests used in this study.

Table 18 Least deformable 20 stacking sequence of control surface of model-1

<b>Ply Orientation</b>	<b><math>\sigma_{x,max}</math> [MPa]</b>	<b><math>\sigma_{y,max}</math> [MPa]</b>	<b><math>\sigma_{xy,max}</math> [MPa]</b>	<b>Maximum Total Deflection [mm]</b>
$[0^\circ/0^\circ/0^\circ/0^\circ/0^\circ/90^\circ]_s$	369.62	6.16	8.42	2.725
$[0^\circ/0^\circ/0^\circ/0^\circ/0^\circ/0^\circ]_s$	365.39	5.79	9.35	2.725
$[0^\circ/0^\circ/0^\circ/0^\circ/0^\circ/60^\circ]_s$	368.76	5.33	8.46	2.730
$[0^\circ/0^\circ/0^\circ/0^\circ/0^\circ/45^\circ]_s$	368.37	5.49	8.48	2.734
$[0^\circ/0^\circ/0^\circ/0^\circ/0^\circ/30^\circ]_s$	367.82	5.80	8.63	2.738
$[0^\circ/0^\circ/0^\circ/0^\circ/60^\circ/0^\circ]_s$	383.07	9.07	8.32	2.818
$[0^\circ/0^\circ/0^\circ/0^\circ/60^\circ/90^\circ]_s$	388.94	10.91	8.15	2.820
$[0^\circ/0^\circ/0^\circ/0^\circ/45^\circ/90^\circ]_s$	388.48	11.34	9.06	2.820
$[0^\circ/0^\circ/0^\circ/0^\circ/90^\circ/0^\circ]_s$	385.20	10.81	8.51	2.820
$[0^\circ/0^\circ/0^\circ/0^\circ/45^\circ/0^\circ]_s$	382.79	6.94	8.61	2.821
$[0^\circ/0^\circ/0^\circ/0^\circ/30^\circ/90^\circ]_s$	386.82	11.97	9.46	2.824
$[0^\circ/0^\circ/0^\circ/0^\circ/30^\circ/0^\circ]_s$	381.37	6.27	9.12	2.825
$[0^\circ/0^\circ/0^\circ/0^\circ/90^\circ/60^\circ]_s$	390.23	12.13	8.21	2.826
$[0^\circ/0^\circ/0^\circ/0^\circ/90^\circ/45^\circ]_s$	389.54	11.79	8.18	2.828
$[0^\circ/0^\circ/0^\circ/0^\circ/90^\circ/90^\circ]_s$	391.23	12.48	8.48	2.829
$[0^\circ/0^\circ/0^\circ/0^\circ/60^\circ/60^\circ]_s$	389.00	11.07	8.25	2.829
$[0^\circ/0^\circ/0^\circ/0^\circ/45^\circ/60^\circ]_s$	388.53	9.11	9.06	2.831
$[0^\circ/0^\circ/0^\circ/0^\circ/60^\circ/45^\circ]_s$	388.26	10.64	8.21	2.831
$[0^\circ/0^\circ/0^\circ/0^\circ/30^\circ/60^\circ]_s$	386.56	9.24	9.08	2.832
$[0^\circ/0^\circ/0^\circ/0^\circ/60^\circ/30^\circ]_s$	386.94	9.93	8.26	2.833

Moreover, the least deformable 20 stacking sequence of control surface of model-2 is given in Table 19. These orientations do not fail in terms of all failure tests used in this study.

Table 19 Least deformable 20 stacking sequence of control surface of model-2

<b>Ply Orientation</b>	<b><math>\sigma_{x,max}</math> [MPa]</b>	<b><math>\sigma_{y,max}</math> [MPa]</b>	<b><math>\sigma_{xy,max}</math> [MPa]</b>	<b>Maximum Total Deflection [mm]</b>
$[0^\circ/0^\circ/0^\circ/0^\circ/0^\circ/90^\circ]_s$	437.62	7.42	8.44	3.484
$[0^\circ/0^\circ/0^\circ/0^\circ/0^\circ/0^\circ]_s$	431.88	6.99	8.59	3.486
$[0^\circ/0^\circ/0^\circ/0^\circ/0^\circ/60^\circ]_s$	436.92	6.38	8.36	3.504
$[0^\circ/0^\circ/0^\circ/0^\circ/0^\circ/45^\circ]_s$	436.44	6.37	8.36	3.514
$[0^\circ/0^\circ/0^\circ/0^\circ/0^\circ/30^\circ]_s$	435.38	6.36	8.48	3.518
$[0^\circ/0^\circ/0^\circ/0^\circ/90^\circ/0^\circ]_s$	461.87	13.30	8.65	3.646
$[0^\circ/0^\circ/0^\circ/0^\circ/90^\circ/90^\circ]_s$	469.46	15.17	8.75	3.665
$[0^\circ/0^\circ/0^\circ/0^\circ/90^\circ/60^\circ]_s$	468.57	14.86	8.48	3.665
$[0^\circ/0^\circ/0^\circ/0^\circ/90^\circ/45^\circ]_s$	467.70	14.54	8.54	3.670
$[0^\circ/0^\circ/0^\circ/0^\circ/60^\circ/0^\circ]_s$	460.11	11.48	8.65	3.672
$[0^\circ/0^\circ/0^\circ/0^\circ/90^\circ/30^\circ]_s$	466.19	14.14	8.74	3.676
$[0^\circ/0^\circ/0^\circ/0^\circ/60^\circ/90^\circ]_s$	467.53	13.28	8.96	3.677
$[0^\circ/0^\circ/0^\circ/0^\circ/30^\circ/90^\circ]_s$	461.15	14.45	11.07	3.682
$[0^\circ/0^\circ/0^\circ/0^\circ/45^\circ/90^\circ]_s$	466.16	13.58	10.92	3.683
$[0^\circ/0^\circ/0^\circ/0^\circ/45^\circ/0^\circ]_s$	459.03	9.19	10.23	3.686
$[0^\circ/0^\circ/0^\circ/0^\circ/30^\circ/0^\circ]_s$	454.35	8.03	10.62	3.687
$[0^\circ/0^\circ/0^\circ/0^\circ/60^\circ/60^\circ]_s$	467.75	13.63	8.71	3.699
$[0^\circ/0^\circ/0^\circ/0^\circ/60^\circ/45^\circ]_s$	466.83	13.27	8.71	3.703
$[0^\circ/0^\circ/0^\circ/0^\circ/30^\circ/60^\circ]_s$	461.09	11.22	10.55	3.704
$[0^\circ/0^\circ/0^\circ/0^\circ/60^\circ/30^\circ]_s$	464.96	12.63	8.82	3.704

According to Table 18 and 19,  $0^\circ$  layers are transcend in all orientations since lift force causing bending is dominant in aerodynamic forces. At the first five columns stacking sequences are identical for both control surface models. In all orientations, there are four  $0^\circ$  layers at the top and bottom layers. It is recommended that,  $90^\circ$  should be used at the mid-layers which are close to mid-plane of the laminate since control surfaces are not exposed to pure bending. In other words,  $90^\circ$  layer orientations are used at the mid-layers due to their closeness to the neutral axis because lift force due to aerodynamic pressure causes bending and torsion in both fiber and matrix direction. Bending moment due to the maximum aerodynamic pressure occurs at  $15^\circ$  angle of attack is much higher than torsion due to aerodynamic pressure occurs at  $15^\circ$  angle of attack so,  $0^\circ$  layers are dominant in ply orientations. Also, normal stresses in fiber direction are much higher than normal

stress in transverse direction and shear stresses. Least stress in fiber direction is obtained at the  $[0^\circ/0^\circ/0^\circ/0^\circ/0^\circ/0^\circ]_s$  orientation for both control surface model.

This parametric study is performed in order to improve a methodology for laminated composite control surfaces. As expected,  $0^\circ$  layers predominate at ply orientations of both control surface models which cause less tip deflection. Since the bending moment due to aerodynamic pressure is much higher than the torsion due to aerodynamic pressure,  $0^\circ$  layers are needed in order to decrease tip deflection and stresses in fiber direction. However, due to existence of a fair amount of torsion, non-zero degree layers are needed especially at the layers close to neutral axis of the structure. For these reasons,  $90^\circ$  layers used in mid-layers cause the reduction of tip deflection of control surfaces.

Moreover, if deflection results of control surface of model-1 are considered with four decimal points, an analyzer will see that using  $90^\circ$  layers at mid-layers causes less tip deflection than  $0^\circ$  layers.

## **5.8 Loading Test**

In order to verify parametric study results a serial set of loading test is performed. Laminated control surfaces with least deflected and randomly chosen two different stacking sequences were manufactured and tested to compare the test and FEM results in terms of the tip deflection of the control surface models. These three stacking sequences including least deformable orientations are the orientations that passed from all four failure criteria used in parametric study part of the thesis and they are listed in Table 20 with their maximum total deformation values.

Table 20 Total deformation with FEM of selected configuration

Test Model	Stacking Sequence	Maximum Total Deformation of Control Surface of Model-1 [mm]	Maximum Total Deformation of Control Surface of Model-2 [mm]
A	$[0^\circ/0^\circ/0^\circ/0^\circ/0^\circ/90^\circ]_s$	2.725	3.484
B	$[45^\circ/0^\circ/0^\circ/0^\circ/90^\circ/0^\circ]_s$	3.973	4.821
C	$[30^\circ/0^\circ/0^\circ/30^\circ/0^\circ/30^\circ]_s$	4.255	5.305

During the manufacturing process, prepreg compression moulding method was used. In this method, CE 1007/310/37 prepreps were cut in ply cutter layer by layer in order to lay layers into closed mould. Mould having two symmetric parts, is manufactured with machining process. The manufactured mould of control surfaces is shown in Figure 71.



Figure 71 Mould of control surfaces

After this operation, mould was put into non-pressurized oven for curing process. In this process, mould was heated up to 120 °C and it was leaved to cooling at the room temperature. After that, initial products were subtracted from mould for trimming process. Initial products without trimming are shown in Figure 72.

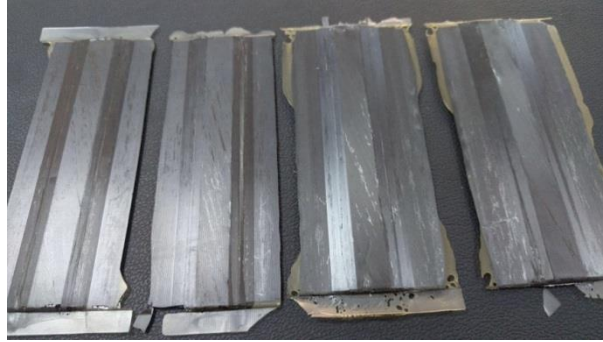


Figure 72 Initial products without trimming

Then, after trimming and surface finishing operation manufacturing process of control surfaces were completed. They are shown in Figure 73.

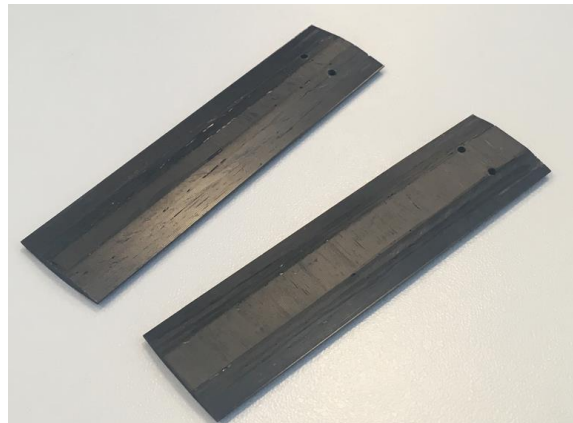


Figure 73 Final product of control surfaces

The dimensions of manufactured control surfaces are larger than the FEM models in order to connect them with the test interfaces. Measured dimensions of a sample of final product are shown in Figure 74.



Figure 74 Length of a control surface sample

In testing part, control surfaces were connected to test interface with bolts and nuts. The aim of testing the control surfaces is to get deflection values under aerodynamic loading. Test setup is shown in Figure 75.

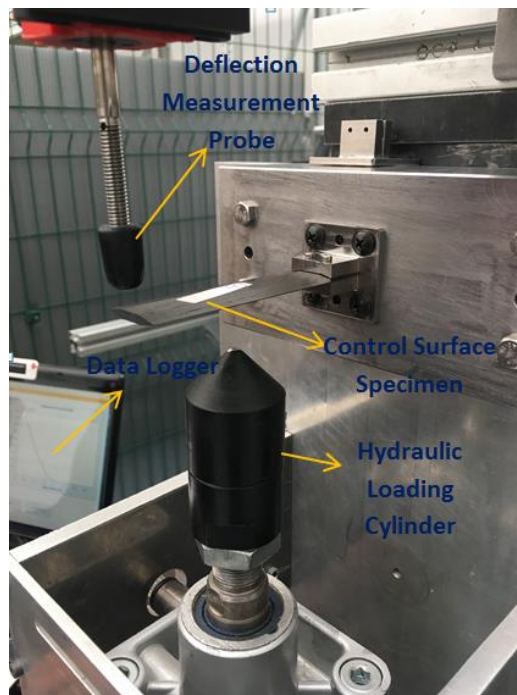


Figure 75 Loading test setup

Test setup is composed of three main parts which are deflection measurement probe, hydraulic loading part and data logger. Deflection measurement probe is responsible for measuring deflection data and it has 0.05 mm measurement sensitivity. Hydraulic loading section applies to point load to the test specimen and data logger part is responsible for gathering and saving the force and displacement data.

During the test aerodynamic lift force is applied to the pressure centers of control surfaces. Applied loads and load application points which are pressure centers of control surface models are given in Table 21.

Table 21 Test inputs of control surface models

	<b>Control Surface of Model-1</b>	<b>Control Surface of Model-2</b>
Test Load (N)	366.4	356.2
Load Application Distance From Leading Edge (mm)	11.8	11.3
Load Application Distance From Tip (mm)	38.3	38.6

The comparison of test and FEM analyses is shown in Table 22 for both control surface models.

Table 22 Comparison of FEM and test results

Test Model	Maximum Total Deformation of Control Surface of Model-1 [mm]			Maximum Total Deformation of Control Surface of Model-2 [mm]		
	FEM Results	Test Results	% Error	FEM Results	Test Results	% Error
A	2.725	2.950	7.627	3.484	3.650	4.548
B	3.973	4.300	7.605	4.821	5.200	7.288
C	4.255	4.450	4.382	5.305	5.550	4.414

According to the test results there are small amount of differences between FEM and test results. The main reason of these differences is manufacturing tolerances. Another one is load application method. In FEM analyses, pressure distributions of each control surface model are applied. On the other hand, during the test, point load is applied to the center of pressure. If point load is applied to FEM model, very high stress values occurs at the application node of the FEM due to stress concentration so failure analyses may give wrong results. All of these are the possible differences between FEM and test results.

In this study, two different control surface models with modified double wedge cross-section are compared in some ways. First of all, least deflected ply orientations of both control surface models are the same which is  $[0^\circ/0^\circ/0^\circ/0^\circ/0^\circ/90^\circ]_s$ . However, control surfaces of model-1 are less deflected under maximum aerodynamic loading in comparison to control surfaces of model-2 due to the their geometries. Although control surfaces of model-2 are lighter than control surfaces of model-1, control surfaces of model-1 are more preferable due to their higher safety factor and lower deflection values under maximum aerodynamic loading. The comparison of both control surface models are given in Table 23.

Table 23 Comparison of control surface models

<b>Control Surface Models</b>	<b>Least Deflected Stacking Sequence w.r.t. Maximum Tip Deflection</b>	<b>Maximum Tip Deflection Under Maximum Aerodynamic Loading [mm]</b>	<b>Weight [g]</b>
<b>Model-1</b>	[0°/0°/0°/0°/0°/90°] <sub>s</sub>	2.725	9.12
<b>Model-2</b>	[0°/0°/0°/0°/0°/90°] <sub>s</sub>	3.484	7.78

## CHAPTER 6

### CONCLUSION AND FUTURE WORKS

In this thesis, laminated composite missile fins or control surfaces of a surface-to-surface missile model are investigated in terms of static aeroelastic response under constant supersonic flight conditions. With respect to their cross-sections by performing a serial set of one-way static aeroelastic analyses, two different modified double wedge fins or control surfaces using for control actuation system of a missile are investigated and compared in terms of aerodynamic and linear structural characteristics in order to minimize tip deflection.

A serial set of steady-state supersonic CFD analyses at different angle of attack are conducted in order to obtain pressure distribution causing the structural deflection or failure on fins having modified double-wedge cross-sections. Grid refinement study is also performed for CFD analysis part.

Control surface models are manufactured and tested in supersonic wind tunnel at  $0^\circ$  angle of attack and constant Mach number which is 1.6 Mach, in order to observe shock waves on control surfaces during the flight. Shock wave angles obtained from test, CFD results and analytical solution of oblique shock wave theory are compared. Lift and drag coefficients are obtained part-by-part for both missile models with different control surfaces. Also, normal and axial forces acting on missile parts are obtained and a comparison study is performed for both control surface models.

By using aerodynamic loads due to pressure distribution on fins, a set of linear structural analyses with an algorithm written in Matlab® are executed in Nastran®.

This algorithm changes the layer orientation in each step and investigates the stacking sequence of the laminated composite control surfaces with respect to tip deflection by considering four different failure criteria. Also, case verification study is performed in order to check whether the algorithm reads and writes correct data or not. Three structures with least deflected stacking sequences and not fail under maximum aerodynamic loads in structural analyses are manufactured and tested for both control surface models in order to compare and verify the maximum tip deflection results of Finite Element Method. Based on these analyses and tests, some conclusions and recommendations for a designer are obtained.

First of all, CFD analyses are performed for both missile model with different control surfaces at different angle of attack and they are repeated for finer grid. The results of fine of coarse grid are very close to each other and it can be said that solutions are converged in terms of mesh refinement study. Also, Missile models have same nose, body and fixed wing geometries so free-stream is the same until it reaches the control surfaces. As a result of these, nose and fixed wings have nearly same drag and lift coefficients for both missile models. Although these coefficients of body parts are close to each other, there are some differences due to the control surfaces of missile which are located at the back. Maximum pressure distribution occurs on control surfaces are also acquired at  $15^\circ$  angle of attack analyses to use it in structural part of the study. Then, normal and axial forces are obtained part by part in order to compare the missile models. The reason of getting normal and axial forces is to implement them to the structural model.

Secondly, supersonic wind tunnel testing is carried out at  $0^\circ$  angle of attack in order to observe shock waves on control surfaces. Shock wave angle comparison study is also performed during this study. Test, CFD result and analytical solution of shock wave theory are compared in terms of the oblique shock wave angles. There are some differences between shock wave angle results. The difference between test and analytical solution may be due to the manufactural tolerances. Wedge angle tolerance of the test specimens can cause measurement error.

In structural analysis part of the study, parametric study of stacking sequence or ply orientation is performed. In order to conduct this stage, an algorithm which can easily modify the input file of Nastran® is written in Matlab® for both control surface models. This algorithm changes the fiber angle of layers in each step and it calculates the maximum tip deflection of control surfaces. Also, it checks whether all ply orientations fail or not under maximum pressure distribution in terms of the four different failure criteria which are Tsai-Wu, Tsai-Hill, and Hoffman and Maximum Stress failure theories. Then, the algorithm prints the in-plane stresses, maximum total deformation and failure status of control surfaces to the external file. Moreover, this parametric study is performed in order to improve a methodology for laminated composite control surfaces. The algorithm created for this parametric study can be used in different loading cases of control surface models. According to the parametric study results, 0° layers predominate at ply orientations of both control surface models which cause less tip deflection as expected. Since bending moment due to maximum aerodynamic pressure occurs at 15° angle of attack is greater than torsion acting on the control surfaces, 0° layers are dominant at the stacking sequences causing less tip deflection. However, due to the existence of torsion on the control surfaces, 90° layers are also obtained at mid-layers, nearest layers of neutral axis. This causes a reduction of tip deflection due to torsion. Moreover, Tsai-Hill is most conservative and Maximum Stress is less conservative failure theories in terms of the passed orientation number from failure tests. According to the failure test part of the study, most conservative failure criterion is Tsai-Hill, and least one is Maximum Stress failure criteria in terms of passed ply orientation numbers.

Finally, the randomly selected three control surface configurations for each model are manufactured and tested. Although test results are close to FEM results, there are some differences between them. The main reason of these differences is manufacturing tolerances. Composite manufacturing is difficult process because the product dimensions depends upon many different parameters such as mould tolerances, layer tolerances and curing process.

Also, due to the usage of unidirectional layers, some defects on the control surfaces when extracting them from the mould. In order to avoid from this, surface film or woven fabric should be used at the outer layers. As a result of structural analysis part, control surfaces of model-1 are less deflected under maximum aerodynamic loading in comparison to control surfaces of model-2. Although control surfaces of model-2 have lightweight, control surfaces of model-1 are more preferable due to their higher safety factor and lower deflection values under maximum aerodynamic loading.

In future works, shape optimization study will be performed for control surfaces instead of using generic models. Parametric study of stacking sequence will be repeated with shape optimization study. Moreover, effect of aerodynamic heating on composite material will be examined by modeling whole flight scenario instead of using the constant free-stream velocity boundary condition.

## REFERENCES

- [1] Nielsen, J. N., “*Missile Aerodynamics*”, Vidya, Inc., Stanford Industrial Park, Palo Alto, California, 1960
- [2] Fleeman, E. L., “*Tactical Missile Design*”, AIAA Education Series, 2001
- [3] *Javelin Medium Anti-armor Weapon System*. (2018, February 15). Retrieved from <http://www.inetres.com>
- [4] Kayabaşı İ., “*Numerical Investigation of Characteristics of Pitch and Roll Damping Coefficients for Missile Models*”, METU M. Sc. Thesis, 2012.
- [5] Bisplinghoff R. L., Ashley H., and Halfman R. L., “*Aeroelasticity*, Courier Corporation, 2013.
- [6] R. M. Jones, “*Mechanics of Composite Materials*”, 2nd Ed., Taylor and Francis Inc., Philadelphia, 1999.
- [7] Dietz, A.G.H., “*Composite Materials*”, Philadelphia, 1965.
- [8] Laszlo P. K. and George S. S., *Mechanics of Composite Structures*, Vol. 1, 2003.
- [9] Yang, Y. "Structural analysis and multidisciplinary design of flexible fluid loaded composite canard". Retrospective Thesis and Dissertations, 2005.
- [10] Kim C.W., Hwang W., Park H.C. and Han K.S. “*Stacking Sequence Optimization of Laminated Plates*”, *Composite Structures* Vol. 39, pp. 283-288, 1998.
- [11] Lopez R.H., Laursen M.A. and Cursi E., “*Optimization of Laminated Composite Plates Considering Different Failure Criteria*”, *International Committee on Composite Materials*, Vol. 31, No.3, July 2009.
- [12] Harrison P. N., Johnson E.R., “*A Mixed Variational Formulation for Interlaminar Stresses in Thickness-Tapered Composite Laminates*”, *International Journal of Solid Structures* Vol. 33, pp. 2377-2399, 1996.

- [13] Rajanish M., Nanjundaradhya N. V., Sharma R. S. and Pal B., “*A Review of Failure of Composite Materials*”, International Journal of Engineering Research and Application, Vol. 3, pp. 122-124, April 2013.
- [14] Burk, R., C., “*Standard Failure Criteria Needed for Advanced Composites*”, AIAA, Vol. 21, pp. 58-62, 1983.
- [15] Sun C.T., Quin B.J., Tao J, Oplinger D.W. and Hughes W.J., “*Comparative evaluation of failure analysis methods for composite laminates*”, Federal Aviation Administration Report, May 1996.
- [16] Olcay Y., “*Progressive Failure Analysis of Composite Shells*”, METU M. Sc. Thesis, 2012.
- [17] Celik O., “*Failure Analysis of Tapered Composite Structures Under Tensile Loading*”, METU M. Sc. Thesis, 2016.
- [18] Akbulut M., Sonmez F.O., “*Design Optimization of Laminated Composites Using a New Variant of Simulated Annealing*”, International Journal of Computers and Structures, 2011.
- [19] Lee H.J., “*CFD Performance of Turbulence Models for Flow from Supersonic Nozzle Exhausts*”, Washington University M. Sc. Thesis, 2017.
- [20] Sumer B., “*Fluid Structure Coupled Analysis of an Aerodynamic Surface*”, METU M. Sc. Thesis, 2004.
- [21] Newman J.C., Newman P.A., Taylor A.C., Houc G.J.W., “*Efficient Nonlinear Static Aeroelastic Wing Analysis*”, Journal of Computer and Fluids, Vol. 28, pp. 615-628, June 1999.
- [22] Inci H., “*Discrete Fiber Angle and Continuous Fiber Path Optimization in Composite Structures*”, METU M. Sc. Thesis, 2012.
- [23] Dillinger J.K.S., “*Static Aeroelastic Optimization of Composite Wings with Variable Stiffness Laminates*”, Technische Universiteit Delft Ph. D. Thesis, 2012.
- [24] Ozkaya O., Kayran A., “*Nonlinear Static Aeroelastic Behavior of Composite Missile Fin with interlaminar and Intralaminar Damage*”, AIAA Structures, Structural Dynamics and Materials Conference, January 2018.

- [25] Aslan G.M., Kurtuluş D.F., Kırımlioğlu S., “*Aeroelastic Modelling and Testing of a Thin Laminated Composite Missile Fin/Wing*” 18th AIAA/ISSMO Multidisciplinary Analysis and Optimization Conference. Denver, Colorado, June 2017.
- [26] Daniel, I. M., Ishai, O. “*Engineering Mechanics of Composite Materials*”, 2nd ed. Oxford University Press, pp. 324, New York, 2005.
- [27] Falzon B.G., Apruzzese P., “*Numerical Analysis of Intralaminar Failure Mechanism in Composite Structures. Part I: FE Implementation*”, Journal of Composite Structures, Vol.93, pp. 1039-1046, January 2011.
- [28] Camancho P.P., “*Failure Criteria for Fibre-Reinforced Polymer Composites*” Universidade do Porto, 2002.
- [29] Hill R., “*The Mathematical Theory of Plasticity*”, Oxford University Press Inc., 1950.
- [30] Tsai W.S., “*Strength Characteristics of Composite Materials*”, National Aeronautics and Space Administration Report, April 1965.
- [31] Yeh H.Y., Murphy H.C., “*An Investigation of Failure Criterion for New Orthotropic Ceramic Matrix Composite Materials*”, Journal of Reinforced Plastics and Composites, Vol. 28, pp. 441-459, 2009.
- [32] Tsai W.S., Wu E.M., “*A General theory of Strength for Anisotropic Materials*”, Journal of Composite Materials, Vol. 5, pp. 58, January 1971
- [33] “*TGRID 3.6 User Guide*”, Fluent, Inc., 2004.
- [34] Salim M.S., Cheah S.C., “*Wall  $y^+$  Strategy for Dealing with Wall-bounded Turbulent Flows*”, International MultiConference of Engineering and Computer Scientists Vol. II, 2009.
- [35] “*Modeling Turbulent Flows with FLUENT*”, Dr. Aleksey Gerasimov, ANSYS Inc., October 2006.
- [36] Raymer D., “*Aircraft Design: A Conceptual Approach*”, Fifth Edition, vol. 134, no. 8. 2012.
- [37] Anderson J., “*Fundamentals of Aerodynamics*”, vol. Third Edit. 1985.
- [38] “*FLUENT User Guide*”, ANSYS Inc., 2009

- [39] Sutherland, W., "*The viscosity of gases and molecular force*", Philosophical Magazine, S. 5, 36, pp. 507-531., 1893.
- [40] "*FLUENT Theory Guide*", ANSYS Inc., 2009.
- [41] Agarwal B.D., Broutman L.J., Chandrashekhara K., "*Analysis and Performance of Fiber Composites*", 3<sup>rd</sup> Ed., Wiley India Pvt. Ltd., 2006.
- [42] Gibson R.F., "*Principle of Composite Material Mechanics*", McGraw-Hill Inc. 1994.
- [43] "*CE 1007/310/37 Technical Data Sheet*", SGL Group the Carbon Company
- [44] MSC Software, Nastran Quick Reference Guide, 2017.
- [45] Nettles A.T., "*Basic Mechanics of Laminated Composite Plates*", NASA Reference Publication, October 1994.
- [46] C. W. Bert, "*Classical Lamination Theory*," in Manual on Experimental Methods for Mechanical Testing of Composites, pp. 11–16, 1989.

## APPENDIX A

### NASTRAN FILE MODIFICATION

“.bdf” file is an input file of Nastran® that includes the model definition. It contains information about mesh model, material property, boundary conditions of analysis such as displacement, force, pressure etc. It is arranged by five main sections which are Nastran statement, file management section, executive control section and bulk data section. Nastran main section is used to arrange the system defaults and it is mostly not needed. File management section controls the database operations while executive control section gives some information about solution type, program modifications and system diagnostics. Then, requested outputs i.e. elements stress and strains, are written in case control section of the file and model definition, loadings and boundary conditions data is written in bulk data section. To better understand, a sample of Nastran input file is shown in Figure 76 [44].

```

ID TRUSS, SAMPLE
SOL 101
TIME 5
CEND
TITLE = SAMPLE INPUT FILE
SUBTITLE = TRUSS STRUCTURE
LOAD = 10
SPC = 11
DISP = ALL
ELFORCE = ALL
SPCFORCE = ALL
BEGIN BULK
$
$ GRID POINTS DESCRIBE THE GEOMETRY ← Comments start with a dollar sign
$
GRID 1 0. 0. 0.
GRID 2 0. 120. 0.
GRID 3 600. 120. 0.
GRID 4 600. 0. 0.
$
$ TRUSS MEMBERS MODELED WITH ROD ELEMENTS
$
CROD 1 21 2 3
CROD 2 21 2 4
CROD 3 21 1 3
CROD 4 21 1 4
CROD 5 21 3 4
$
PROD 21 22 4. 1.27
MAT1 22 30.E6 .3
FORCE 10 4 1000. 0. -1. 0.
SPC1 11 12 1 2
SPC1 11 3456 1 2 3 4
ENDDATA

```

Figure 76 Sample of Nastran® input file [44]

For the input file of control surfaces, ply orientations in bulk data section are changed. The bulk data section of the “.bdf” file of control surfaces is given in Figure 77. In bulk data section, there are six main cards of file which are CQUAD4, PCOMP, MAT8, PLOAD4, SPC1 and FORCE cards. In CQUAD4 card, quadratic elements are defined in terms of the element identification number, layer identification number, node number of elements and the ratio of theta angle and material coordinate identification. In PCOMP card, composite layers are identified in terms of their layer identification, thicknesses, orientation angles, requested outputs and lamination type. This card is important for this study because it is changed with the algorithms in order to parametrize layer orientations. MAT8 card defines the material properties and its identification number. Then, PLOAD4, SPC1 and FORCE cards identifies the boundary conditions of the input files which are pressure load, fixed support and point load respectively.

	Element ID	PCOMP ID	Node 1	Node 2	Node 3	Node 4	Theta/MC ID
CQUAD4	1	1	1	2	121	120	90.
CQUAD4	118	1	118	119	238	237	90.
CQUAD4	119	1	120	121	240	239	90.

	Ply ID	Z0	orientation angle	Output Request	Laminate type
PCOMP	3				SYM
	1	5.-5	0	YES	

Material Input								
	Material ID	E1	E2	v12	G12	G13	G23	Density
MAT8	1	126890.	6263.	0.32	3938.9	3938.9	2800.	1500.

Pressure Load Input	Load Set ID	Element Number	Pressure
PLOAD4	1	9439	-106000.
PLOAD4	1	9440	-106000.

Single Point Constraint	Constraint ID	Components of Global coordinate System	Element ID
SPC1	1	123456	1 THRU 119

	Force ID	Grid ID	Coordinate ID	Load Vector Scale Factor	X Component	Y Component	Z Component
FORCE	3	4594	0	36.	0.	0.	1.

Figure 77 Bulk data section of Nastran® input file

In order to form a better parametrization routine for Nastran, the format of the input and output files should be known well.

“.f06” file is a main output file of Nastran. It includes the information about constraint forces, displacements of each elements and element stresses. This file can be viewed and edited in any text editor. It also contains error messages to help user interpret the quality of analysis results.

Reading stress and deformation results correctly are very significant for the parametrization algorithm. An example of the output file of initial structural analysis is given in Figure 78. As it is seen in this figure, constraint forces, displacement vectors and element stresses are listed in the output file.

These parameters are used in the parametric study to check whether an element is failed or not and to obtain the maximum displacement of the control surfaces.

FORCES OF SINGLE-POINT CONSTRAINT							
POINT ID.	TYPE	T1	T2	T3	R1	R2	R3
30	G	-1.993723E+01	-2.542657E+01	3.645380E+00	-2.358236E-03	2.899111E-07	1.502463E-01
31	G	-1.318887E+01	-1.505539E+00	-2.256543E-01	-3.018425E-03	6.550987E-08	1.230279E-01
32	G	-9.337475E+00	-1.984685E-01	-5.225106E-01	-4.142455E-03	6.714308E-08	1.129930E-01
33	G	-7.916608E+00	6.958154E-01	-5.842092E-01	-3.795171E-03	6.946554E-08	1.185835E-01
34	G	-6.983613E+00	1.374005E+00	-6.379725E-01	-3.567692E-03	7.195311E-08	1.270493E-01

### a) Node Forces

DISPLACEMENT VECTOR							
POINT ID.	TYPE	T1	T2	T3	R1	R2	R3
1	G	2.856714E-06	3.506003E-05	-1.278941E-07	2.634539E-03	-2.948275E-04	-7.057120E-03
2	G	2.783152E-06	3.437891E-05	-1.279032E-07	2.946567E-03	-2.943726E-04	-7.033520E-03
3	G	2.709911E-06	3.362778E-05	-1.280082E-07	3.143691E-03	-2.937952E-04	-7.011696E-03
4	G	2.636953E-06	3.283044E-05	-1.283151E-07	3.302019E-03	-2.934359E-04	-6.987837E-03
5	G	2.564141E-06	3.199550E-05	-1.288913E-07	3.439271E-03	-2.934150E-04	-6.962026E-03

### b) Node Displacements

STRESSES IN LAYERED COMPOSITE ELEMENTS (QUAD4)										
ELEMENT ID	PLY ID	STRESSES IN FIBER AND MATRIX DIRECTIONS			INTER-LAMINAR STRESSES		PRINCIPAL ANGLE	STRESSES (ZERO SHEAR)		MAX SHEAR
		NORMAL-1	NORMAL-2	SHEAR-12	SHEAR XZ-MAT	SHEAR YZ-MAT		MAJOR	MINOR	
0	1	-1.17744E+05	-1.96924E+05	-2.24320E+04	2.77082E+03	-7.72118E+04	-14.77	-1.11830E+05	-2.02838E+05	4.55036E+04
0	1	8.39443E+04	1.94602E+05	1.49189E+04	0.0	0.0	82.45	1.96578E+05	8.19682E+04	5.73049E+04
0	2	-2.34280E+05	-3.78020E+05	-6.61743E+04	5.44033E+03	-8.75695E+04	-21.32	-2.08455E+05	-4.03845E+05	9.76954E+04
0	2	-9.19517E+04	-1.28368E+05	-2.84781E+04	7.25378E+03	-1.16759E+05	-28.70	-7.63584E+04	-1.43961E+05	3.38015E+04
0	2	5.03763E+04	1.21284E+05	9.21820E+03	5.44033E+03	-8.75695E+04	82.71	1.22463E+05	4.91975E+04	3.66327E+04
0	2	1.92704E+05	3.70936E+05	4.69145E+04	6.46567E-13	0.0	76.12	3.82531E+05	1.81110E+05	1.00711E+05

### c) Element Stresses

Figure 78 Parts of the output file of initial analysis

In order to form a better parametrization routine for Nastran, the format of the input files should be known well. Each bulk data entry has a specific format. In bulk data section of input file each line includes 80 columns. However a bulk data entry may span multiple lines. There are three types of data entries in Nastran which are integer, real and character. Integer does not contain any decimal point while real data includes a decimal point. It is important that, a single decimal point is not taken into consideration as a real zero value. Character data entry always starts with an alphanumeric character. Real numbers have many ways to be entered. In Table 24, all versions of real numbers are listed [44].

Table 24 Real number data entry types

7.0	.7E1	0.7+1
.70+1	7.E+0	70.-1

Nastran has three different field formats which are free field format, small field format and large field format. In Table 25, the definition of field formats is given, and general format of grid entry is shown in Figure 79 [44].

Table 25 Field Format Types

Free Field Format	Input data fields are separated by comma.
Small Field Format	Ten fields with eight characters
Large Field Format	Ten fields with eight character including actual data with sixteen characters

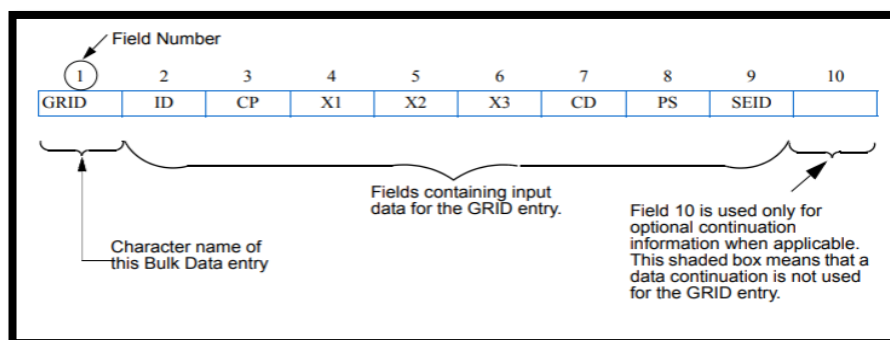


Figure 79 General format of grid entry [44]

Data fields are separated by commas in free field format. There are some restrictions for this field. Firstly, free field data must start in column 1 of a line. Secondly, in order to skip one field two commas, and to skip two fields three commas should be used. Finally, integer or character fields must not be used with more than eight characters because this causes a fatal error. A sample of grid data written in free field format is shown in Figure 80.

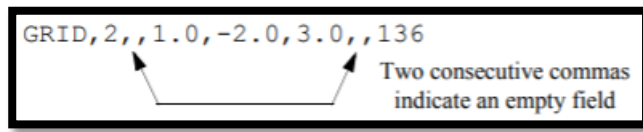


Figure 80 Grid data in free field [44]

In small field format, bulk data entry is divided into ten equal fields with eight characters. There are three basic rules for writing in small field format. First of all, first and last fields which are field-1 and field-10 have to be left justified. Secondly, second and ninth fields do not have to be right or left justified. Finally, small field input cannot include any embedded blanks. An example of small field data entry is shown in Figure 81.

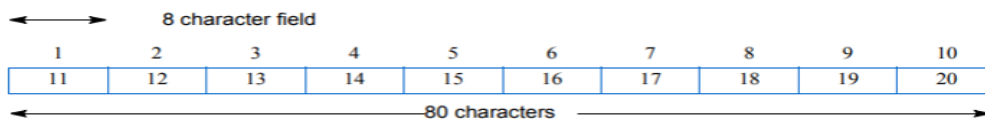


Figure 81 Small field data entry [44]

On the other hand, large field format is used when significant digits in small field format is not enough. Large field format requires at least two lines. The first and last field of each line consists of eight characters and the other fields include 16 characters. Large field data entries are denoted by a symbol which is called asterisk (\*). This symbol is written in the first field of first line and at the beginning of second line. An example of large field format is shown in Figure 82 [44].

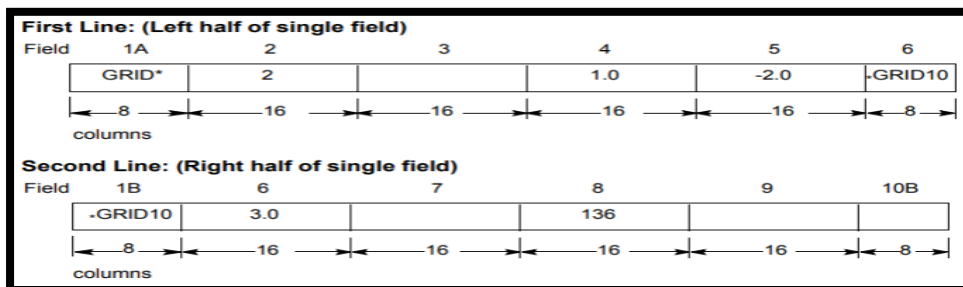


Figure 82 Large field data entry format [44]